論文 / 著書情報
Article / Book Information

題目(和文)	トモグラフィック発光分光計測と衝突輻射モデルにもとづくアルゴン誘導結合プラズマの位置分布診断
Title(English)	Positional Distribution Diagnosis of Argon Inductively Coupled Plasma Based on Tomographic Optical Emission Spectroscopic Measurement and Collisional-Radiative Model
著者(和文)	山下雄也
Author(English)	Yuya Yamashita
出典(和文)	学位:博士(工学), 学位授与機関:東京科学大学, 報告番号:甲第278号, 授与年月日:2025年3月26日, 学位の種別:課程博士, 審査員:赤塚 洋,浦壁 隆浩,竹内 希,清田 恭平,河邊 賢一,伊藤 剛仁
Citation(English)	Degree:Doctor (Engineering), Conferring organization: Institute of Science Tokyo, Report number:甲第278号, Conferred date:2025/3/26, Degree Type:Course doctor, Examiner:,,,,,
学位種別(和文)	博士論文
Type(English)	Doctoral Thesis

Positional Distribution Diagnosis of Argon Inductively Coupled Plasma Based on Tomographic Optical Emission Spectroscopic Measurement and Collisional-Radiative Model

トモグラフィック発光分光計測と衝突輻射モデルにもとづく
アルゴン誘導結合プラズマの位置分布診断

by

Yuya Yamashita

山 下 雄 也

A doctoral thesis

submitted to

Graduate Major in Electrical and Electronic Engineering,
Department of Electrical and Electronic Engineering,
School of Engineering,
Institute of Science Tokyo

in partial fulfillment of the requirements for the degree of

Doctor of Engineering

Supervised by Assoc. Prof. Dr. Hiroshi Akatsuka

March 2025

In the PDF version of this thesis, hyperlinks are provided. By selecting any figure, table, equation, reference number, URL, or table of contents heading cited in the text, you can directly jump to the corresponding page or website.

Summary

This thesis presents studies in diagnostic methods and findings for plasma diagnostics based on optical emission spectroscopic (OES) measurements. With backgrounds in both plasma science and engineering, the need for positional distribution diagnostics is becoming increasingly important. The objective of this thesis is to establish positional distribution diagnostics based on tomographic OES measurements and collisional-radiative (CR) models. The core content of this thesis consists of two published original papers. The first study focuses on the uncertainty of OES measurement-based plasma diagnostics caused by spectral reflectance of chamber inner wall. The second study finally established the objective of this thesis. In this thesis, 0.5–10 Pa argon (Ar) 13.56 MHz inductively coupled plasma (ICP) was employed as the experimental measurement target.

The first study addresses the issue of multiple reflected light from the chamber inner wall in OES-based plasma diagnostics. The multiple reflected light cases uncertainty in OES measurement of plasmas. However, the multiple reflected light has not been compensated for in previous studies. To resolve this problem, this study developed a simple method for measuring the spectral reflectance of the chamber inner wall. The developed method has a high degree of applicability to existing chambers. Additionally, a measurement method for the spectral emission coefficient was developed with compensation of multiple reflected light. This method reliably provides the radial distribution of the spectral emission coefficient under axial symmetry assumptions. Furthermore, the radial distribution of electron temperature (T_e) and electron density (N_e) was diagnosed based on the Ar CR model. This study employed 10 lines-of-sight on each side of the horizontal plane of the chamber, with separate sets for each side. The results showed that the uncertainty in T_e measurements increased by 0.6%, and the uncertainty in N_e measurements increased by 3.1% without correcting for spectral reflectance. These findings provide the first quantitative insight into the uncertainty of T_e and N_e due to multiple reflected light. The results suggest that accounting for chamber wall reflection improves the accuracy of OES measurement-based diagnostics. T_e and N_e were also measured with a Langmuir probe and

compared with the proposed method. Electromagnetic simulations further revealed that T_e and N_e distributions are influenced by the shape of the antenna and the placement of the window.

The second study focused on positional distribution diagnostics without any positional assumptions. Most tomographic OES measurement studies have remained focused on observing positional distributions of spectral emission coefficients or excited-level number densities. Some studies of tomographic OES measurement diagnosed T_e or N_e by analyzing based on simplified excitation-kinetics. However, these oversimplify excitation kinetics, leading to significant discrepancies with real structures and limitations in the plasma pressures and generation principles to which they can be applied. This study established positional distribution diagnostics based on tomographic OES measurements and CR models. A spectroradiometric system was constructed to simultaneously measure spectral radiance dependence on 18 lines-of-sight. Additionally, the computation program was developed for line-of-sight dependency spectral radiance, including a wavelength interpolation algorithm to enable using multi-channel polychromators, even with wide wavelength resolution. The spectral tomography calculation program was developed by the constrained regularization algorithm. The positional dependence of spectral emission coefficients was reconstructed. The positional distributions of T_e and N_e were diagnosed based on the Ar CR model. The dependence of power and pressure on the positional distribution of T_e and N_e was revealed. This study further assessed the repeatable uncertainty of the spectral emission coefficient, T_e, and N_e. This study also discussed the dependence of reduced population density on the position.

In conclusion, this thesis presents innovative approaches to improving plasma diagnostics through OES and spectral tomography. The findings demonstrate that the proposed tomographic OES system is a valuable, non-invasive diagnostic tool for industrial plasma applications. This research contributes to advancing non-invasive diagnostic methods of plasmas and lays the groundwork for further innovation in diagnostics and related fundamental and applied fields.

Acknowledgments

On this page, the author would like to express gratitude for the support received throughout the author's time as a doctoral student. The author would like to express their deepest gratitude to all those who supported and guided the author throughout the doctoral studies. The author's doctoral studies have been both rewarding and challenging, and it would not have been possible without their encouragement and assistance. The author is grateful to have had the opportunity to conduct research with people who have served as valuable role models and will continue to inspire the author.

The author expresses gratitude to Assoc. Prof. Dr. Hiroshi Akatsuka, the supervisor and chief examiner at the Institute of Science Tokyo (Science Tokyo). He provided the author with appropriate and helpful supervision, valuable and interesting discussions, and much warm encouragement. Furthermore, he provided an environment where students could research freely, openly, and enthusiastically. The author is pleased to have had the opportunity to learn from him about his philosophy of research and education.

The author expresses gratitude to the examiners: Assoc. Prof. Dr. Kenichi Kawabe, Assoc. Prof. Dr. Kyohei Kiyota, Assoc. Prof. Dr. Nozomi Takeuchi, and Prof. Dr. Takahiro Urakabe at Science Tokyo, Assoc. Prof. Dr. Tsuyohito Ito at The University of Tokyo, for their invaluable guidance, insightful feedback, and thoughtful discussions throughout the examination process.

The core content of this thesis is a result of collaborative research between Science Tokyo and ULVAC, Inc. The author expresses gratitude to Dr. Kenta Doi, Mr. Tetsuji Kiyota, and Mr. Keiichiro Asakawa, co-researchers at ULVAC. They provided guidance, cooperation, and thought-provoking discussions to the author at various stages of the research, including conception, experiments, analysis, and even the manuscript submission process. When the author faced difficulties in the research, they gave accurate advice and accompanied the author in resolving them. Furthermore, they offered warm encouragement. The author expresses gratitude to the people of ULVAC for supporting this collaborative research.

The author expresses gratitude to Mr. Masaki Yokoi and Ms. Yoko Sato at HORIBA STEC, Co., Ltd., and Mr. Kengo Yasui, Mr. Takumi Miyaoka, and Mr. Masayuki Sakurai at HORIBA, Ltd., for lending the multichannel spectrometer (M116, used in Chapter4) and advising on measurements using the spectrometer.

The author expresses gratitude to Assoc. Prof. Dr. Shigekazu Ito at Science Tokyo for renting the spectrophotometer and teaching the author how to use it under the equipment-sharing system at Science Tokyo. The author was able to measure the spectral reflectance of various materials by the spectrophotometer.

The author expresses gratitude to Mr. Toshihiko Hara, a Technical Support Staff at Science Tokyo, for machining various components. Thanks to his special machining skills, the author could construct the desired experimental system.

From now on, the author expresses gratitude to the dear members of the Akatsuka Laboratory (Akatsuka Lab), who made the research environment and student life interesting and enjoyable through their research and daily interactions. The members of the Akatsuka Lab were very varied in expertise areas, research styles, research interests, personalities, and many other aspects. The author has learned countless things from these members.

The author expresses gratitude to Mr. Atsushi Nezu, a Technical Specialist at Science Tokyo, for his technical experimental support, maintenance, discussions, and laboratory management of resources and safety. He also offered warm encouragement and advice to the author, as well as to the other members of the Akatsuka Lab, making life in the lab even more enjoyable.

The author expresses gratitude to the colleague students in the Akatsuka Lab for their work on the study of inductively coupled plasma (ICP) with the author—Mr. Koki Fukumoto, Mr. Hinata Hanyu, Mr. Wentao He, Mr. Sotaro Hosoya, Mr. Kenta Ishi, Mr. Wataru Kikuchi, Mr. Akira Kobayashi, Mr. Ayaki Sakurai, Mr. Kazuki Shimatani, Mr. Shuhei Watanabe, Mr. Yuchen Ye, and Mr. Kazuma Yoneda. The author and these individuals discussed research ideas, performed experiments together, discussed the results, and sometimes even built experimental equipment and programs. This experimental study would not have been possible without their collaboration. Furthermore, the author expresses gratitude to the colleague students in the Akatsuka Lab who worked on research outside of the scope of ICP—Mr. Jun Enomoto, Mr. Kenta Fuse, Dr. Thijs van der Gaag, Mr. Koji Kikuchi, Mr. Takumi Kikuchi, Mr. Silin Li, Dr. Keren Lin, Mr. Yosuke Shimada, Mr. Kohaku Sunakawa, Mr. Tomoya Taguchi, Mr. Shogo Yamanaka, Mr. Kohei Yamashita, and Mr. Koyo Yoshida. The author is grateful for the

opportunity to discuss, analyze, and conduct experiments with them, which has significantly broadened and deepened the author's research perspective.

Furthermore, the author expresses gratitude to the researchers and students met at conferences, the professors who provided feedback on departmental presentations, the classmates and peers from Science Tokyo, and the administrative staff, though individual names cannot be mentioned.

The author would also like to express gratitude to the author's family and friends for their emotional support.

The author has received financial support from competitive funding during the three years of the doctoral program. The author would like to express gratitude by writing here.

First, the author expresses gratitude for fellowships. These fellowships provided the author with financial support for research and ensured focus without undue burden. From April 2022 to March 2023, the author was awarded the Pioneering Research Initiated by the Next Generation (SPRING) of Japan Science and Technology Agency (JST)—JST SPRING Grant Number JPMJSP2106. From April 2023 to March 2025, the author was awarded the Research Fellowships of Japan Society for the Promotion of Science for Young Scientists (JSPS Research Fellowships for Young Scientists)—JSPS KAKENHI Grant Number JP23KJ0884.

Next, the author expresses gratitude for grants that supported conference attendance and presentations. These supports have allowed the author to engage in discussions with researchers and students from around the world and form lasting relationship. A presentation [1] at ICRP-11/GEC 2022 was supported by the Student Travel Grant from the American Physical Society. A presentation [2] at ICPIG 2023 was supported by the Student Presentation Grant from The Japan Society of Applied Physics. A presentation [3] at ESCAMPIG 2024 was supported by the International Exchange Grant in Science and Technology from the Watanabe Memorial Foundation for The Advancement of New Technology.

Contents

Chapter 1

Introduction

1.1 Research background

1.1.1 Plasmas and its applications

Plasmas

Plasmas are an ionized gas that consists of electrons, positive ions, atoms, and molecules [6]. In nature, astronomical objects [7], and atmospheric electrical phenomena such as the aurora and lightning are also examples of plasma. To generate plasma artificially, a gas is discharged or heated. Plasma is used in a wide range of engineering fields [6]. For example, plasma has long been used as a light source for various discharge lamps such as arc lamps. Other examples include heat treatments such as arc welding and plasma cutting, nuclear fusion, chemical reactions such as ozone generation and treatment of harmful substances, sterilization [8], and growth control of living organisms.

Plasma processing

One of the most important fields of engineering applications of plasmas is in various material processing. **Plasma processing** refers to material processing technologies using plasmas [9, 10][1]. Plasma processing include surface modification, film deposition, etching, vapor phase growth, sputtering, and ion implantation. Plasma processing is applied to various industries, for example, various inorganic and organic chemical products, metal products, electronic components, and electronic devices. In particular, plasma processing is used in precision materials processing in semiconductor manufacturing i.e., integrated circuits, liquid crystal panels, flat panels, and solar cell panels. Consequently, plasma processing serves as a cornerstone for advancements in engineering applications.

[1] A plasma applied for plasma processing is called **processing plasma**.

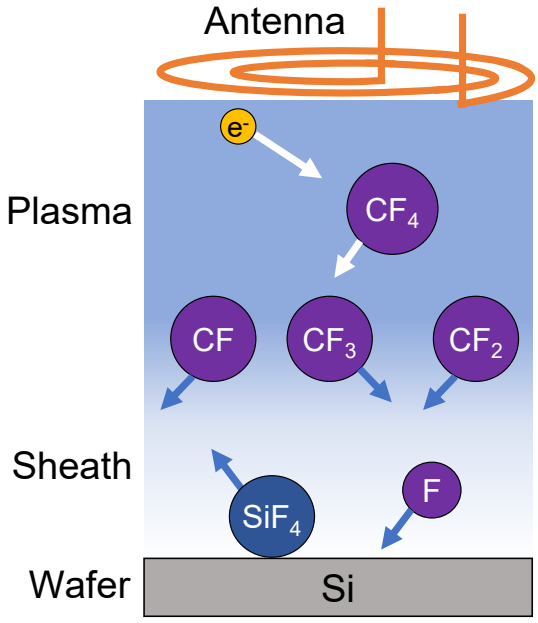

Fig. 1.1: The Conceptual diagram of the reaction mechanism for silicon (Si) wafer etching by carbon tetrafluoride (CF_4) plasma.

Reaction mechanisms in plasma processing: A case study of plasma etching

The reaction mechanism in processing plasmas depends on the gas species of plasmas, the principle of generation, the pressure range, and the material to be processed.

Figure 1.1 is an overview of the reaction mechanism using plasma etching as an example of the reaction mechanism. Free electrons (called initial electrons) exist in the reaction vessel even before an electric field is applied. When an electric field is applied to the reaction vessel, the free electrons are accelerated. As the accelerated electrons collide with the atoms and molecules of the gas introduced into the reaction vessel, various reactions occur. This includes ionization processes, which generate additional electrons and cause the plasma to become electrically conductive, resulting in a sustained discharge. Various other elementary processes also take place. Fluorine radicals and atoms are produced during this process. These fluorine species are transported to the substrate, causing etching [9, 10].

1.1.2 Plasma diagnostics

Temperature and density as macroscopic parameters of plasmas

As mentioned in Section 1.1.1, plasmas contain atoms, molecules, electrons, and positive ions. Therefore, by knowing their velocity distribution function (or the temperature as the

average of velocity distribution function) and number density[2], the macroscopic characteristics of plasma can be expressed [9, 10]. **Plasma diagnostics** refers to methods used to measure and analyze properties of plasmas, such as temperature, density, and composition.

In low-pressure[3] weak ionization plasmas, the kinetic energy of electrons is often significantly larger than that of ions and atomic molecules (low-temperature non-equilibrium plasma). Therefore, in low-temperature non-equilibrium plasmas, elementary processes due to electron collisions play an important role in describing the population kinetics [9, 10].

Plasma diagnosis of electron temperature[4] and density[5] directly provides the macroscopic characteristics of bulk plasma. In addition, when applying electromagnetic field analysis and its coupled analysis with particle methods or fluid methods simulations to experimental devices, electron temperature and density can be used as parameters for comparison between the calculation and experimental results [11–13]. Furthermore, by performing coupled simulations with the electron temperature and density obtained from plasma diagnostics as input parameters, reactions in the sheath, interface, surface, and solid phase can be understood. The simulation result is expected to be used for understanding and predicting the physical properties of solid phases after processing [14].

Significance and necessity of plasma diagnostics

In plasma processing, the required post-processing physical properties depend on the specific objectives. However, operators of plasma processing apparatus can directly control only operating parameters such as pressure, discharge power, and gas flow rate, as shown in Fig. 1.2. Therefore, processing design—that is, the act of determining operating parameters based on the specific purpose of the process—is required. Present process design often relies on experimental optimization. This involves assigning operating parameters, conducting trial processing, and evaluating the resulting physical properties afterward. By repeating this process, optimal operating parameters are determined. This design approach is costly and is not always capable of achieving the desired device. Moreover, this issue becomes particularly pronounced when dealing with new materials, shapes, and physical properties with limited prior processing experience. In particular, in semiconductor processing, rational and efficient processing design is

[2] In the plasma field, **density** often refers to number density, i.e., mass per unit volume, rather than mass density.

[3] **Low-pressure** means pressure lower than atmospheric pressure. In other words, **low-pressure plasma** means plasma generated in a chamber where the pressure is maintained below atmospheric pressure.

[4] **Electron temperature** is the temperature corresponding to the average electron energy in a plasma.

[5] **Electron density** is defined as the number density of free electrons per unit volume of plasma.

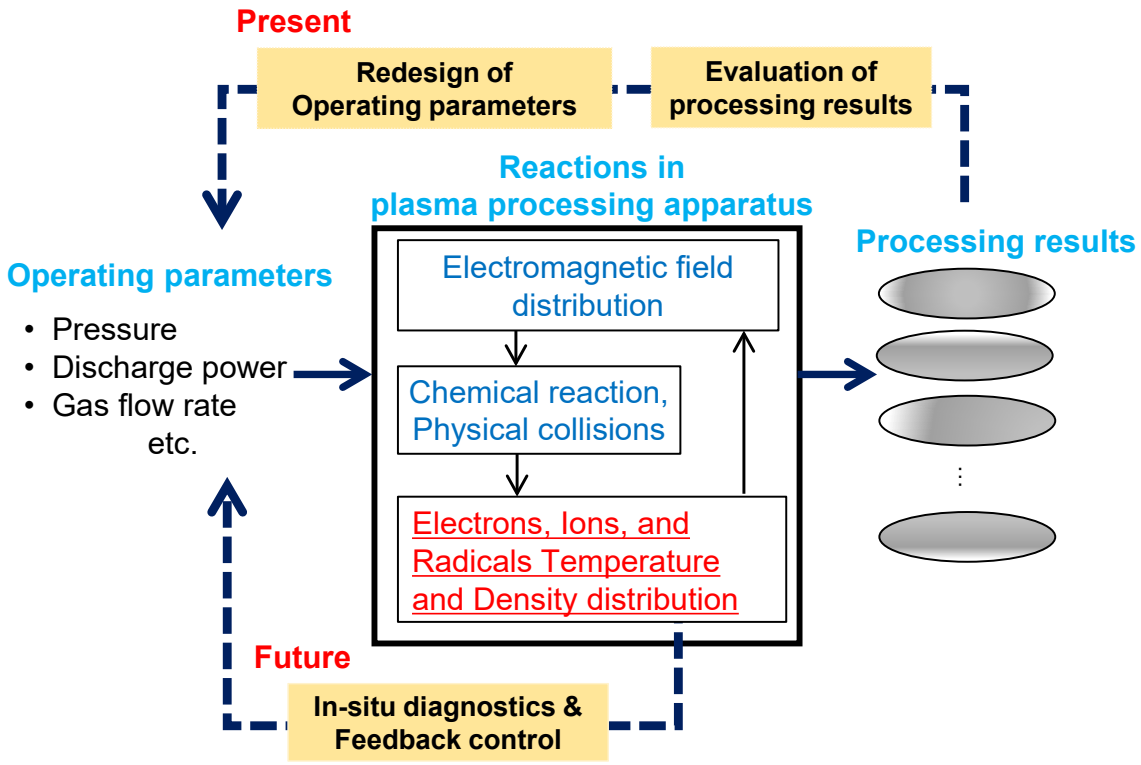

Fig. 1.2: The Conceptual diagram of operational parameter design in plasma processing apparatus.

required due to high integration, miniaturization, and even larger wafer diameters [15–17].

To solve this problem, it is necessary to predict the macro parameters required to achieve the desired post-processing physical properties and to design and optimize plasma processing equipment and process conditions that achieve them. Furthermore, by diagnosing the desired plasma state during the process and controlling the process, it is possible to overcome the limitations of conventional experimental optimization [15, 16]. In this way, plasma diagnostics play an important role in advancing plasma processing.

In addition, although these goals include challenges from a long-term perspective, examples of applications that can be applied in a relatively short time include the following: For example, real-time monitoring [18] through anomaly detection and uncertainty detection during the process can be used. Plasma diagnostics have the potential to improve the reliability and yield of plasma processing [16].

1.2 Identification of issues

1.2.1 Positional distribution diagnosis based on tomographic optical emission spectroscopic measurement and collisional-radiative model

To obtain a more detailed understanding of plasma characteristics, it is necessary to perform a positional distribution diagnosis [19]. This is because phenomena occurring in the central and peripheral regions of the plasma are different. The phenomena in these regions influence each other through transport and diffusion processes. Additionally, local inhomogeneities can arise due to the generation principles or apparatus, such as standing waves in microwave plasmas [20]. Furthermore, from an engineering standpoint, diagnosis as a positional distribution is necessary. Because, it is necessary to optimize the design of plasma processing equipment and workpiece based on the knowledge obtained from positional distribution diagnosis. For example, in semiconductor processing plasmas, as the diameter of wafers becomes larger, the diameter of the plasma is also becoming larger. It is necessary to improve the uniformity of the physical properties in the surface direction after processing even for large-diameter wafers [21]. To achieve this, it is necessary to elucidate the phenomenon by positional distribution diagnosis [22].

In optical emission spectroscopic (OES) measurement, tomography is a method for observing plasma as a positional distribution. However, there are almost no analyses using collisional-radiative (CR) models in tomographic OES measurement. For this reason, the description remains phenomenological, and the elucidation of the plasma reaction mechanism is currently insufficient. As mentioned above, temperature and density diagnosis is necessary to understand the physical properties of plasma. It is required to establish temperature and density diagnosis using tomographic OES measurements and CR models.

1.2.2 Uncertainty in plasma diagnostics by optical emission spectroscopic measurement due to multiple reflections on the chamber inner wall

Let's consider an OES measurement of plasma generated in a situation where it is surrounded by objects, such as in a chamber or discharge tube. In such cases, part of the light emitted from the plasma is reflected by the inner walls of the chamber or discharge tube. Some of this reflected light is further reflected by the walls, a phenomenon known as multiple reflection. Both the direct and the multiple-reflected light are incident on the lens installed on the wall. Therefore, to accurately calculate the spectral emission coefficient of the plasma, it is

necessary to distinguish between these two types of light. Furthermore, it is important to understand how the presence or absence of multiple reflections affects both the spectral emission coefficient and the diagnostic results.

In order to calculate this multiple reflection precisely, ray tracing must be used to calculate the ratio of the spectral radiance[6] of the direct light and the multiple reflected light observed on the wall surface. The input data for ray tracing requires the geometric structure of the chamber and the bidirectional reflectance distribution function (BRDF)[7] of its components. However, it is difficult to apply ray tracing to plasma processing equipment, especially plasma processing equipment used in actual processes. Because, for the geometric structure of the chamber, it is possible to reuse 3D design data. However, BRDF strongly depends on the material, composition, filling rate, and surface roughness, which is a physical property value after processing. In other words, many parameters determine the BRDF of a material. Therefore, it is difficult to apply BRDF in general using existing databases. Therefore, BRDF must often be measured individually. To actually measure BRDF, a dedicated measuring device (a device that can scan the angle of incidence and reflection on the measurement target) is required. In addition, the materials that make up the inner wall surface of semiconductor process plasma chambers are often curved. It is considered that the BRDF of flat plates and curved processed materials will be different. For these reasons, it is considered practically difficult to obtain the BRDF[8].

1.3 Research objective of this thesis

The research objective of this thesis is to develop a positional distribution diagnosis of plasma based on tomographic OES measurement and CR model. The diagnostic scheme of this study works towards being applicable regardless of gas species or plasma source. However, in the experiments of this study, argon low-pressure inductively coupled plasma (ICP) is employed an example of the measurement target. Argon gas is employed for basic verification, in which the atomic and molecular processes are relatively simple. Low-pressure ICP is widely used in etching processes, in which the in-plane distribution is important. Therefore, the experiment with low-pressure ICP is ideal for discussing the possibility of application.

[6]**Spectral radiance** is defined as "density of radiance, with respect to wavelength [23]". **Radiance** is defined as "density of radiant intensity with respect to projected area in a specified direction at a specified point on a real or imaginary surface [23]".

[7]BRDF is spectral reflectance for each angle of incidence and reflection.

[8]In addition, BRDF data of plasma devices is not generally provided by device manufacturers.

1.4 Structure of this thesis

This thesis consists of five chapters. Chapters 1 and 2 are the preliminary chapters. Chapters 3 and 4 constitute the core content of this thesis and are reprinted from the original papers published in [4] and [5], respectively. Chapter 5 is the conclusion.

Chapter 1 is an introduction to this thesis. This chapter provides an overview of plasma and the significance of plasma diagnostics by OES measurement. This chapter also reviews previous research in this field and raises current issues. Based on that, this chapter sets the objectives of this research and describes its significance.

Chapter 2 introduces the basic theory in preparation for the following discussion in Chapters 3 and 4. This chapter will support the understanding of this research, especially for readers who specialize outside of this research field or are new to this research field.

Chapter 3 covers the effect of multiple reflections on the chamber inner wall on plasma diagnostic results. In this chapter, the spatial distribution of the plasma is assumed to be axially symmetric. A simple method for measuring the spectral reflectance of the chamber inner wall is proposed. A calculation method for a radial dependence of spectral emission coefficient with multiple reflection compensation is also proposed. Furthermore, the radial distributions of electron temperature and density are diagnosed based on the CR model. The uncertainty in the diagnostic results caused by multiple reflected lights is revealed. Chapter 3 is also positioned as a preliminary consideration for Chapter 4.

Chapter 4 covers tomographic OES measurement and plasma diagnosis based on tomographic OES. In contrast to Chapter 3, no assumption on the spatial distribution of the plasma is imposed in this chapter. An optical system of simultaneous measurement of wavelength and lines-of-sight is implemented. Furthermore, an algorithm for pixel-based spectral tomography is proposed. From this, the positional distribution of the spectral emission coefficient is obtained. The positional distributions of electron temperature and density are diagnosed based on the CR model. The dependence of the diagnostic results on discharge power and pressure dependence is experimentally revealed.

Chapter 5 presents the conclusion of this thesis. Furthermore, this chapter discusses and proposes future prospects for both research and applications of plasma diagnostics based on OES measurements.

Chapter 2

Theoretical background

This chapter introduces basic theories to provide the fundamental knowledge for understanding Chapters 3 and 4.

2.1 Spectroradiometry

In this section, spectroradiometry will first be introduced as the basic theory for measuring light as a physical quantity. Next, the application of spectroradiometry to plasmas will be presented as an extension of this theory.

2.1.1 Basic theory of spectroradiometry

Definitions of radiometric quantities and spectral radiometric quantities

A general term for the physical quantity that combines the time and space components of the radiant energy of optical radiation is referred to as **radiometric quantities** [23]. **Radiometry** [23, 24] is measurement of radiometric quantities[1].

Spectral radiometric quantities [23, 25] are defined as radiometric quantities per unit wavelength, i.e. expressed as the wavelength derivative of radiometric quantities. Especially in radiometry, measurement of spectral radiometric quantities is called **spectroradiometry** [24, 25].

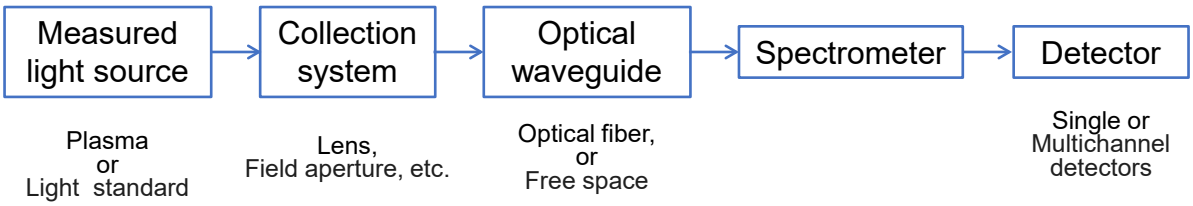

Fig. 2.1: The conceptual diagram of the typical structure of spectroradiometric system.

Spectroradiometric system

Spectroradiometric system typically consists as shown in Fig. 2.1 and described below [25, 26]. **Collection system** is typically a lens or field aperture. The collection system extracts the light emitted from the source being measured, depending on the aimed radiometric quantities and aimed measurement spatial range. **Optical waveguide** transmits light from the focusing system to the spectrometer. The optical waveguide is typically an optical fiber or free space, sometimes assembled with concave mirrors. In designing an optical waveguide, the degrees of freedom required for the system layout and the tolerable optical loss must be considered as constraints. **Spectrometer** is a device that spatially separates (called dispersion) light by wavelength. There are various types based on different principles [26]. In the ultra-violet–visible–near-infrared wavelength range, diffraction grating-based spectrometers are often used. **Detector** is a device that converts light into an electrical signal. Detectors are classified by principle and include photomultiplier tubes and various photodiodes. Measurement wavelength range and sensitivity of detectors depend on its principle. Detectors are structurally classified as single-channel detectors and multi-channel detectors. Single-channel detectors have only one detection element. On the other hand, Multichannel detectors, have multiple detector elements and can measure multiple lights simultaneously.

The combination of a single-channel detector and a spectrometer is called a **monochromator** [25]. With monochromators, only a specific wavelength is measured in one measurement. Therefore, when measuring a spectrum, the wavelength is scanned over time. On the other hand, the combination of a multichannel detector and a spectrometer is called a **polychromator** [25]. The advantage of polychromators is that they enable the observation of the wavelength dependence of spectral radiometric quantity in a single shot. Note that if the dispersion range of the

[1]The psychological quantities of radiation perceived by the human eyes is known as a **photometric quantities** [23, 25], and measurement of photometric quantities is called **photometry** [23, 25]. Photometric quantities are primarily used in fields where human perception plays a role, such as lighting engineering. In this way, it is important to note that radiometric quantities and photometric quantities are often confused, though their meanings differ significantly.

desired measurement wavelength exceeds the observation range of the detector, the diffraction grating may be rotated in the polychromator to temporally scan the wavelength for measurement.

Spectral radiance calibration of spectroradiometric system

The components of the spectroradiometric system have wavelength dependence. Therefore, the spectrum, as the response value of the detector, is a count value specific to the spectroradiometric and wavelength, and cannot be directly compared with other systems. Therefore, spectroradiometry is achieved by comparatively measuring with the measured light source and standard light sources using the same spectroradiometric system [25].

This subsection introduces spectral radiance calibration[2] of the spectroradiometric system. The spectral radiance of measured light sources is obtained by proportional measurement with respect to a spectral radiance standard as detailed in Eq. (4.3). A generic example of the spectral radiance standard is a method that combines a spectral irradiance[3] standard and a standard diffuse reflector [25, 27]. Details of this experimental system and calculation flow will be presented in Figs. 4.3 and 4.4 in Section 4.2.2, respectively. The **spectral irradiance standard**[4] is a standard light source with a spectral irradiance calibration value $E_{\mathrm{std}}(\lambda)$ at a predetermined distance and position.

The **standard diffuse reflector**[5] is a reflector that is calibrated as a spectral reflectance $R_{\mathrm{std}}(\lambda)$ under predetermined geometric conditions and has characteristics close to uniform diffuse reflection.

The spectral radiance on the standard diffuse reflector surface $L_{\mathrm{std}}(\lambda)$ will be obtained as shown in Eq.(4.1) [25,27]. The calibration results of $R_{\mathrm{std}}(\lambda)$ and $E_{\mathrm{std}}(\lambda)$ are usually supplied by the calibration service provider as wavelength discrete values. Therefore, $R_{\mathrm{std}}(\lambda)$ and $E_{\mathrm{std}}(\lambda)$ at any wavelength must be obtained by interpolation from the calibration wavelength point of $R_{\mathrm{std}}(\lambda)$ and $E_{\mathrm{std}}(\lambda)$, respectively. The widely employed formula used for the interpolation is the Lagrangian interpolation formula which uses four calibration wavelength points of, two before

[2]The choice of light standards and radiometric collection systems varies depending on which radiometric quantities are being measured.

[3]**Spectral irradiance** is defined as"density of irradiance, with respect to wavelength [23]". **Irradiance** is defined as "density of incident radiant flux with respect to area at a point on a real or imaginary surface [23]".

[4]As of 2025 in Japan, spectral irradiance standards available include the halogen standard lamp (JPD100V500WCS, USHIO LIGHTING, INC.) for 250–2500 nm [25,28–30] and the xenon calibrated light source unit (L7810-03, Hamamatsu Photonics K.K.) for 200–800 nm.

[5]As of 2025, standard diffuse reflectors made of polytetrafluoroethylene (PTFE) [25]are widely used. Examples of these reflector products include Spectralon from Labsphere, Inc., or Zenith Polymer from SphereOptics GmbH.

and two after, as shown in Eq. (4.2) [31].

Wavelength calibration of spectroradiometric system

Wavelength calibration is also required for the spectroradiometric system [25]. Wavelength calibration means the act of calibrating wavelength to the operation variable[6] of the wavelength of spectroradiometry system.

A wavelength standard light source with a known wavelength is observed using a spectroradiometric system. The wavelength operation variable of the spectroradiometric system are recorded for the desired wavelength range. The wavelength at any point is obtained by polynomial approximation of the experimentally obtained relationship between the wavelength operation variable and the wavelength. A line-spectrum light source with a line-spectrum width sufficiently narrow compared to the slit width of the spectrometer, and with a known wavelength, is used as the wavelength standard.

As dedicated wavelength standard light sources, low-pressure mercury lamps (such as a pencil-type mercury lamp[7]) are widely used in the ultraviolet to visible range, and low-pressure argon lamps are widely used in the visible to near-infrared range [25, 31]. In the case of spectroscopic measurements of plasma, the plasma itself can sometimes be used as a wavelength standard [26].

2.1.2 Spectroradiometry in plasma studies

In this subsection, the basic theory of applying spectroradiometry to plasmas is discussed. Plasmas have three-dimensional volumes. Therefore, it is necessary to consider the spatial extent when discussing radiometry for plasmas[8,9].

The spectral radiance of the plasma is observed using a focusing lens with a field diameter sufficiently small compared to the apparent size of the plasma. Plasmas have thickness in the line-of-sight direction. Therefore, **spectral emission coefficient** is introduced. The spectral

[6]For example the angle of a diffraction grating in a moving grating spectrometer, or the pixels of a multichannel detector in a polychromator.

[7]The uncertainty of the pencil-type mercury lamp is reported be 0.0001 nm [32]. Note that the uncertainty of the irradiance of this lamp is reported in the literature [33]. However, the irradiance uncertainty of this lamp is larger than that of the spectral irradiance standard light source introduced in Section 2.1.1. Therefore, the pencil-type mercury lamp should not be used as an irradiance standard in situations where a spectral irradiance standard source is available.

[8]This is probably one of the hardest concepts to master for someone new to this field, in the author's opinion.

[9]On the other hand, in the analysis of general-purpose lighting fixtures and flat-panel displays, the depth in the line-of-sight direction of the lamp or screen can often be ignored. This is because the distance between the observer and those light sources is significantly larger compared to the length of the light source in the line-of-sight direction.

emission coefficient is a physical quantity used in plasma spectroradiometry, defined as the optical power emitted from a unit volume of plasma per unit solid angle and unit wavelength [34]. The spectral radiance is equal to the line integral along the line-of-sight of the spectral emission coefficient emitted from the plasma located along the line-of-sight.

2.2 Plasma spectroscopy

Plasma spectroscopy is a study to describe the physical properties of plasmas from its optical emission or absorption spectrum.

2.2.1 Line- and continuum-spectra

Plasma spectra are divided into line- and continuum- spectra by their generation mechanisms [26, 34].

Line-spectra are generated by transitions between energy levels. The initial and final states of line-spectrum have specific energy values. The wavelengths of line spectra correspond to the energy differences between the initial and final states and are observed as sharp lines. Therefore, transitions of line-spectrum are called **bound-bound transitions**. Note that energy levels refer to electronic states in atoms, and electronic, vibrational, and rotational states in molecules.

Continuum-spectra are spectra that are continuous with respect to wavelength. The origins of continuum-spectra include free-bound transitions, free-free transitions, and molecular continuum-spectra. **Free-bound transition** occurs when free electrons are captured by ions and recombine (**radiative recombination**). The energy, which is the sum of the kinetic energy of the free electrons and the ionization energy of the excited levels, is emitted as photons. On the other hand, **free-free transition** occurs when free electrons move close to ions and bend their orbits, causing the ions to slow down. In other words, it is a process in which the electron transitions to a lower energy state. The energy difference during this process is emitted as photons. The emitted light is called bremsstrahlung. When a molecule dissociates, it absorbs the energy required for dissociation in the form of a photon. When atoms recombine to form molecules, they emit light along a continuum. These are non-bonding transitions, specifically called molecular continuum transitions.

2.2.2 Light absorption and emission in plasmas

In this section, absorption and emission of light in plasmas are introduced.

The mechanism of light **absorption** in plasmas is as follows [34]. When an atom is irradiated with light of a wavelength (resonant wavelength) that corresponds to the difference between the low and high-energy levels, the atom absorbs a photon and transitions occur from the lower energy level to the higher energy level. The absorption probability is expressed by **Einstein's B coefficient**.

Light **emission** in plasmas occurs through two mechanisms. The first is the **stimulated emission process**. In the stimulated emission process, electrons are induced to move from a high-energy level to a low-energy level when light is irradiated to atoms, and light is emitted during this transition. The stimulated emission process is the reversal process of the absorption process, and its emission probability is expressed by Einstein's B coefficient. For the lasing process to occur, the number density of the high-energy level must be greater than that of the low-energy level[10].

The second is the **spontaneous emission process**. In the spontaneous emission process, electrons spontaneously transition from a high-energy level to a low-energy level with light emission, without any external influence. The transition probability for the spontaneous emission process is expressed by **Einstein's A coefficient**. A coefficient is determined both theoretically and experimentally in atomic and molecular physics. Data on A coefficients can also be accessed through online databases, such as the NIST Atomic Spectra Database [35] for atomic spectra. Molecular spectra can be identified using data handbooks, such as Pearse *et al.*' book [36].

2.3 Atomic and molecular processes in plasmas

2.3.1 Elementary processes of plasmas

The individual reactions in a plasma are called **elementary processes**. **Excitation** refers to changes in the internal energy of atoms. **Ionization** and **attachment** are elementary processes that generate charged particles. **Recombination**, **dissociation**, and **diffusion** are elementary processes that annihilate charged particles [26, 37].

Quantifying the rates of elementary processes is essential for understanding Atomic and molecular processes. **Rate coefficient** is the rate of change in particle number density per unit time in a unit volume of plasma, caused by the elementary process. Rate coefficients for collisional processes can be obtained as a function of the macroscopic parameters of the

[10]This distribution of number density is called **population inversion**.

plasma and the reaction cross-section as inputs. The reaction cross-section is an indicator of the probability that a specific interaction, such as a collision or reaction, occurs between two particles [26, 37]. Reaction cross-sections are determined both theoretically and experimentally in atomic and molecular physics. Data on reaction cross-sections can also be accessed through online databases, such as the LXCat [38][11].

2.3.2 Modeling of population kinetics and collisional-radiative models

In plasmas, various elementary processes are simultaneously occurring at the microscopic scale. To understand the atomic and molecular processes in the plasmas on a macroscopic scale, it is necessary to introduce a model of population kinetics. The model of model of population kinetics is expressed that take plasma parameters (such as energy distribution, temperature, density, and pressure) as input and calculate elementary processes of the plasma, providing population density as output[12] [26, 42].

A **collisional-radiative (CR) model** is a type of model of population kinetics. The CR model is named for its focus on describing the main elementary processes through electron collision and radiation processes [43] (although it often includes other elementary processes as well). The population density of excited levels is obtained by solving the rate equations for each excited level as simultaneous equations, using plasma macroscopic parameters (such as energy distribution or temperature, density, and pressure) as input [26, 42].

2.3.3 Ionization and recombination of plasmas

The excited level number density n_i is expressed as a linear combination of the ground level number density n_1 and the ion number density n_{I} as explanatory variables as follows [42, 44]:

$$\begin{aligned} n_i &= Z(i)\, r_0(i)\, n_{\mathrm{I}}\, n_{\mathrm{e}} + \frac{Z(i)}{Z(1)}\, r_1(i)\, n_1 \\ &= N_0(i) + N_1(i) \qquad\qquad (i = 2, 3, \cdots), \end{aligned} \tag{2.1}$$

where $Z(i)$ is a **Saha-Boltzmann coefficient** of level i as follows:

$$Z(i) = \frac{g_i}{2g_{\mathrm{I}}} \left(\frac{h^2}{2\pi m_{\mathrm{e}} k T_{\mathrm{e}}} \right)^{3/2} \exp\left(\frac{\chi_i}{k T_{\mathrm{e}}} \right), \tag{2.2}$$

whereg_i and χ_i are the statistical weight and ionization energy of level i, respectively; g_{I} is the partition function of the fully ionized ion; h is the Planck constant, k is Boltzmann constant,

[11] For a detailed description of the LXCat project, please refer to the following references [39–41].

[12] In the field of plasma science and engineering, **population density** means a number density on the levels. Furthermore, population density distribution means the dependence of the number density on the levels.

and m_e is electron mass, respectively. $r_0(i)$ and $r_1(i)$ are population coefficients. The situation in which n_i depends only on n_1 is called a (fully) ionized plasma, while the situation in which n_i depends only on n_I is called a (fully) recombined plasma [42, 44]. Fully ionized and fully recombined plasmas are special cases; most plasmas exist in an intermediate situation.

Plasmas with a low degree of ionization are called weakly ionized plasmas. Note that the low-pressure ICP employed in the experiments of this thesis is also classified as a weakly ionized plasma.

2.3.4 Phases of ionizing- and recombining- plasmas

To conceptually understand the kinetics of the increase and decrease of excited states in ionizing- and recombining- plasmas, Fujimoto classified plasma phases using the (effective) principal quantum number p and the reduced electron density N_e/z, calculated by dividing electron density N_e by the seventh power of the nuclear charge z, as follows [44–49].

The ionizing-plasma phases are classified into the **corona phase** and the **saturation phase**, with the boundary between them called **Griem's boundary** as shown in Fig. 2.2. The saturation phase is further classified into (thermal equilibrium and ladder-like excitation), with the boundary between them called **Byron's boundary**.

The recombining-plasma phases are classified into the **capture-radiative-cascade phase** and the **saturation phase**, with the boundary between them called **Griem's boundary** as shown in Fig. 2.3. The saturation phase is further classified into (ladder-like excitation and local thermodynamic equilibrium), with the boundary between them called **Byron's boundary**.

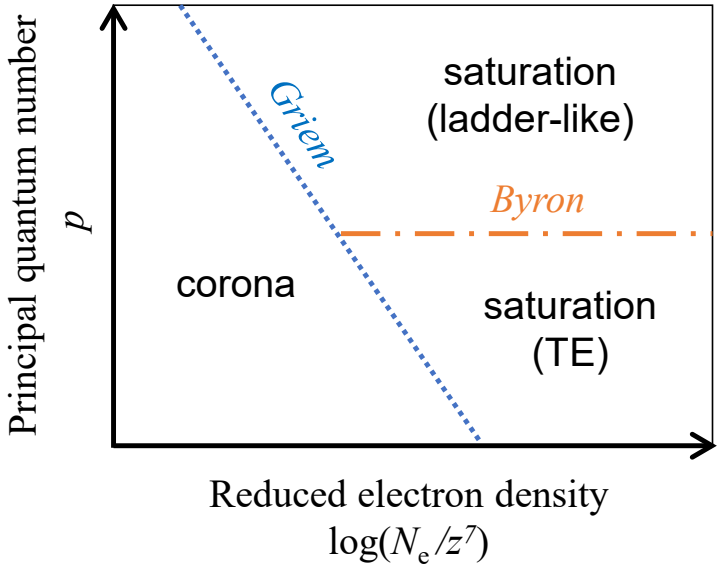

Fig. 2.2: The conceptual diagram of phases of ionizing-plasma. TE stands for thermal equilibrium.

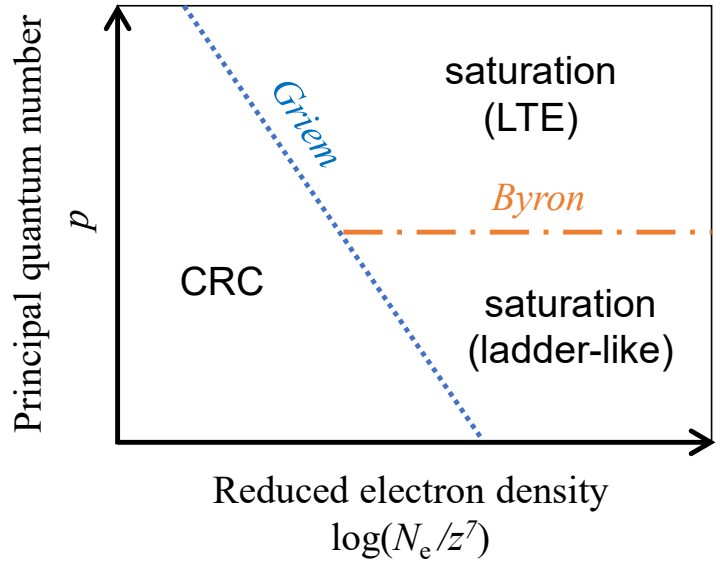

Fig. 2.3: The conceptual diagram of phases of recombining-plasma. CRC stands for capture-radiative-cascade. LTE stands for local thermodynamic equilibrium.

Chapter 3

Radial dependence diagnosis of inductively coupled Ar plasma based upon optical emission spectroscopic measurement with spectral reflectance compensation [4]

3.1 Introduction

Optical emission spectroscopy (OES) has been widely employed in a method of plasma diagnostics as it allows for non-disturbing plasma measurements based on a relatively simple measurement setup. Macroscopic plasma parameters, such as electron temperature T_e and density N_e, are of interest consistently because they govern the reactions in a plasma. The collisional-radiative (CR) model [50] is an atomic-molecular process model that provides the excited-level number density distribution from macroscopic plasma parameters. The excited-level number density distribution of plasmas is experimentally obtained from the spectral emission coefficient, which is defined as the spectral radiant flux emitted per unit solid angle from a unit volume of plasma. Thus, the macroscopic plasma parameters, T_e and N_e, can be obtained by fitting the experimental data with the theoretical value of the excited-level number density distribution determined by the CR model [51, 52]. Spatially resolved plasma diagnostics based on OES have been achieved through Abel inversion of multi-position spectral data considering the axial symmetry of the plasma [53–59]. However, the measured spectral radiance includes the sum of both the direct light from the plasma volume and the reflected light at the chamber inner wall.

To calculate the excited-level number density distributions, it has been pointed out in a previous study [60] that the light reflection from the chamber inner walls must be considered. That is, the dependence of optical emission spectra on time was observed during the deposition of thin films in an ICP setup with a two-type wall of different reflectivity. In the highly reflective wall, the dependence of spectra varied periodically due to the thin-film interference on the wall. The diagnostic results of the line-pair method based on the acquired spectra were reported to be significantly different [60]. As for the report that compensates for light reflections on the chamber walls, ray-tracing analysis of visible camera images based on the assumed wall reflectance has been reported in the field of fusion reactor research [61, 62]. However, few studies have reported on the spectral properties and influence of the reflected light on chamber inner walls. Moreover, few studies have been conducted on reflectance-aware diagnosis in the field of low-temperature weakly ionized plasmas, particularly semiconductor processing apparatus. An experimental approach to evaluate the light reflection is required to achieve practical diagnostic availability.

The previous reports that corrected for the effect of reflections required bidirectional reflectance distribution function (BRDF) data of the geometrical structures and components in the chamber.

Therefore, although rigorous calculations can be performed, there are practical difficulties, particularly when applying the method to existing plasma devices for the semiconductor industry. This is because measuring the BRDF of each component requires time and effort, such as removing the component and measuring it with a spectrometer.

This study proposed a simple *in situ* method for evaluating the spectral reflectance of the chamber inner wall in this paper. Based on the spectral reflectance calculated using the proposed method, the net spectral emission coefficient of the plasma is obtained. Eventually, T_e and N_e are evaluated based on line spectra fitting.

3.2 Experimental setup of ICP apparatus

Figure 3.1 shows an inductively coupled plasma (ICP)—generating apparatus employed in this study. The inner wall of the chamber employed anodized aluminum. The chamber inner diameter was Φ = 354 mm. An RF antenna was placed at the top of the chamber over a synthetic quartz window ($\Phi = 205$ mm). The chamber height was 208 mm just below the top window and 193 mm at the outside of the window. The view window (width 110 mm $\times$ height 5 mm)

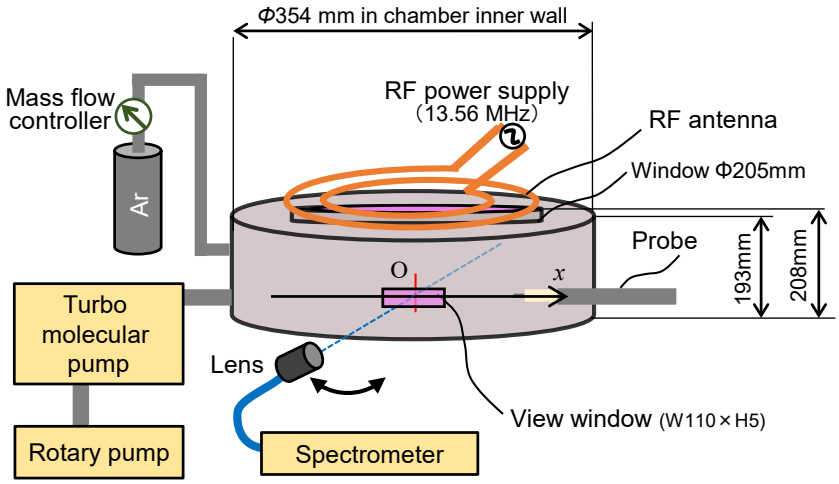

Fig. 3.1: The schematic diagram of ICP generating apparatus (non-scale). The measured height of the OES and probe are the same, $z = 0$. (Dimensions are actual measurements.) Reproduced from Yuya Yamashita *et al.*, Rev. Sci. Instrum., **94**, 083503, (2023) [4], with the permission of AIP Publishing.

of a synthetic quartz ($t_{\mathrm{win}} = 6$ mm thick) was installed on the side wall of the chamber.

3.3 Light reflection by chamber inner wall

3.3.1 Refraction of line-of-sights on the view window

In OES measurement experiments, the directly measurable quantity is the spectral radiance of the air-side surface of the view window. In this study, the line-of-sight is set at an angle to the window surface, which causes a shift in the line-of-sight due to refraction at the window. Figure 3.2 denotes the concept of the path of the light emitted from the plasma in the chamber to incident on the lens through the view window of the chamber. θ_{air} is defined as the angle between the line-of-sight and the window normal in air. θ_{win} is defined as the angle between the line-of-sight and the window normal in air in the view window. The relationship can be obtained from Snell's law as follows:

$$\frac{\sin\theta_{\mathrm{air}}}{\sin\theta_{\mathrm{win}}} = \frac{n_{\mathrm{win}}(\lambda)}{n_{\mathrm{air}}(\lambda)}, \tag{3.1}$$

where λ is the wavelength and $n_{\mathrm{air}}(\lambda)$ and $n_{\mathrm{win}}(\lambda)$ are the spectral refractive index of air and the window, respectively. Therefore, the following relationship is obtained:

$$\theta_{\mathrm{win}}(\lambda) = \sin^{-1}\left(\frac{n_{\mathrm{air}}(\lambda)}{n_{\mathrm{win}}(\lambda)}\sin\theta_{\mathrm{air}}\right). \tag{3.2}$$

The spectral refractive index in vacuum n_{vac} is approximately equal to $n_{\mathrm{air}}(\lambda)$, $n_{\mathrm{air}}(\lambda) \simeq n_{\mathrm{vac}}(\lambda) = 1$. Therefore, the incident angle between the line-of-sight and the window normal in vacuum,

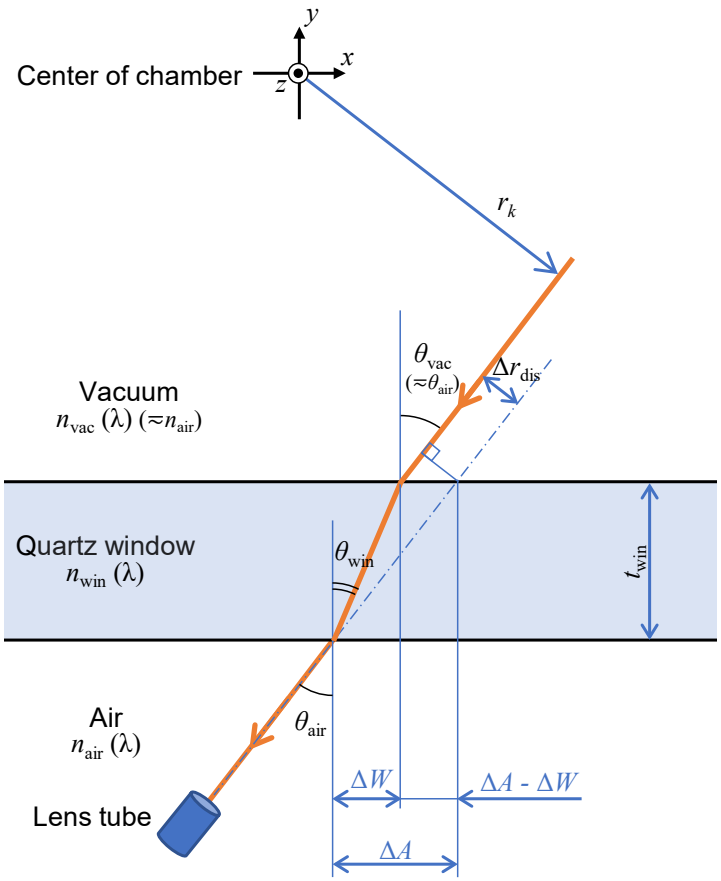

Fig. 3.2: The conceptual diagram of light propagation in the window. Here, the line-of-sight is parallel to the paper surface and the window interface is vertical to the paper surface. Reproduced from Yuya Yamashita *et al.*, Rev. Sci. Instrum., **94**, 083503, (2023) [4], with the permission of AIP Publishing.

$\theta_{\mathrm{vac}}(\lambda)$, can be assumed to be equal to θ_{air}, $\theta_{\mathrm{air}}(\lambda) \simeq \theta_{\mathrm{vac}}(\lambda)$. Therefore, $\Delta W(\lambda)$ and $\Delta A(\lambda)$ as shown in Fig. 3.2 can be obtained as follows:

$$\Delta W(\lambda) = t_{\mathrm{win}} \tan\theta_{\mathrm{win}}, \tag{3.3}$$

where t_{win} is the thickness of the view window,

$$\Delta A(\lambda) = t_{\mathrm{win}} \tan\theta_{\mathrm{air}}. \tag{3.4}$$

Therefore, the distance between the line-of-sight in the air and the line-of-sight in the vacuum is obtained as follows:

$$\begin{aligned} \Delta r_{\mathrm{dis}}(\lambda) &= [\Delta A(\lambda) - \Delta W(\lambda)] \cos\theta_{\mathrm{air}}(\lambda) \\ &= t_{\mathrm{win}}[\tan\theta_{\mathrm{air}}(\lambda) - \tan\theta_{\mathrm{win}}(\lambda)] \cos\theta_{\mathrm{air}}(\lambda). \end{aligned} \tag{3.5}$$

On OES measurement of the plasma (Sec. 3.4.2), the positions of the line-of-sights, which were employed in this study, were calculated, as shown in Table 3.1, which were calculated by using the above equations. Note that $n_{\mathrm{win}}(\lambda)$ was employed as the literature values [63, 64] for the calculation of this study.

Note that in the calculation to obtain radially resolved spectral inversion of this study, r_k is the radius from the center (z axis) of the chamber in the vacuum, which was employed for the calculation of this study ("mean" as shown in Table 3.1) regardless of wavelength because the aberration was sufficiently small to the field of view diameter in the wavelength range, which was employed for the plasma diagnosis in this study.

3.3.2 Fresnel on the view window

Due to Fresnel reflection, some of the light emitted from the plasma is reflected at the surface of the window. Figure 3.3 shows the concept of the Fresnel reflection on the view window. To calculate the spectral emission coefficient of the plasma, the spectral radiance just before the plasma enters the window is required. On the other hand, the quantity that can be directly observed in the experiment is the spectral radiance at the interface between the outside of the window and the air. In this section, we discuss spectral radiance measurements that take these effects into account. (The meanings of the symbols that appear in the following equations are defined, as shown in Fig. 3.4.) In this section, the relationship $n_{\mathrm{air}}(\lambda) = n_{\mathrm{vac}}(\lambda) = 1$ is also assumed.

The spectral energy transmittance $T'_{\mathrm{s}}(\lambda)$ and the spectral energy reflectance $R'_{\mathrm{s}}(\lambda)$ are expressed for the s(TE)-wave on the first incidence from the plasma in vacuum to the vacuum side

Table 3.1: The angle and nearest radius of line-of-sights of the OES measurement of the plasma. Reproduced from Yuya Yamashita *et al.*, Rev. Sci. Instrum., **94**, 083503, (2023) [4], with the permission of AIP Publishing.

Radius number k	Radius in air [nm]	Incident angle in air $\theta[win]$ (deg)	Nearest radius for chamber center in vacuum [mm] Mean r_k (λ = 750.3–978.6 nm)	Min. (λ = 750.3 nm)	Max. (λ = 978.6nm)
0	0.0	0.000	0.000	0.000	0.000
1	17.7	0.000	17.700	17.700	17.700
2	35.4	0.000	35.400	35.400	35.400
3	53.1	23.893	52.081	52.078	52.083
4	70.8	23.893	69.781	69.778	69.783
5	88.5	23.893	87.481	87.478	87.483
6	106.2	23.893	105.181	105.178	105.183
7	123.9	45.000	121.008	121.003	121.013
8	141.6	45.000	138.708	138.703	138.713
9	159.3	50.894	155.427	155.421	155.433
10	...	...	177.000	...	...

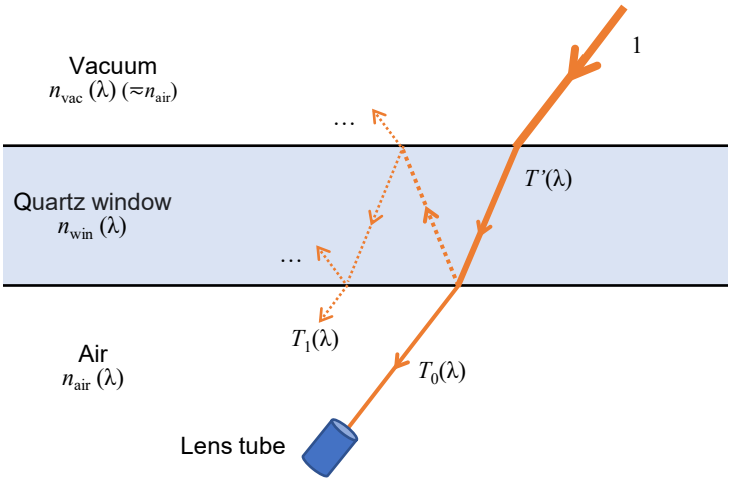

Fig. 3.3: The spectral radiance observed by the lens is smaller than the spectral radiance emitted by the plasma due to Fresnel reflection. Reproduced from Yuya Yamashita *et al.*, Rev. Sci. Instrum., **94**, 083503, (2023) [4], with the permission of AIP Publishing.

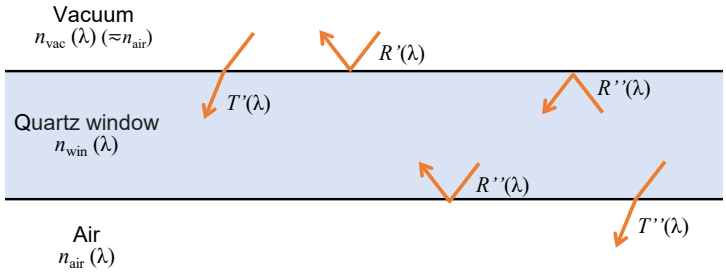

Fig. 3.4: Meaning of the symbols for transmittance and reflectance. Reproduced from Yuya Yamashita *et al.*, Rev. Sci. Instrum., **94**, 083503, (2023) [4], with the permission of AIP Publishing.

of the window as follows [65]:

$$T'_{\mathrm{s}}(\lambda) = \frac{\sin 2\theta_{\mathrm{air}}\ \sin 2\theta_{\mathrm{win}}}{\sin^2(\theta_{\mathrm{air}} + \theta_{\mathrm{win}})}, \tag{3.6}$$

$$R'_{\mathrm{s}}(\lambda) = \frac{\sin^2(\theta_{\mathrm{air}} - \theta_{\mathrm{win}})}{\sin^2(\theta_{\mathrm{air}} + \theta_{\mathrm{win}})}. \tag{3.7}$$

Similarly, the spectral energy transmittance $T'_{\mathrm{p}}(\lambda)$ and the spectral energy reflectance $R'_{\mathrm{p}}(\lambda)$ are expressed for the p(TM)-wave as follows [65]:

$$T'_{\mathrm{p}}(\lambda) = \frac{\sin 2\theta_{\mathrm{air}}\ \sin 2\theta_{\mathrm{win}}}{\sin^2(\theta_{\mathrm{air}} + \theta_{\mathrm{win}})\ \cos^2(\theta_{\mathrm{air}} - \theta_{\mathrm{win}})}, \tag{3.8}$$

$$R'_{\mathrm{p}}(\lambda) = \frac{\tan^2(\theta_{\mathrm{air}} - \theta_{\mathrm{win}})}{\tan^2(\theta_{\mathrm{air}} + \theta_{\mathrm{win}})}. \tag{3.9}$$

From Eqs. (3.6) and (3.7), the spectral energy transmittance from the window to the air on the window - the air boundary, $T''_{\mathrm{s}}(\lambda)$, and the spectral energy reflectance from the window to the window on the window - the air or vacuum boundary, $R''_{\mathrm{s}}(\lambda)$, are expressed as follows:

$$T''_{\mathrm{s}}(\lambda) = T'_{\mathrm{s}}(\lambda), \tag{3.10}$$

$$R''_{\mathrm{s}}(\lambda) = R'_{\mathrm{s}}(\lambda). \tag{3.11}$$

From Eqs. (3.8) and (3.9), the spectral energy transmittance: $T''_{\mathrm{p}}(\lambda)$ and the spectral energy reflectance: $R''_{\mathrm{p}}(\lambda)$ are expressed for the p-wave as follows:

$$T''_{\mathrm{p}}(\lambda) = T'_{\mathrm{p}}(\lambda), \tag{3.12}$$

$$R''_{\mathrm{p}}(\lambda) = R'_{\mathrm{p}}(\lambda). \tag{3.13}$$

The spectral transmittance of the zeroth-order transmitted light, that is, the ratio of the incident light power on the vacuum–window interface to the power of the light passing through the vacuum–window interface and further right away passing through the window–vacuum interface (as shown in Fig. 3.3), is given for s and p waves as follows, respectively:

$$T_{\mathrm{s0}}(\lambda) = T'_{\mathrm{s}}(\lambda)\ T''_{\mathrm{s}}(\lambda), \tag{3.14}$$

$$T_{\mathrm{p0}}(\lambda) = T'_{\mathrm{p}}(\lambda)\ T''_{\mathrm{p}}(\lambda). \tag{3.15}$$

Therefore, the spectral transmittance of the zeroth-order transmitted light is given for the natural polarization wave as follows:

$$T_0(\lambda) = \frac{1}{2}\left[T_{\mathrm{s0}}(\lambda)\ +\ T_{\mathrm{p0}}(\lambda)\right]. \tag{3.16}$$

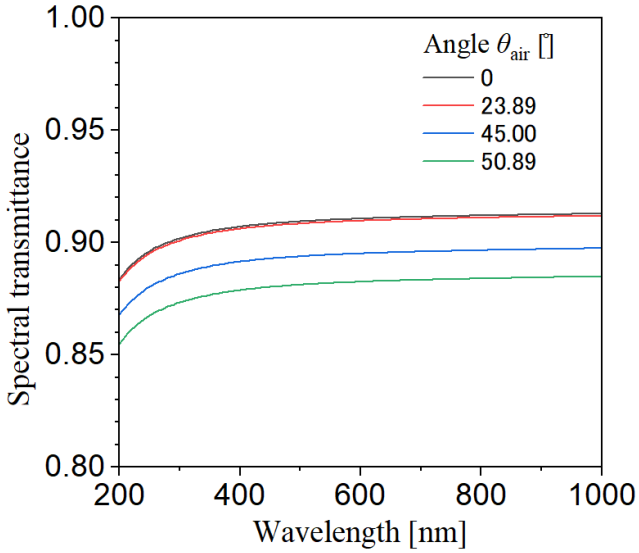

Fig. 3.5: The calculation result of spectral transmittance $T_0(\lambda)$ of the zeroth-order transmitted light on the 6 mm thick quartz window. The spectral transmittance is expressed as the power ratio to incident light. Reproduced from Yuya Yamashita *et al.*, Rev. Sci. Instrum., **94**, 083503, (2023) [4], with the permission of AIP Publishing.

Fig.3.5 denotes the calculation result of Eq. (3.16) for the experimental setup of this study.

Note that the spectral transmittance of the first-order transmitted light, that is, the light passing through the vacuum–window interface, reflected on the window side of the window–air boundary, reflected on the window side of the window–vacuum boundary, and transmitted on the window–air boundary, is given for s and p-waves as follows, respectively:

$$T_{s1}(\lambda) = T_s'(\lambda)\,\{R_s''(\lambda)\}^2\,T_s''(\lambda), \tag{3.17}$$

$$T_{p1}(\lambda) = T_p'(\lambda)\,\{R_s''(\lambda)\}^2\,T_p''(\lambda). \tag{3.18}$$

For natural polarization light, the transmittance is expressed as follows:

$$T_1(\lambda) = \frac{1}{2}\left[T_{s1}(\lambda) + T_{p1}(\lambda)\right]. \tag{3.19}$$

The calculation result of $T_1(\lambda)$ for the experimental setup of this study is shown in Fig.3.6.

In this study, only the zeroth-order transmitted light was assumed to enter the lens. This is because the higher-order transmitted light above the first order has less energy than zero-order transmitted light (as shown in Fig.3.6) and higher-order transmitted light above the second order has even lower intensity. Moreover, the first-order or higher-order transmitted light is incident at a displaced position except at vertical incidence. In addition, the window is sufficiently thick relative to the wavelength that thin-film interference phenomena are unlikely to be involved.

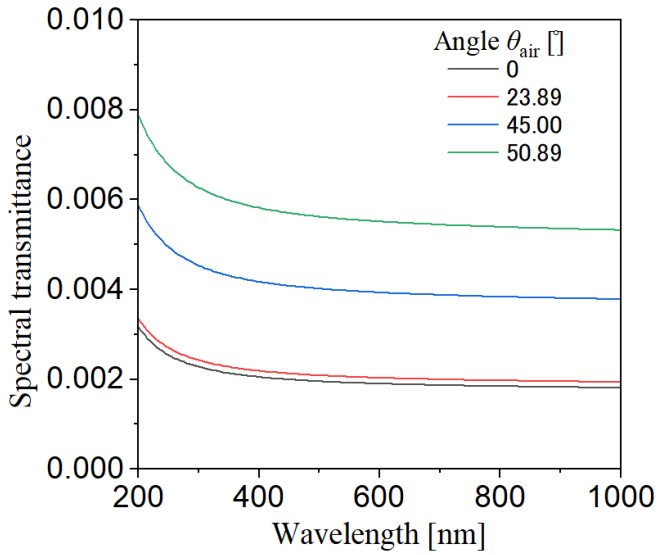

Fig. 3.6: The calculation result of spectral transmittance $T_1(\lambda)$ of first-order transmitted light on the 6 mm thick quartz window. The spectral transmittance is expressed as the power ratio to incident light. Reproduced from Yuya Yamashita *et al.*, Rev. Sci. Instrum., **94**, 083503, (2023) [4], with the permission of AIP Publishing.

Therefore, the spectral radiance on the vacuum side surface of the window is calculated as follows:

$$L_{\mathrm{I}}(\lambda) = \frac{L'_{\mathrm{I}}(\lambda)}{T_0(\lambda)}, \tag{3.20}$$

where $L'_{\mathrm{I}}(\lambda)$ is the spectral radiance on the air side surface of the window, which was experimentally obtained by the OES measurement experiment[1].

3.3.3 Evaluation of spectral reflectance of inner wall

This section discusses the strategy of obtaining the average spectral reflectance of the chamber inner wall. In this study, the chamber was regarded as an integrating sphere on the inner wall to facilitate a simplified evaluation to measure the spectral reflectance of the chamber. However, an integrating sphere is generally spherical, and its inner surface is composed of a diffuse reflective material according to the cosine law, and the area of the aperture port is designed to be sufficiently small to the area of the diffuse reflective material. In contrast, the shape of this chamber is cylindrical. The inner surface of the chamber consists of anodized aluminum (no coloring; the thickness of the anodic oxide film was ∼6-10 μm; the fine hole was sealed by using the nickel acetate method), which does not guarantee compliance with the cosine law. Further-

[1] [This footnote has been supplemented in this thesis to deepen the reader's understanding and was not included in the original paper [4].] For the specific data of $L'_{\mathrm{I}}(\lambda)$, see Figs. A.1 and A.2 in Appendix A.

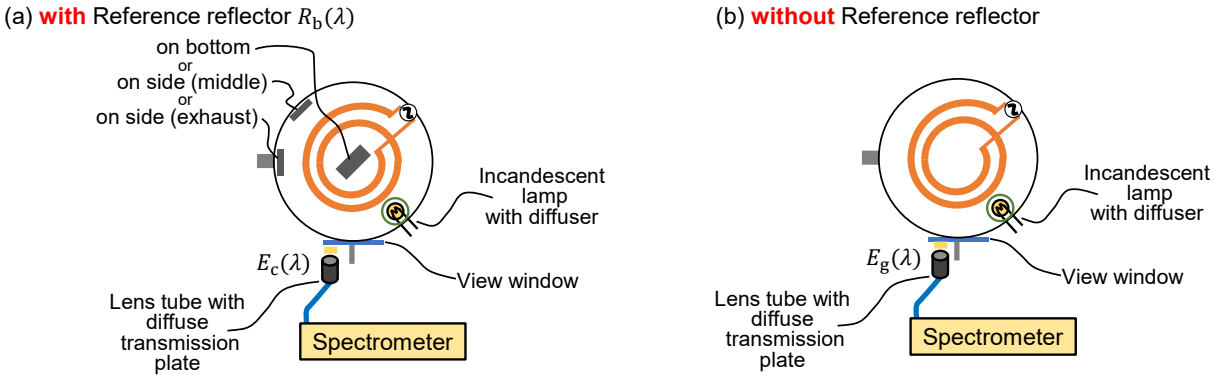

Fig. 3.7: The top view diagram of spectral-reflectance measurement. In (a), a reference reflector was placed at one of the locations. To investigate how well the chamber acts as an integrating sphere, the dependence of the spectral reflectance of the chamber inner wall on the position of the reference reflector was measured. In (b), the reference reflector was not placed. Reproduced from Yuya Yamashita *et al.*, Rev. Sci. Instrum., **94**, 083503, (2023) [4], with the permission of AIP Publishing.

more, the chamber has windows, a gas inlet, and exhaust ports. Therefore, strictly speaking, this chamber cannot be regarded as an integrating sphere, and differences will arise, but for the sake of simplicity in optical modeling, such an assumption was made.

In this study, the following method for measuring the average spectral reflectance of the chamber inner wall was applied. Note that this method is similar to the method used to evaluate the average spectral reflectance of the inner wall of the integrating sphere [25]. (1) A graphite plate that has surface area S_b was employed as the reference reflector. The spectral total reflectance $R_b(\lambda)$ of the graphene reference reflector was calibrated with a UV–VIS–NIR spectrophotometer (U-4100, Hitachi High-Tech Science) beforehand. Note that the spectral total reflectance is the sum of the specular and diffuse reflected spectral radiant flux relative to the sum of the incident spectral radiant flux. (2) Figure 3.7 illustrates the conceptual setup of the spectral-reflectance measurement. An incandescent lamp (G-1282H, Asahi Electric) was placed inside the chamber. To prevent direct light from the lamp from entering directly the reference graphene reflector and lens, the lamp was covered with a douser. The lamp works the same as a self-absorption measurement lamp in a spherical light fluxmeter. In other words, the reference reflector or the lens is indirectly illuminated by multiple reflected lights on the chamber inner wall. Furthermore, a lens tube with a diffuse transmission plate was set on the quartz view window of the chamber side wall to measure spectral-count value, which is proportional to spectral irradiance at the inner wall surface. The lens tube was connected to the spectrometer (MS3504i, SOL instruments) with the charge coupled device (CCD) detector (DU420A-OE, Andor Technology). (3) The spectral-count value $I_g(\lambda)$ was measured without the reference

reflector in the chamber [as shown in (b) of Fig. 3.7]. (4) The reference reflector was placed on the chamber inner wall, as shown in (a) of Fig. 3.7. The spectral-count value $I_c(\lambda)$ was measured with the reference reflector in the chamber.

The derivation of the spectral reflectance of the chamber wall is as follows. The spectral irradiance at the inner wall surface without and with the reference reflector in the chamber, $E_g(\lambda)$ and $E_c(\lambda)$, is as follows, respectively:

$$\begin{aligned} E_g(\lambda) &= K_1(\lambda)\, I_g(\lambda), \\ E_c(\lambda) &= K_1(\lambda)\, I_c(\lambda), \end{aligned} \tag{3.21}$$

where $K_1(\lambda)$ is a constant, which is determined by the system's spectral response. The spectral irradiance at the inner wall surface $E_g(\lambda)$, is calculated as follows [25]:

$$E_g(\lambda) = K_2(\lambda)\frac{R_g(\lambda)}{1-R_g(\lambda)}, \tag{3.22}$$

where $K_2(\lambda)$ is a constant, which is determined by the total spectral radiant flux of the incandescent lamp and the chamber inner size, and $R_g(\lambda)$ is the spectral reflectance of the inner wall. When the reference reflector is installed in the chamber, the average spectral reflectance is expressed as follows:

$$\begin{aligned} R_c(\lambda) &= \frac{S_g - S_b}{S_g} R_g(\lambda) + \frac{S_b}{S_g} R_b(\lambda) \\ &= (1-\alpha) R_g(\lambda) + \alpha R_b(\lambda), \end{aligned} \tag{3.23}$$

where S_g is the surface area of the chamber inner wall, $\alpha = S_b/S_g$ $(0 < \alpha < 1)$. The spectral irradiance at the inner wall surface with the reference reflector is as follows:

$$E_c(\lambda) = K_2(\lambda)\frac{R_c(\lambda)}{1-R_c(\lambda)}. \tag{3.24}$$

When $F(\lambda) = E_c(\lambda)/E_g(\lambda)$ is defined, the following relationship is obtained:

$$\begin{aligned} F(\lambda) &= \frac{E_c(\lambda)}{E_g(\lambda)} \\ &= \frac{R_c(\lambda)}{1-R_c(\lambda)} \frac{1-R_g(\lambda)}{R_g(\lambda)} \qquad (0 < F(\lambda) < 1), \end{aligned} \tag{3.25}$$

and from Eq. (3.21), we have

$$F(\lambda) = \frac{I_c(\lambda)}{I_g(\lambda)}. \tag{3.26}$$

The following equation is obtained using Eqs. (3.23) and (3.25) and eliminating $R_c(\lambda)$:

$$A R_g^2(\lambda) + B R_g(\lambda) + C = 0, \tag{3.27}$$

where

$$\begin{cases} A = (1-\alpha)[1-F(\lambda)] > 0, \\ B = [1-\alpha R_{\mathrm{b}}(\lambda)][F(\lambda)-1]+\alpha > 0, \\ C = -\alpha R_{\mathrm{b}}(\lambda) < 0. \end{cases} \tag{3.28}$$

$R_{\mathrm{g}}(\lambda)$ must be $0 < R_{\mathrm{g}}(\lambda) < 1$. Therefore, $R_{\mathrm{g}}(\lambda)$ is obtained as follows:

$$R_{\mathrm{g}}(\lambda) = \frac{-B+\sqrt{B^2-4AC}}{2A}. \tag{3.29}$$

Therefore, $R_{\mathrm{g}}(\lambda)$ was obtained and based on Eqs. (3.26) and (3.29) from the experimental values $I_{\mathrm{g}}(\lambda)$ and $I_{\mathrm{c}}(\lambda)$.

3.3.4 Calculation of net spectral emission coefficient of plasma

In this section, we discuss the strategy for obtaining the radial distribution of the spectral emission coefficients of the plasma from the OES measurement of plasmas. In this study, the spatial distribution of the spectral emission coefficient of the plasma was assumed to be z axis cylindrical symmetry. Let $\varepsilon(\lambda, r)$ be the spectral emission coefficient of the microvolume element $\mathrm{d}\boldsymbol{v}$ at radius r on the x-y plane and z on the z axis; the total spectral emission flux from $\mathrm{d}\boldsymbol{v}$, $\mathrm{d}\Phi_{\mathrm{T}}(\lambda, r)$, is expressed as follows:

$$\mathrm{d}\Phi_{\mathrm{T}}(\lambda, r) = 4\pi\, \varepsilon(\lambda, r)\, \mathrm{d}\boldsymbol{v}. \tag{3.30}$$

Therefore, the spectral total radiation flux of the plasma in the chamber, $\Phi_{\mathrm{T}}(\lambda)$, is expressed as follows:

$$\begin{aligned} \Phi_{\mathrm{T}}(\lambda) &= \int_{\boldsymbol{v}} \mathrm{d}\Phi_{\mathrm{T}}(\lambda, r) \\ &= \int_{\boldsymbol{v}} 4\pi\, \varepsilon(\lambda, r)\, \mathrm{d}\boldsymbol{v}. \end{aligned} \tag{3.31}$$

Applying the variable transformation from the rectangular coordinate system to the cylindrical coordinate system $(x, y, z) \to (r, \theta, z)$, the following equation can be obtained because $\mathrm{d}\boldsymbol{v} = r\, \mathrm{d}r\, \mathrm{d}\theta\, \mathrm{d}z$:

$$\begin{aligned} \Phi_{\mathrm{T}}(\lambda) &= \int_{z''}^{z'} \int_0^{2\pi} \int_0^R 4\pi\, \varepsilon(\lambda, r)\, r\, \mathrm{d}r\, \mathrm{d}\theta\, \mathrm{d}z \\ &= 8\pi^2 H \int_0^R \varepsilon(\lambda, r)\, r\, \mathrm{d}r, \end{aligned} \tag{3.32}$$

where R is the cylinder inner radius of the chamber; z' and z'' are the upper and lower position of the chamber along the z axis, respectively, and $H = z' - z''$ is the height along the z axis of the chamber.

The spectral irradiance by the multiple reflections illuminating the inner wall surface has position dependence. Therefore, as mentioned in the Introduction, to rigorously calculate the effect of multiple reflections by the inner wall, it is necessary to perform calculations using the ray-tracing method. The method requires the geometry of the inner wall and BRDF, which is a complex calculation. However, in this study, we propose a calculation method by "average" spectral irradiance for multiple reflections on the chamber inner wall surface. We were inspired by the "luminous flux method" used in the field of lighting engineering to develop the proposed method. The proposed method is undeniable that the calculation error increases compared to the ray-tracing method. However, the proposed method is computationally simpler than the ray-tracing method. Furthermore, the proposed method is especially useful for multiple reflection correction in situations where it is not possible to measure the BRDF of all the components of the inner wall, for example, in existing plasma devices. The proposed methodology is as follows.

The average spectral irradiance on the chamber inner wall by the multiple reflected light of $\Phi_{\mathrm{T}}(\lambda)$ is as follows [25]:

$$E_{\mathrm{refl}}(\lambda) = \frac{R_{\mathrm{g}}(\lambda)\,\Phi_{\mathrm{T}}(\lambda)}{[1-R_{\mathrm{g}}(\lambda)]\,S_{\mathrm{g}}}. \tag{3.33}$$

Assuming Lambertian reflection, the spectral radiance on the chamber inner wall by the multiple reflected light of $\Phi_{\mathrm{T}}(\lambda)$ is expressed as follows:

$$\begin{aligned} L_{\mathrm{refl}}(\lambda) &= \frac{R_{\mathrm{g}}(\lambda)}{\pi} E_{\mathrm{refl}}(\lambda) \\ &= \frac{R_{\mathrm{g}}^2(\lambda)\,\Phi_{\mathrm{T}}(\lambda)}{\pi[1-R_{\mathrm{g}}(\lambda)]\,S_{\mathrm{g}}}. \end{aligned} \tag{3.34}$$

Inserting Eq. (3.32), we get

$$L_{\mathrm{refl}}(\lambda) = \frac{R_{\mathrm{g}}^2(\lambda)}{\pi[1-R_{\mathrm{g}}(\lambda)]\,S_{\mathrm{g}}}\, 8\pi^2 H \int_0^R \varepsilon(\lambda, r)\, r\,\mathrm{d}r. \tag{3.35}$$

The spectral radiance on the window vacuum side surface of the line-of-sight whose nearest distance to origin $x = x''$ on the $x-y$ plane, $L_{\mathrm{I}}(\lambda, x'', z)$, is the sum of the spectral radiance due to direct light from the plasma in the line-of-sight and the multiple reflections of light emitted from the entire plasma,

$$L_{\mathrm{I}}(\lambda, x'', z) = L_{\mathrm{D}}(\lambda, x'', z) + L_{\mathrm{refl}}(\lambda), \tag{3.36}$$

where $L_{\mathrm{D}}(\lambda, x'', z)$ is the spectral radiance at the window surface on $x = x''$ due to direct light caused by the micro-volume elements of the plasma on the line-of-sight, which through on the

$x-y$ plane and whose nearest point to the origin in the line-of-sight is $(x,y,z) = (x'',0,0)$ as follows:

$$L_{\mathrm{D}}(\lambda,x'',z) = \int_{-\sqrt{R^2-x''^2}}^{\sqrt{R^2-x''^2}} \varepsilon(\lambda, x'', y, z)\,\mathrm{d}y. \tag{3.37}$$

As $\varepsilon(\lambda, x'', y, z)$ is the even function of y, the following relationship can be obtained:

$$L_{\mathrm{D}}(\lambda,x'',z) = \int_{0}^{\sqrt{R^2-x''^2}} 2\,\varepsilon(\lambda, x'', y, z)\,\mathrm{d}y. \tag{3.38}$$

By the variable transformation from the rectangular coordinate system to the cylindrical coordinate system, $(x,y,z) \to (r,\theta,z)$, we get the following relationship as $x''^2 + y^2 = r^2$ and $\mathrm{d}y = r\,\mathrm{d}r/\sqrt{r^2-x''^2}$. Furthermore, assuming z axis symmetry in the $x-y$ plane, we can get $r'' = x''$. Therefore, Eq. (3.38) can be expressed as follows:

$$\begin{aligned} L_{\mathrm{D}}(\lambda, r'', z) &= L_{\mathrm{D}}(\lambda, x'', z) \\ &= \int_{r''}^{R} 2\,\varepsilon(\lambda, r, z)\,\frac{r}{\sqrt{r^2-r''^2}}\,\mathrm{d}r, \end{aligned} \tag{3.39}$$

From now, the chamber inner diameter R is divided into n segments, and r_k $(k = 0, 1, \cdots, n-1)$ is defined as the kth radius. Note that $r_0 = 0$ and $r_n = R$ are the center and the inner wall of the chamber, respectively. Therefore, Eq. (3.39) can be expressed as follows:

$$\begin{aligned} L_{\mathrm{D}}(\lambda, r_k, z) &= \int_{r_k}^{R} 2\,\varepsilon(\lambda, r, z)\,\frac{r}{\sqrt{r^2-r_k^2}}\,\mathrm{d}r \\ &= \int_{r_k}^{r_{k+1}} 2\,\varepsilon(\lambda, r, z)\,\frac{r}{\sqrt{r^2-r_k^2}}\,\mathrm{d}r + \int_{r_{k+1}}^{r_{k+2}} 2\,\varepsilon(\lambda, r, z)\,\frac{r}{\sqrt{r^2-r_k^2}}\,\mathrm{d}r \\ &\quad + \cdots + \int_{r_{n-1}}^{R} 2\,\varepsilon(\lambda, r, z)\,\frac{r}{\sqrt{r^2-r_k^2}}\,\mathrm{d}r \\ &= \sum_{k'=k}^{n-1} \int_{r_k}^{r_{k+1}} 2\,\varepsilon(\lambda, r, z)\,\frac{r}{\sqrt{r^2-r_k^2}}\,\mathrm{d}r. \end{aligned} \tag{3.40}$$

Furthermore, $\varepsilon(\lambda, r, z)$ is assumed to be the first-order polynomial on the assumption of uniformity in the z axis direction, as in the following equation and in Fig. 3.8:

$$\varepsilon(\lambda, r) = \begin{cases} a_k(\lambda) + b_k(\lambda)\,r, & \text{where } r_k \le r < r_{k+1} \text{ and } k = 0, 1, \ldots, n-2 \\ & \qquad\qquad (\text{for } 0 \le r < r_{n-1}), \\ a_{n-2}(\lambda) + b_{n-2}(\lambda)\,r_{n-1} & (\text{for } r_{n-1} \le r < R). \end{cases} \tag{3.41}$$

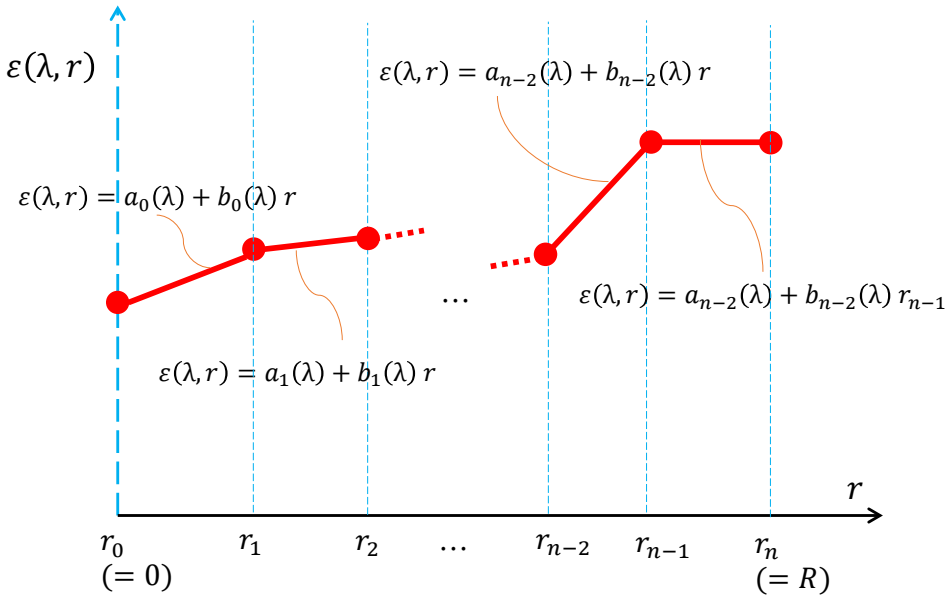

Fig. 3.8: The conceptual diagram of Eq. (3.41). Reproduced from Yuya Yamashita *et al.*, Rev. Sci. Instrum., **94**, 083503, (2023) [4], with the permission of AIP Publishing.

Equation (3.41) can be expressed for $0 \leq r < r_{n-1}$ as follows:

$$\begin{aligned} & a_k(\lambda) + b_k(\lambda)\, r_{k+1} = a_{k+1}(\lambda) + b_{k+1}(\lambda)\, r_{k+1}, \\ \Leftrightarrow \quad & a_{k+1}(\lambda) = a_k(\lambda) + [b_k(\lambda) - b_{k+1}(\lambda)] r_{k+1}, \\ \therefore \quad & a_k(\lambda) = a_0(\lambda) + \sum_{k'=0}^{k-1} [b_{k'}(\lambda) - b_{k'+1}(\lambda)] r_{k'+1}. \end{aligned} \tag{3.42}$$

Therefore, Equation (3.41) can be expressed as follows:

$$\varepsilon(\lambda, r) = \begin{cases} a_0(\lambda) + b_k(\lambda)\, r + \sum_{k'=0}^{k-1} [b_{k'}(\lambda) - b_{k'+1}(\lambda)] r_{k'+1}, \\ \qquad \text{where} \quad r_k \leq r < r_{k+1} \ \text{ and } \ k = 0, 1, \ldots, n-2 \quad (\text{for } 0 \leq r < r_{n-1}), \\ a_0(\lambda) + b_{n-2}(\lambda)\, r_{n-1} + \sum_{k'=0}^{n-3} [b_{k'}(\lambda) - b_{k'+1}(\lambda)] r_{k'+1} \qquad (\text{for } r_{n-1} \leq r < R). \end{cases} \tag{3.43}$$

Inserting Eq. (3.43) into Eq.(3.40), we get

$$
\begin{aligned}
L_{\mathrm{D}}(\lambda, r_k) &= \sum_{k'=k}^{n-1} \int_{r_k}^{r_{k+1}} 2\,\varepsilon(\lambda, r)\,\frac{r}{\sqrt{r^2 - r_k^2}}\,\mathrm{d}r \qquad = \qquad \sum_{k'=k}^{n-2} \left[\int_{r_{k'}}^{r_{k'+1}} 2\,\varepsilon(\lambda, r)\,\frac{r}{\sqrt{r^2 - r_k^2}}\,\mathrm{d}r \right] + \int_{r_{n-1}}^{r_n=R} 2\,\varepsilon(\lambda, r)\,\frac{r}{\sqrt{r^2 - r_k^2}}\,\mathrm{d}r \\
&= \sum_{k'=k}^{n-2} \left\{ \int_{r_{k'}}^{r_{k'+1}} 2\,[a_{k'}(\lambda) + b_{k'}(\lambda)\,r]\,\frac{r}{\sqrt{r^2 - r_k^2}}\,\mathrm{d}r \right\} + \int_{r_{n-1}}^{r_n=R} 2\,[a_{n-2}(\lambda) + b_{n-2}(\lambda)\,r_{n-1}]\,\frac{r}{\sqrt{r^2 - r_k^2}}\,\mathrm{d}r \\
&= 2 \sum_{k'=k}^{n-2} \left\{ \int_{r_{k'}}^{r_{k'+1}} a_{k'}(\lambda)\,\frac{r}{\sqrt{r^2 - r_k^2}}\,\mathrm{d}r \int_{r_{k'}}^{r_{k'+1}} b_{k'}(\lambda)\,\frac{r^2}{\sqrt{r^2 - r_k^2}}\,\mathrm{d}r \right\} + 2 \int_{r_{n-1}}^{r_n=R} [a_{n-2}(\lambda) + b_{n-2}(\lambda)\,r_{n-1}]\,\frac{r}{\sqrt{r^2 - r_k^2}}\,\mathrm{d}r \\
&= 2 \sum_{k'=k}^{n-2} \left[a_{k'}(\lambda)\sqrt{r^2 - r_k^2} + b_{k'}(\lambda) \left\{ \frac{r\sqrt{r^2 - r_k^2}}{4} + \frac{r_k^2}{4} \ln \left| r + \sqrt{r^2 - r_k^2} \right| \right\} \right]_{r_{k'}}^{r_{k'+1}} + 2\{a_{n-2}(\lambda) + b_{n-2}(\lambda)\,r_{n-1}\} \left[\sqrt{r^2 - r_k^2} \right]_{r_{n-1}}^{r_n=R} \\
&= 2 \sum_{k'=k}^{n-2} a_{k'}(\lambda) \left[\sqrt{r_{k'+1}^2 - r_k^2} - \sqrt{r_{k'}^2 - r_k^2} \right] + 2 \sum_{k'=k}^{n-2} b_{k'}(\lambda) \left\{ \frac{r_{k'+1}\sqrt{r_{k'+1}^2 - r_k^2} - r_{k'}\sqrt{r_{k'}^2 - r_k^2}}{4} + \frac{r_k^2}{4} \ln \left| \frac{r_{k'+1} + \sqrt{r_{k'+1}^2 - r_k^2}}{r_{k'} + \sqrt{r_{k'}^2 - r_k^2}} \right| \right\} \qquad (3.44) \\
&\quad + 2\{a_{n-2}(\lambda) + b_{n-2}(\lambda)\,r_{n-1}\} \left[\sqrt{r_n^2 - r_k^2} - \sqrt{r_{n-1}^2 - r_k^2} \right] \\
&= 2 \sum_{k'=k}^{n-2} \left[a_0(\lambda) + \sum_{k''=0}^{k'-1} [b_{k''}(\lambda) - b_{k''+1}(\lambda)] r_{k'+1} \right] \left[\sqrt{r_{k'+1}^2 - r_k^2} - \sqrt{r_{k'}^2 - r_k^2} \right] \\
&\quad + 2 \sum_{k'=k}^{n-2} b_{k'}(\lambda) \left\{ \frac{r_{k'+1}\sqrt{r_{k'+1}^2 - r_k^2} - r_{k'}\sqrt{r_{k'}^2 - r_k^2}}{4} + \frac{r_k^2}{4} \ln \left| \frac{r_{k'+1} + \sqrt{r_{k'+1}^2 - r_k^2}}{r_{k'} + \sqrt{r_{k'}^2 - r_k^2}} \right| \right\} \\
&\quad + 2 \left\{ \left[a_0(\lambda) + \sum_{k'=0}^{n-3} [b_{k'}(\lambda) - b_{k'+1}(\lambda)] r_{k'+1} \right] + b_{n-2}(\lambda)\,r_{n-1} \right\} \left[\sqrt{r_n^2 - r_k^2} - \sqrt{r_{n-1}^2 - r_k^2} \right]
\end{aligned}
$$

(continued on the next page)

(continued from the previous page)

$$
\begin{aligned}
=&2\sum_{k'=k}^{n-2}\left[a_0(\lambda)+\sum_{k''=0}^{k'-1}[b_{k''}(\lambda)-b_{k''+1}(\lambda)]r_{k'+1}\right]C_1(k',k)\ +\ 2\sum_{k'=k}^{n-2}b_{k'}(\lambda)C_2(k',k)\\
&+\ 2\left\{\left[a_0(\lambda)+\sum_{k'=0}^{n-3}[b_{k'}(\lambda)-b_{k'+1}(\lambda)]r_{k'+1}\right]+b_{n-2}(\lambda)\,r_{n-1}\right\}C_3(n,k)\\
=&2\sum_{k'=k}^{n-2}a_0(\lambda)\,C_1(k',k)\ +\left[\ 2\sum_{k'=k}^{n-2}\sum_{k''=0}^{k'-1}[b_{k''}(\lambda)-b_{k''+1}(\lambda)]r_{k'+1}\,C_1(k',k)\right]\ +\ 2\sum_{k'=k}^{n-2}b_{k'}(\lambda)C_2(k',k)\\
&+2C_3(n,k)\,a_0(\lambda)+\left\{2C_3(n,k)\sum_{k'=0}^{n-3}[b_{k'}(\lambda)-b_{k'+1}(\lambda)]r_{k'+1}\right\}\ +\ 2b_{n-2}(\lambda)\,r_{n-1}C_3(n,k)\\
=&2\sum_{k'=k}^{n-2}a_0(\lambda)\,C_1(k',k)\ +\ \left[2\sum_{k'=k}^{n-2}\sum_{k''=0}^{k'-1}b_{k''}(\lambda)r_{k'+1}\,C_1(k',k)\ -\ 2\sum_{k'=k}^{n-2}\sum_{k''=1}^{k'}b_{k''}(\lambda)r_{k'+1}\,C_1(k',k)\right]+2\sum_{k'=k}^{n-2}b_{k'}(\lambda)C_2(k',k)\\
&+\ 2C_3(n,k)\,a_0(\lambda)\ +\ \left\{2C_3(n,k)\sum_{k'=0}^{n-3}b_{k'}(\lambda)r_{k'+1}-2C_3(n,k)\sum_{k'=1}^{n-2}b_{k'}(\lambda)r_{k'+2}\right\}+\ 2b_{n-2}(\lambda)\,r_{n-1}C_3(n,k),
\end{aligned}
\tag{3.44}
$$

where C_1, C_2, C_3 are as follows, respectively,

$$
C_1(k',k)=\left[\sqrt{r_{k'+1}^2-r_k^2}-\sqrt{r_{k'}^2-r_k^2}\right],
$$

$$
C_2(k',k)=\left\{\frac{r_{k'+1}\sqrt{r_{k'+1}^2-r_k^2}-r_{k'}\sqrt{r_{k'}^2-r_k^2}}{4}+\frac{r_k^2}{4}\ln\left|\frac{r_{k'+1}+\sqrt{r_{k'+1}^2-r_k^2}}{r_{k'}+\sqrt{r_{k'}^2-r_k^2}}\right|\right\},
$$

$$
C_3(n,k)=\left[\sqrt{r_n^2-r_k^2}-\sqrt{r_{n-1}^2-r_k^2}\right].
$$

Similarly, applying Eq.(3.43) to Eq.(3.35), we obtain

$$
\begin{aligned}
L_{\mathrm{refl}}(\lambda) &= \frac{R_{\mathrm{g}}^2(\lambda)}{\pi[1-R_{\mathrm{g}}(\lambda)]\,S_{\mathrm{g}}}\,8\pi^2 H\left[\int_{r_0}^{r_1}\varepsilon(\lambda,r)\,r\,\mathrm{d}r+\int_{r_1}^{r_2}\varepsilon(\lambda,r)\,r\,\mathrm{d}r+\cdots+\int_{r_{n-1}}^{R}\varepsilon(\lambda,r)\,r\,\mathrm{d}r\right] \\
&= \frac{R_{\mathrm{g}}^2(\lambda)}{\pi[1-R_{\mathrm{g}}(\lambda)]\,S_{\mathrm{g}}}\,8\pi^2 H\sum_{k'=0}^{n-1}\int_{r_{k'}}^{r_{k'+1}}\varepsilon(\lambda,r)\,r\,\mathrm{d}r \\
&= \frac{R_{\mathrm{g}}^2(\lambda)}{\pi[1-R_{\mathrm{g}}(\lambda)]\,S_{\mathrm{g}}}\,8\pi^2 H\left[\sum_{k'=0}^{n-2}\int_{r_{k'}}^{r_{k'+1}}\varepsilon(\lambda,r)\,r\,\mathrm{d}r+\int_{r_{n-1}}^{r_n}\varepsilon(\lambda,r)\,r\,\mathrm{d}r\right] \\
&= \frac{R_{\mathrm{g}}^2(\lambda)}{\pi[1-R_{\mathrm{g}}(\lambda)]\,S_{\mathrm{g}}}\,8\pi^2 H\left\{\sum_{k'=0}^{n-2}\left[\int_{r_{k'}}^{r_{k'+1}}[a_{k'}(\lambda)\,r+b_{k'}(\lambda)\,r^2]\,\mathrm{d}r\right]+\int_{r_{n-1}}^{r_n}[a_{n-2}(\lambda)+b_{n-2}(\lambda)\,r_{n-1}]\,r\,\mathrm{d}r\right\} \\
&= \frac{R_{\mathrm{g}}^2(\lambda)}{\pi[1-R_{\mathrm{g}}(\lambda)]\,S_{\mathrm{g}}}\,8\pi^2 H\left\{\sum_{k'=0}^{n-2}\left[a_{k'}(\lambda)\frac{r^2}{2}+b_{k'}(\lambda)\frac{r^3}{3}\right]_{r_{k'}}^{r_{k'+1}}+\{a_{n-2}(\lambda)+b_{n-2}(\lambda)\,r_{n-1}\}\left[\frac{r^2}{2}\right]_{r_{n-1}}^{r_n}\right\} \\
&= \frac{R_{\mathrm{g}}^2(\lambda)}{\pi[1-R_{\mathrm{g}}(\lambda)]\,S_{\mathrm{g}}}\,8\pi^2 H\left\{\sum_{k'=0}^{n-2}\left[a_{k'}(\lambda)\frac{r_{k'+1}^2-r_{k'}^2}{2}+b_{k'}(\lambda)\frac{r_{k'+1}^3-k_{k'}^3}{3}\right]+\{a_{n-2}(\lambda)+b_{n-2}(\lambda)\,r_{n-1}\}\frac{r_n^2-r_{n-1}^2}{2}\right\} \\
&= \frac{R_{\mathrm{g}}^2(\lambda)}{\pi[1-R_{\mathrm{g}}(\lambda)]\,S_{\mathrm{g}}}\,8\pi^2 H\left\{\left[\sum_{k'=0}^{n-2}a_{k'}(\lambda)\frac{r_{k'+1}^2-r_{k'}^2}{2}+\sum_{k'=0}^{n-2}b_{k'}(\lambda)\frac{r_{k'+1}^3-k_{k'}^3}{3}\right]+[a_{n-2}(\lambda)+b_{n-2}(\lambda)\,r_{n-1}]\frac{r_n^2-r_{n-1}^2}{2}\right\} \\
&= \frac{R_{\mathrm{g}}^2(\lambda)}{\pi[1-R_{\mathrm{g}}(\lambda)]\,S_{\mathrm{g}}}\,8\pi^2 H \\
&\quad\cdot\left\{\sum_{k'=0}^{n-2}\left[a_0(\lambda)+\sum_{k''=0}^{k'-1}[b_{k''}(\lambda)-b_{k''+1}(\lambda)]r_{k''+1}\right]C_4(k')+\sum_{k'=0}^{n-2}b_{k'}(\lambda)\,C_5(k')\right. \\
&\qquad\left.+\left[a_0(\lambda)+\sum_{k'=0}^{n-3}[b_{k'}(\lambda)-b_{k'+1}(\lambda)]r_{k'+1}+b_{n-2}(\lambda)\,r_{n-1}\right]C_4(n-1)\right\} \\
&\qquad\qquad \text{where } C_4(k')=\frac{r_{k'+1}^2-r_{k'}^2}{2},\ C_5(k')=\frac{r_{k'+1}^3-k_{k'}^3}{3}
\end{aligned}
\tag{3.45}
$$

(continued on the next page)

(continued from the previous page)

$$= \frac{R_g^2(\lambda)}{\pi[1-R_g(\lambda)]\,S_g}\, 8\pi^2 H \cdot \Bigg[\sum_{k'=0}^{n-2} a_0(\lambda) C_4(k') + \sum_{k'=0}^{n-2} \sum_{k''=0}^{k'-1} b_{k''}(\lambda) r_{k''+1} C_4(k') - \sum_{k'=0}^{n-2} \sum_{k''=1}^{k'} b_{k''}(\lambda) r_{k''} C_4(k') + \sum_{k'=0}^{n-2} b_{k'}(\lambda)\, C_5(k') + a_0(\lambda)\, C_4(n-1) + \sum_{k'=0}^{n-3} b_{k'}(\lambda)\, r_{k'+1} C_4(n-1) - \sum_{k'=1}^{n-2} b_{k'}(\lambda) r_{k'} C_4(n-1) \;+\; b_{n-2}(\lambda)\, r_{n-1} C_4(n-1) \Bigg]. \tag{3.45}$$

Assuming that the z axis direction is independent, Eq. (3.36) can be expressed as follows:

$$L_{\mathrm{I}}(\lambda, r_k) = L_{\mathrm{D}}(\lambda, r_k) + L_{\mathrm{refl}}(\lambda). \tag{3.46}$$

Therefore, $L_{\mathrm{I}}(\lambda, r_k)$ can be expressed as the function of $a_0(\lambda)$ and $b_k(\lambda)$, where $L_{\mathrm{I}}(\lambda, r_k)$ is the kth line-of-sight of the spectral radiance on the vacuum side surface of the window, which is equal to $L_{\mathrm{I}}(\lambda)$ of Eq.(3.20).

In this study, $a_0(\lambda)$ and $b_k(\lambda)$ were obtained based on the numerical fitting of the calculated and experimental of $L_{\mathrm{I}}(\lambda, r_k)$. Furthermore, $\varepsilon(\lambda, r_k)$ were calculated from the obtained $a_0(\lambda)$ and $b_k(\lambda)$.

3.4 Plasma diagnosis

3.4.1 Experimental condition of plasma diagnosis

Figure 3.1 shows that Argon (Ar) gas of 10 SCCM was supplied into the chamber via a mass flow controller. Furthermore, the chamber was evacuated using turbomolecular and rotary pumps. The base pressure of the vacuum chamber was 1.6×10^{-3} Pa. The 13.56 MHz RF power of 300 W was applied to the RF antenna to generate the plasma, while the total discharge pressure was set at $p = 1.0$ Pa.

3.4.2 OES measurement

The line-of-sight k dependence of the spectral radiance on the air side surface of the view window, $L'_k(\lambda)$, along the line-of-sight was measured using a lens (CLA-SMA2, B&W Tek), an optical fiber (FPC-600-0.2-1.0-SRUV, B&W Tek; core diameter = 600 μm, NA = 0.22), and a spectrometer (MS3504i, SOL instruments) with the charge coupled device (CCD) detector (DU420A-OE, Andor Technology). The angle of view (half angle) of the focusing optics is 1.909°, and the beam waist diameter is 4.059 mm. The line-of-sights were set oblique angles to normal of the view window, as shown in Fig. 3.9 and Table 3.1 due to displaced Snell's law, as discussed in Sec. 3.3.1. $L'_k(\lambda)$ was measured by scanning the line-of-sight while maintaining the discharge. Note that the spectral radiance of the spectrometer was calibrated using a spectral radiance standard surface, which was realized using a spectral irradiance standard lamp (JPD100V500WCS, Ushio Lighting) and a standard diffuse reflector (SG 3051, SphereOptics).

$L'_k(\lambda)$ was calculated by using Eq. (3.20). Furthermore, $\varepsilon_k(\lambda)$ on the radial position was calculated as shown in Sec. 3.3.4.

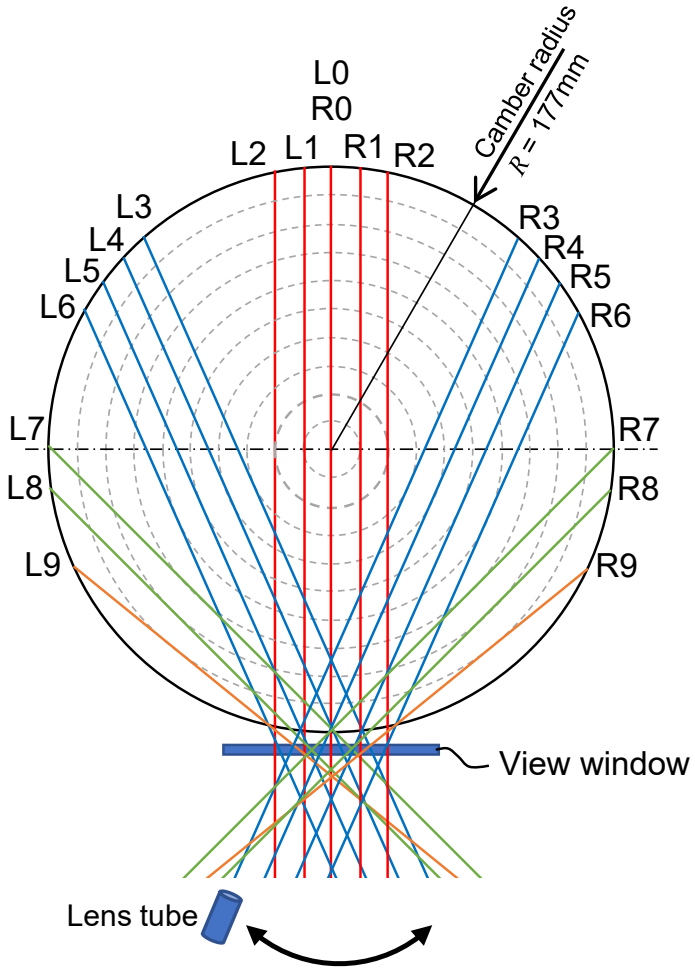

Fig. 3.9: The schematic diagram of the line of sight of OES measurement. Here, "L l" and "R l" denote the lth lines of sight on left and right sides, respectively. Note that the line of sight placement was set the same as in Ref [1]. Reproduced from Rev. Sci. Instrum., **94**, 083503, (2023) [4], with the permission of AIP Publishing.

On the each position k, the dependence of the excited-level number density on the radius was calculated from the optical emission lines based on the lines listed in Table 3.2. The excited-level density n_{j*} of level $j*$, which is designated by the Racah notation, is expressed based on the spontaneous emission from level $j*$ to level $i*$ as follows:

$$4\pi \int_{j*\to i*} \varepsilon_{j*\to i*}(\lambda)\,\mathrm{d}\lambda = h\,\frac{c}{\lambda(j*,i*)}\,A(j*,i*)\,\Lambda_{j*,i*}\,n_{j*}, \tag{3.47}$$

where $\varepsilon_{j*\to i*}$ is the spectral emission coefficient of the transition from level $j*$ to level $i*$, the integral on the left-hand side is measured over the spectral profile for transition from level $j*$ to level $i*$, h is the Planck constant, c is the speed of light, $\lambda(j*,i*)$ is the wavelength of the transition from level $j*$ to level $i*$, $A(j*,i*)$ is Einstein's A coefficient of the transition from level $j*$ to level $i*$, and $\Lambda_{j*,i*}$ is the optical escape factor of the transition of level $j*$ to level $i*$. In the Ar CR model, the excitation levels are grouped for excitation states with similar excitation energies; $\Lambda_{j*,i*}$ is considered only for transitions to the ground level and is assumed to be optically thin for transitions to excited levels other than the ground level. The number density n_j of excited-level j, which is specified by the Ar CR model, can be expressed as follows:

$$\frac{n_j}{g_j} = \frac{n_{j*}}{g_{j*}}, \tag{3.48}$$

where g_j is the statistical weight of level j, which is specified by the Ar CR model; g_{j*} is the statistical weight of level $j*$, which is specified by the Racah notation; and level $j*$ belong to the same level j of the Ar CR model. In this study, the reduced population density n_j was calculated by optical emission line spectra.

The Ar CR model [50] was employed to calculate T_e and N_e from the excited-level number densities. The Ar CR model [50] is an excitation-kinetic model that provides a reduced population density distribution n_i / g_i as a function of T_e [electron energy distribution function (EEDF) was assumed to be Maxwellian], N_e, atomic temperature T_a, ion density N_I, and plasma radius r. The rate equation is expressed as

$$\begin{aligned}\frac{\mathrm{d}n_i}{\mathrm{d}t} = &\sum_{j=i+1}^{65}\left[-\{C(i,j)N_\mathrm{e}n_i + K(i,j)n_1n_i\} + \left\{F(j,i)N_\mathrm{e}n_j + L(j,i)n_1n_j + A(j,i)\Lambda_{j,i}n_j\right\}\right] \\ &+ \sum_{j=1}^{i-1}\left[\left\{C(j,i)N_\mathrm{e}n_j + K(j,i)n_1n_j\right\} - \left\{F(i,j)N_\mathrm{e}n_j + L(j,i)n_1n_i + A(i,j)\Lambda_{i,j}n_i\right\}\right] \\ &- \{S(i)N_\mathrm{e}n_i + V(i)n_1n_i\} \\ &+ [\{O(i)N_\mathrm{e} + W(i)n_1 + R(i)\Lambda_i\}]N_\mathrm{e}N_\mathrm{I} - [D(i) + B(i)] \qquad (i = 2,3,\cdots),\end{aligned} \tag{3.49}$$

Table 3.2: Optical emission lines for OES measurement. Reproduced from Yuya Yamashita *et al.*, Rev. Sci. Instrum., **94**, 083503, (2023) [4], with the permission of AIP Publishing.

Ritz wavelength	Upper level				Lower level				A coefficient
in Air	Vlček [50]		Racah [66]		Vlček [50]		Racah [66]		$A(j*,i*)$
$\lambda(j*,i*)$ [nm] [66]	level j	g_j	level $j*$	g_{j*}	level i	g_i	level $i*$	g_{i*}	[s^{-1}] [66]
750.38	11	1	$4p'[1/2]_0$	1	5	3	$4s'[1/2]_1^\circ$	3	4.50×10^7
763.51	7	20	$4p[3/2]_2$	5	2	5	$4s[3/2]_2^\circ$	5	2.45×10^7
794.81	8	8	$4p'[3/2]_1$	3	4	1	$4s'[1/2]_0^\circ$	1	1.86×10^7
810.37	7	20	$4p[3/2]_1$	3	3	3	$4s[3/2]_1^\circ$	3	2.50×10^7
811.53	7	20	$4p[5/2]_3$	7	2	5	$4s[3/2]_2^\circ$	5	3.30×10^7
826.45	9	3	$4p'[1/2]_1$	3	5	3	$4s'[1/2]_1^\circ$	3	1.53×10^7
840.82	8	8	$4p'[3/2]_2$	5	5	3	$4s'[1/2]_1^\circ$	3	2.23×10^7
842.46	7	20	$4p[5/2]_2$	5	3	3	$4s[3/2]_1^\circ$	3	2.15×10^7
852.14	8	8	$4p'[3/2]_1$	3	5	3	$4s'[1/2]_1^\circ$	3	1.39×10^7
922.45	7	20	$4p[3/2]_2$	5	5	3	$4s'[1/2]_1^\circ$	3	5.00×10^6
978.45	7	20	$4p[5/2]_2$	5	5	3	$4s'[1/2]_1^\circ$	3	1.47×10^6

In Eq. (3.49), C and F are electron-collisional excitation and de-excitation rate coefficients, respectively; K and L are atomic-collisional excitation and de-excitation rate coefficients, respectively; A is the radiative transition probability; S and O are atomic-collisional ionization and electron three-body recombination rate coefficients, respectively; V and W are atomic-collisional ionization and atomic three-body recombination rate coefficients, respectively; R is the radiative recombination rate coefficient; B is the rate of generation of metastable Ar_2 molecules; and D is the diffusion loss of the metastable Ar atom. The rate coefficients were calculated using the method of Vlcek [50]. The quasi-stationary approximation ($\mathrm{d}/\mathrm{d}t = 0$) of Eq.(3.49) yields a set of simultaneous equations with T_e and N_e as input variables and n_i as the output variables. T_e and N_e were determined by fitting the n_i/g_i distributions based on OES measurements with the value obtained from the Ar CR model. The objective function f_I of the fitting is as follows:

$$f_\mathrm{I}(T_\mathrm{e},N_\mathrm{e}) = \sum_{i\in\mathrm{I}} \left(\frac{n_{i\mathrm{model}}(T_\mathrm{e},N_\mathrm{e})/g_i}{n_{i\mathrm{OES}}/g_i} - 1 \right)^2 . \tag{3.50}$$

where $n_{i\mathrm{model}}(T_\mathrm{e},N_\mathrm{e})/g_i$ is the value of n_i/g_i from the Ar CR model, whereas $n_{i\mathrm{OES}}/g_i$ is the experimental value obtained by OES measurement. T_e and N_e are obtained by fitting minimizing f_I.

In contrast to the previous studies [52] that aimed at diagnosis with a low-wavelength resolution spectrometer, this study aimed at accurate diagnosis based on multiple emission lines obtained with a high-wavelength resolution spectrometer that had a wavelength resolution of

0.22 nm (FWHM). The 11 emission lines listed in Table 3.2 were adopted for the diagnosis. The parameters assumed were $T_a = 400$ K and $N_I = N_e$. The plasma column radius for diffusion calculations was assumed to be 96.5 mm, which corresponds to the half value of the inner minimum height of the chamber. The EEDF was assumed to be Maxwellian in nature.

3.4.3 Probe measurement

A single Langmuir probe was employed to obtain T_e and N_e for comparison with those obtained from OES-based diagnosis. A tungsten wire tip ($\Phi 1.55 \times L 0.50$ mm) probe was equipped with a push-pull linear shift mechanism, allowing for scanning of the measurement position in the diameter direction of the chamber. T_e was determined from the slope of the current-voltage characteristics, while N_e was determined from the electron saturation current. Note that OES measurements were performed without the probe inserted.

3.5 Results and discussion

Figure 3.10 shows the measurement results of the spectral reflectance of the inner wall of the chamber (Sec. 3.3).

Above 400 nm, the spectral reflectance increased monotonically. The variation range of spectral reflectance at the same wavelength was up to 19.6 % (λ = 750.3–978.6 nm, wavelength range used for diagnosis in this study). Note that the noise observed at the wavelengths below 400 nm is due to the small relative spectral distribution of the incandescent lamp. Note that the reason for the small incremental changes in spectral reflectance on the same curve is considered for the signal-to-noise ratio of the radio-photometric system. Furthermore, the upper part of the chamber of this ICP system had Φ 205 mm quartz window, where the antenna was placed outside the window. Therefore, the light transmitted outside the window was attenuated by multiple reflections. It is assumed that this is a type of light trap behavior, which can be attributed to the low reflectance.

Figures 3.11 and 3.12 show the dependence of the spectral emission coefficient, which is the calculation result in Sec.3.3.4 based on the experiment. It is clear that by not considering reflections at the wall in this system, the spectral emission coefficient results would result in error, which would be up to 4.1 %. In particular, the effect of multiple reflections on the chamber inner wall was found to be significant at locations where the spectral emission coefficient was small. Note that in the spectral radiance calibration setup, which is the same type of this study,

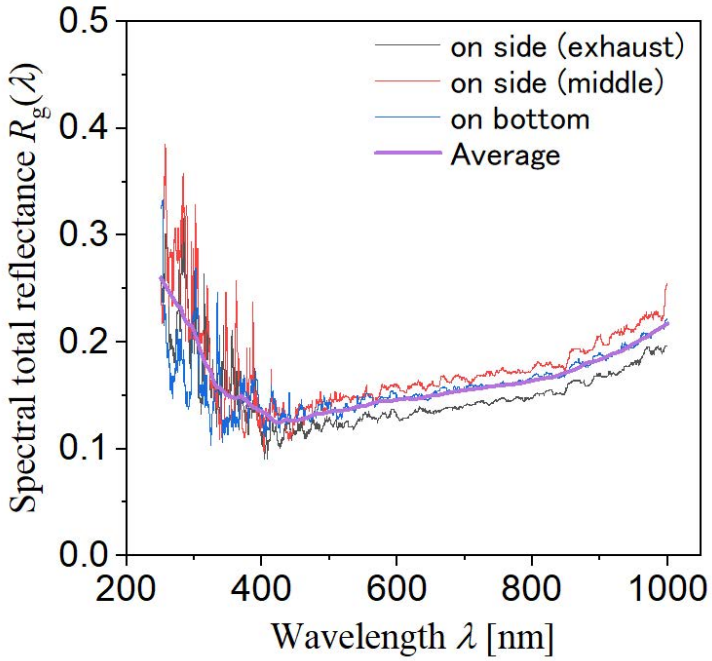

Fig. 3.10: The spectral reflectance of the inner wall of the chamber: “on side (exhaust)”, “on side (middle)”, and “on bottom” denote the location of the reflector that was set at side or bottom of the chamber, as shown in Fig. 3.7. "Average" denotes the averaged and Savitzky-Golay smoothed data of the their spectral reflectance that were employed to calculate the spectral radiance. [This figure was modified from Ref. 20. Reproduced with permission from the work of Yamashita *et al.*, in Proceedings of 43rd International Symposium on Dry Process (DPS2022) (43rd International Symposium on Dry Process Organizing Committee, 2022), pp. 47-48 [67]. Copyright 2022 43rd International Symposium on Dry Process Organizing Committee.] Reproduced from Yuya Yamashita *et al.*, Rev. Sci. Instrum., **94**, 083503, (2023) [4], with the permission of AIP Publishing.

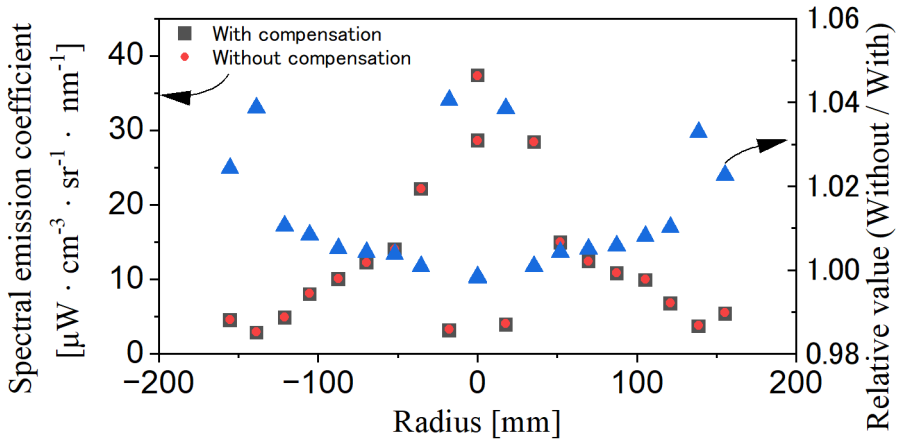

Fig. 3.11: The dependence of the spectral emission coefficient of 750.4 nm on the position. "With" and "without compensations" denote considering or not the multiple reflectance on the chamber inner wall, respectively. Reproduced from Yuya Yamashita *et al.*, Rev. Sci. Instrum., **94**, 083503, (2023) [4], with the permission of AIP Publishing.

the expanded uncertainty (coverage factor $k = 2$) of spectral radiance on the standard surface is reported to be 3.9–7.4 % [68].

Figure 3.13 shows the reduced population density distribution, which was calculated from the OES experiment based on Eq. (3.47).

Figures 3.14 shows the T_e diagnostic results by OES. The difference between the diagnostic results of T_e with and without reflectance correction was up to 0.6 %. Figures 3.15 shows the N_e diagnostic results by OES. The difference between the diagnostic results of N_e with and without reflectance correction was up to 3.1 %.

Figure 3.16 shows the diagnostic results for the probe. T_e exhibits a convex distribution to position x. The positions of these peaks approximately correspond to the position of the ICP antenna. Meanwhile, N_e exhibited a convex distribution centered at $x = 17$ mm. Both T_e and N_e exhibited asymmetric characteristics because the ends of the ICP antenna on the positive side of the x axis are not perfect spiral-shaped. However, the diagnostic results of the OES and probe measurement differences are $\sim$1 eV for T_e and ten times for N_e, respectively. One of the causes of the difference that is to be considered is the disturbances caused by the insertion of the probe. That is, in this study, the probe was inserted from the port on the x axis positive side wall to the x axis negative side direction. The most part of the probe, except for the tip, is covered by a grounded stainless steel sleeve. Therefore, the probe insertion affects the electromagnetic field distribution of the plasma. It is reported that the calculated electron temperatures of the probe and OES in a 1 Pa argon inductively coupled plasma differ by about 0.7 eV [69]. Therefore, it is possible that the disturbance was larger on the negative side of the x axis.

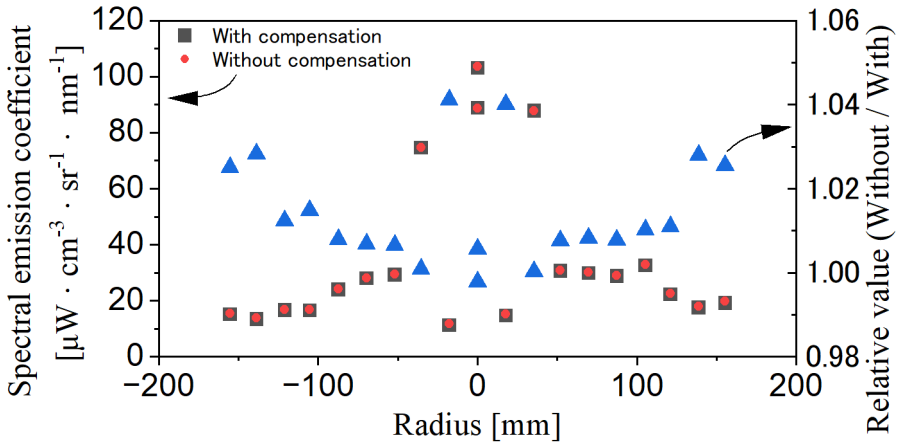

Fig. 3.12: The dependence of the spectral emission coefficient of 811.2 nm on the position. "With" and "without compensations" denote considering or not the multiple reflectance on the chamber inner wall, respectively. Reproduced from Yuya Yamashita *et al.*, Rev. Sci. Instrum., **94**, 083503, (2023) [4], with the permission of AIP Publishing.

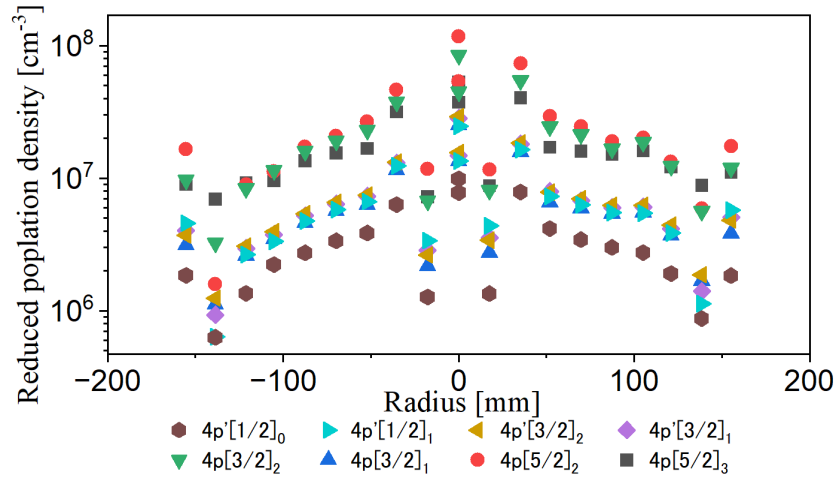

Fig. 3.13: The dependence of the reduced population density distribution on the position. This result was calculated based on OES measurement with compensation of the reflection on the chamber inner wall. Reproduced from Yuya Yamashita *et al.*, Rev. Sci. Instrum., **94**, 083503, (2023) [4], with the permission of AIP Publishing.

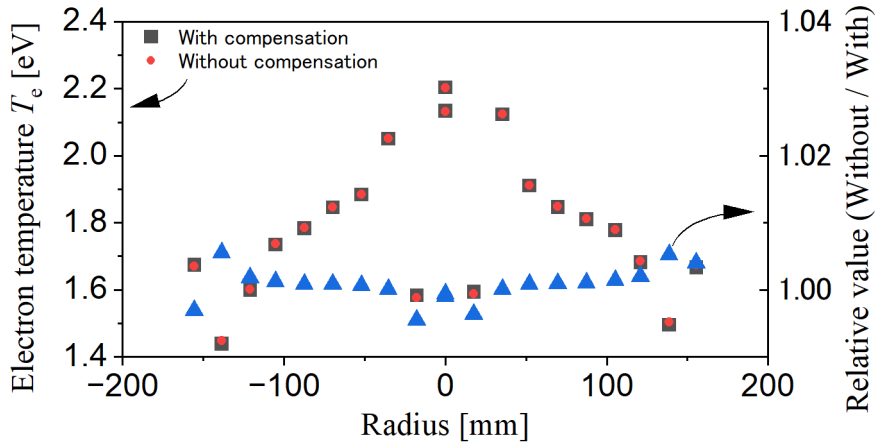

Fig. 3.14: The diagnostic results of the electron temperature by OES measurement. "With" and "without compensations" denote considering or not the multiple reflectance on the chamber inner wall, respectively. Reproduced from Yuya Yamashita *et al.*, Rev. Sci. Instrum., **94**, 083503, (2023) [4], with the permission of AIP Publishing.

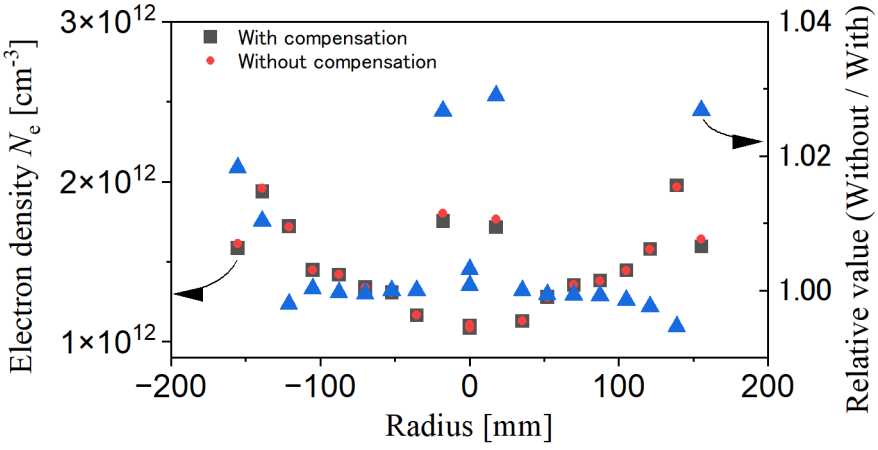

Fig. 3.15: The diagnostic results of the electron density by OES measurement. "With" and "without compensation" denote considering or not the multiple reflectance on the chamber inner wall, respectively. Reproduced from Yuya Yamashita *et al.*, Rev. Sci. Instrum., **94**, 083503, (2023) [4], with the permission of AIP Publishing.

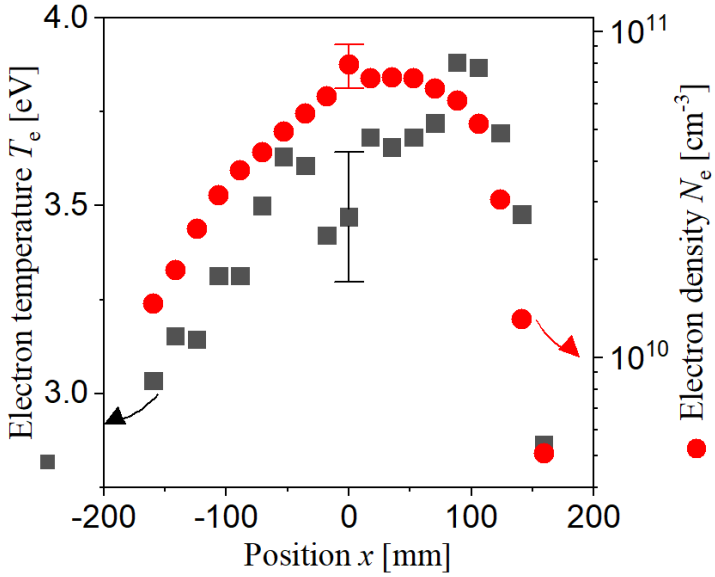

Fig. 3.16: The diagnostic results of the probe measurement. The error bars denote minimum and maximum values of eight repeated measurements [67]. Reproduced with permission from the work of Yamashita *et al.*, in Proceedings of 43rd International Symposium on Dry Process (DPS2022) (43rd International Symposium on Dry Process Organizing Committee, 2022), pp. 47-48 [67]. Copyright 2022 43rd International Symposium on Dry Process Organizing Committee.

The electromagnetic field distribution of the ICP apparatus was simulated with Femtet, Murata Software Co., Ltd. based on the geometric model, as shown in Fig. 3.17.In the simulation, the electromagnetic field distribution radiated from the antenna was calculated when a high frequency current with an applied frequency of 13.56 MHz and a power of 300 W (the same as in the experiment) was applied to the antenna. For the calculation, the chamber, the antenna shield box, and the quartz window were modeled, as shown in Fig. 3.17. Note that this simulation assumes a vacuum in the chamber and does not consider space-charge effects.

Figures 3.18 and 3.19 show the electromagnetic field strength distributions on the x - z planes at $y = 0$ mm. In the ICP apparatus structure, the quartz window was smaller than the diameter of the discharge chamber, and the window flange, which was grounded, was placed on the inside of the chamber along the diameter. It can be considered that the electromagnetic field is distorted by the grounded flange that entered inward immediately below the quartz window. This is the reason for the formation of the convex spatial electromagnetic field distribution.

Figure 3.20 shows the electromagnetic field strength distributions on the x - y planes at $z = 99$ mm (directly below the quartz window). Because of the asymmetric shape of the antenna, the electromagnetic field is also asymmetric. This is the cause of the x-directional left-right

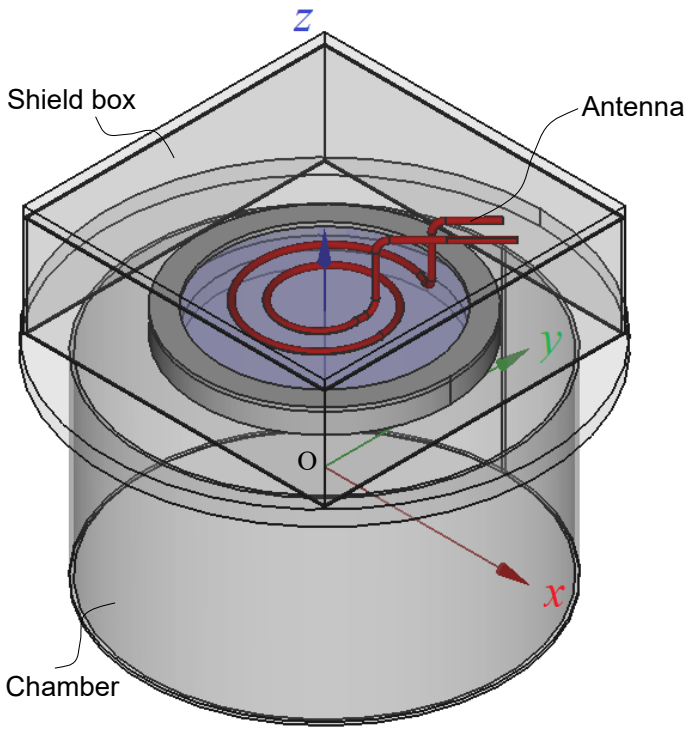

Fig. 3.17: Geometric model for electromagnetic field simulation of the ICP apparatus. The origin of the coordinate axis is the center of the chamber. Reproduced from Yuya Yamashita *et al.*, Rev. Sci. Instrum., **94**, 083503, (2023) [4], with the permission of AIP Publishing.

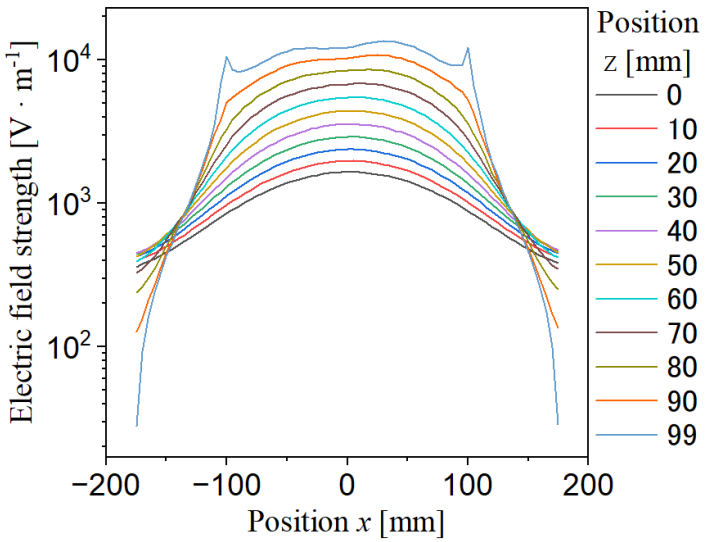

Fig. 3.18: Electric field strength distribution on the x - z plane at $y = 0$mm of the ICP apparatus. Reproduced from Yuya Yamashita *et al.*, Rev. Sci. Instrum., **94**, 083503, (2023) [4], with the permission of AIP Publishing.

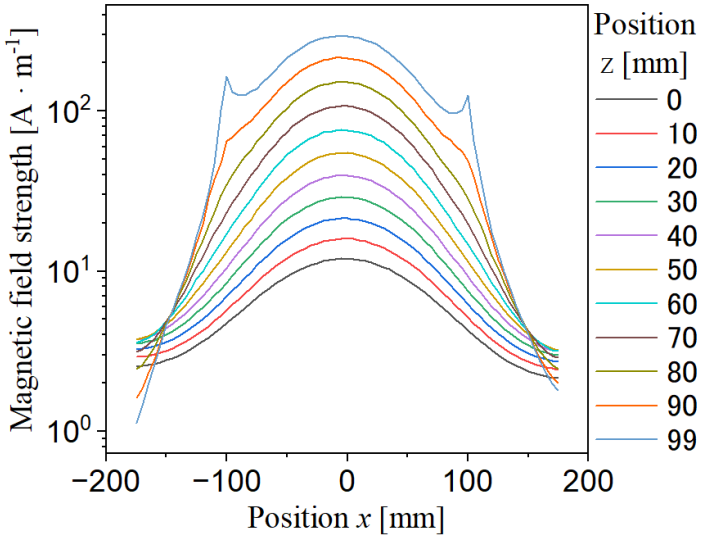

Fig. 3.19: Magnetic field strength distribution on the x - z plane at $y = 0$mm of the ICP apparatus. Reproduced from Yuya Yamashita *et al.*, Rev. Sci. Instrum., **94**, 083503, (2023) [4], with the permission of AIP Publishing.

asymmetry in T_e and N_e, as shown in Figs. 3.14 – 3.16.

Figure 3.21 shows the horizontal component of the magnetic field strength distributions which is shown in Fig. 3.19. The horizontal component of the magnetic field showed an M-shaped magnetic field at $z = 0$.

The study of the electromagnetic field of 13.56 MHz RF ICP in a rectangular chamber was reported by Hopwood *et al.* [70]. In their study, a rectangular chamber ($27 \times 27 \times 13$ cm^3) was employed, and a quartz window smaller than the top of the chamber was used, similar to that in the present study. A rectangular spiral antenna was placed outside the quartz window, and a permanent magnet for confinement was placed inside the chamber. The result of electromagnetic field calculations and magnetic probe measurements reported an M-shaped magnetic field strength distribution in its horizontal component. It concluded that the magnetic field strength decreased exponentially along the z direction from the antenna because the charged particles absorb power owing to non-collisional heating.

The induced electric field is generated by a high-frequency magnetic field due to Faraday's law. It has been reported that the electromagnetic field caused by the induced electric and magnetic fields induces a drift of $\boldsymbol{v} \times \boldsymbol{B}$ in the electrons [71], where $\boldsymbol{v}$ is the circumferential component of the velocity of electron. Hence, an electron drift to downstream of the chamber (the negative side of the z axis) will occur. The mean free path of electrons at the pressure in this experiment was estimated to be 39.8 mm. This estimation suggests that fast electrons

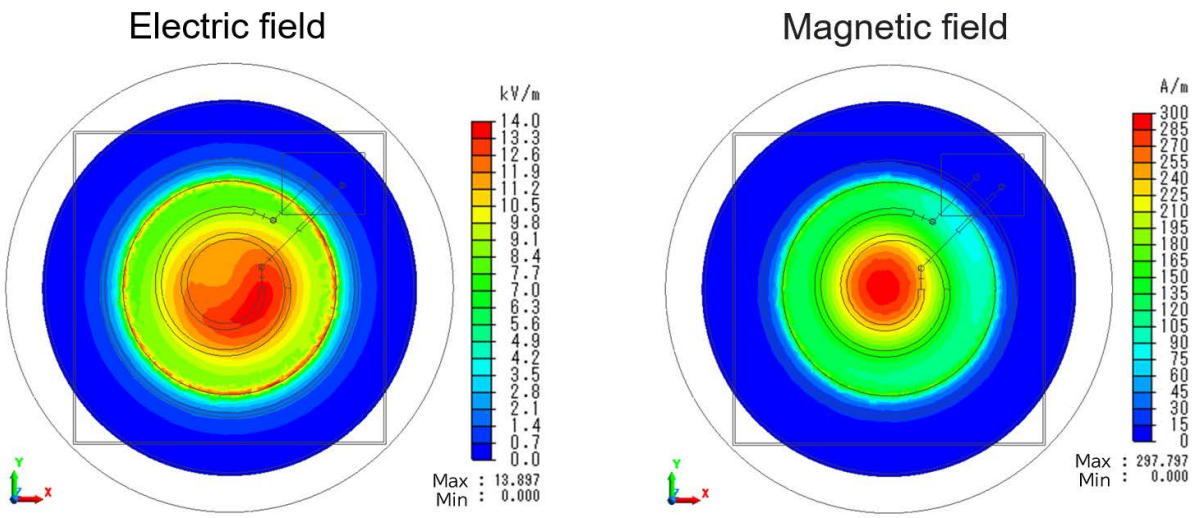

Fig. 3.20: Electromagnetic field strength distribution on the $z = 99$mm plane (just below the window) of the ICP apparatus. Reproduced from Yuya Yamashita *et al.*, Rev. Sci. Instrum., **94**, 083503, (2023) [4], with the permission of AIP Publishing.

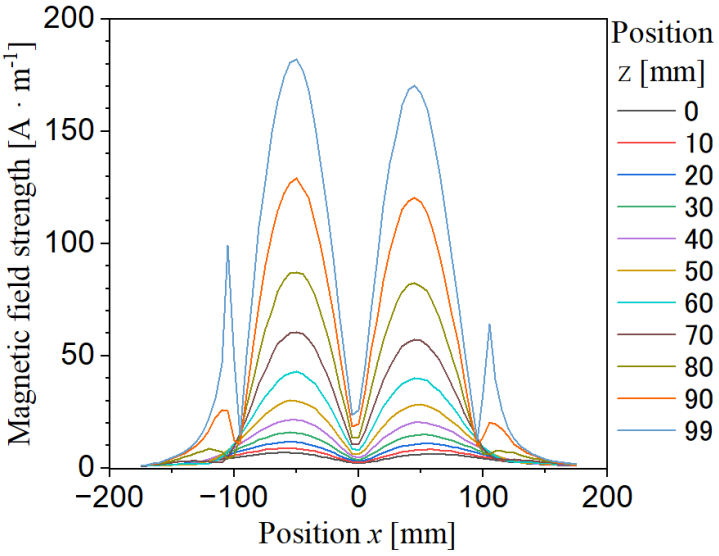

Fig. 3.21: Horizontal component of the magnetic field strength distribution on the x - z plane at $y = 0$mm of the ICP apparatus. Reproduced from Yuya Yamashita *et al.*, Rev. Sci. Instrum., **94**, 083503, (2023) [4], with the permission of AIP Publishing.

heated by induced electric field just below the upper quartz window reach the middle of the chamber without much collisions with Ar atoms. Therefore, an convex distribution of electron temperature was observed even at the middle region of the chamber ($z = 0$ mm), while the electromagnetic simulation result shows that convex magnetic field strength distribution only starts below the upper middle window. Therefore, the magnetic field distribution observed just below the upper glass window (Fig. 3.19) is considered to be observed as an convex distribution of electron temperature because the fast component of the electrons reached even at the center of the chamber ($z = 0$), which is the diagnostic view position.

However, the electromagnetic field simulations in this study did not consider space charge. It is conceivable that the electromagnetic field distribution may change due to space charge. Analysis of gas dynamics in the electromagnetic field, which was not considered in this study, is also a future issue. Other issues are to verify the electron energy distribution function assumed as Maxwell distribution and to elucidate the mechanism of spatial distribution by electromagnetic field analysis considering space-charge effects and gas dynamics.

However, in the present study, both the assumption of uniformity in the z axis direction and the analysis of emission spectroscopy measurements were performed. Therefore, the possibility of differences in diagnostic results due to the z axis position dependence of spectral emission coefficients remains an issue. The diagnosis of three-dimensional spatial distribution by tomographic measurement is a future issue.

3.6 Conclusion

A method for measuring the spectral reflectance of the inner walls of the chamber was proposed, and its application to the ICP measurement was demonstrated. The effect of the reflected light from the chamber inner wall on OES measurements is discussed. Furthermore, the spectral emission coefficient calculation method was considered with the reflected light from the chamber inner wall. The radial dependence of T_e and N_e was diagnosed by OES measurement based on the proposed method. The Langmuir probe results revealed the effect of the antenna geometry on T_e and N_e. Furthermore, the electromagnetic simulation result suggested that the placement of the antenna and window affected T_e and N_e distribution. The evaluation of the effect of uncertainties in radiophotometry and in the reaction cross section and constants in the collisional radiation model on the electron temperature and electron density is a future issue. Another issue is to elucidate the mechanism of spatial distribution by electromagnetic

field analysis considering space-charge effects and gas dynamics. In this study, we assumed axis symmetry, but spectral reflectance correction in tomographic measurements is also a future issue.

Chapter 4

Spatial distribution diagnosis of electron temperature and density of argon inductively coupled plasma by tomographic optical emission spectroscopic measurement and collisional-radiative model [5]

This chapter is reproduced from Yuya Yamashita *et al.*, J. Vac. Sci. Technol. A, **42**, 023003, (2024) [5] with permission from the American Vacuum Society (AVS); unless otherwise noted.

4.1 Introduction

In recent years, the field of plasma processing has seen progress in the size of workpieces, the miniaturization of processed structures, and high aspect ratios. As a result, there is a growing demand for diagnostics of the spatial distribution of plasma macroparameters. Indeed, there has been an increasing number of reports on the diagnosis of the spatial distribution of plasma by tomographic measurement. Optical emission spectroscopic (OES) measurement is a simple noncontact diagnostic method that can be realized using an experimental system and is suitable for performing real-time measurements of processing plasmas. Diagnosis of the spatial distribution of plasma using tomography and emission spectroscopy, specifically in the field of fusion reactor plasmas [72], has been considered for a long time. Inverse integral calculations, such as the Radon transform, have previously been utilized, and with improvements in computer performance, some studies have also used discrete tomography [73].

In a prior study [74] on air plasma arc jet, simultaneous five-line-of-sight spectroscopy was

performed by placing several mirrors inside the vessel and guiding the reflected light to a lens placed in front of the entrance slit of the spectrometer. The study diagnosed the excitation temperature distribution as well as the rotational and vibrational temperatures. In the prior study, a diffraction grating movable polychromator was used. This facilitates measurement over a wide wavelength range with high wavelength resolution. However, a fixed reflector and mirror are used as the incident optical system to the spectrometer, which limits the number of lines-of-sight. In addition, the complexity of the incident optics makes it difficult to apply this method to process plasmas at a reduced pressure.

In Barni *et al.*'s study [75] of toroidal field confined plasmas, 19 lines-of-sight were positioned. Each of the lines-of-sight was taken sequentially at different times. The excitation temperature of the hydrogen plasma was thus diagnosed. Tomographic measurements with a single line-of-sight spectrometer were achieved by taking multiple random line-of-sight measurements and averaging the results. However, the method did not acquire all the lines-of-sight simultaneously. In that method, the uncertainty of the reconstructed image may increase due to plasma time evolution.

An example of tomographic optical emission spectroscopy of an inductively coupled plasma [76, 77] has been reported. As the result of spectral tomography, the spatial distribution of the excited-level number density distribution was obtained. In the prior study, a single fiber that had a position-variable lens head with a four-axis robot was employed as the input optical system to the monochromator. The system deserves special mention for its ability to change observation positions quickly and freely. However, the system was mechanically complicated.

In low-temperature weakly ionized process plasmas, diagnostics of electron temperature T_e and density N_e are important [9]. However, there are few reported cases of T_e and N_e by tomography measurements in weakly ionized plasmas. Moreover, most of them employ the line-pair method, which is extremely undesired for non-equilibrium ionized plasmas.

Tomographic OES measurements were performed on arc plasmas by arranging a photometric system with a plasma source on the rotation stage and a movable one-line-of-sight lens [78]. The temperature, ionization coefficient, electron (ion) density, and atomic density were obtained using the line-pair method.

Rathore *et al.* [79] entailed tomographic OES measurements on microwave-induced plasma using eight pinhole cameras with wavelength filters. The spatial distributions of the T_e and N_e were obtained by assuming a coronal equilibrium.

Gonzalez-Fernandez *et al.* performed tomographic optical emission spectroscopy in a linearly magnetized plasma system with 49 lensed fibers [80]. T_e and N_e were obtained using the line-pair method with the assumption of corona model.

However, these reports assume simplified excitation kinetics. Introducing that assumption has the advantage of facilitating a rough understanding of atomic-molecular processes and contributes to reducing the computational complexity of excitation kinetic calculations. On the other hand, it limits the applicable plasma macroparameters; therefore, there are limits to the types of plasma (for ionized plasma or recombination plasma) where the applied excitation kinetics is validated [42].

The collisional-radiative (CR) model is a type of excitation kinetic model that takes macroparameters such as the temperature (of electrons, atoms, and ions), density (of electrons, atoms, and ions), and pressure as inputs, calculates the rates of various elementary processes, and outputs an excited-level number density distribution by analyzing the rate equations. In principle, the CR model can be applied to a wide range of macroparameters, making it a highly versatile excitation kinetic model. Experimental data from tomographic OES measurements must be analyzed by a CR model that can faithfully describe atomic and molecular processes. However, only one study using such a strategy has been reported [81], where in tomographic optical emission spectroscopy was performed in the plume region of a Hall-thruster Ar plasma using radon conversion. In the study, the Hall-thruster on a rotating and $x-y$ (horizontal) stages was installed in a vacuum chamber (diameter: 1.5 m, length: 3.0 m). A fiber with a lens on the z (vertical) stage was also installed in the vacuum chamber. Spectra were took for every 10° rotations of the stage. The imaging was repeated at 69 points by scanning the x stage; in total, $1242 (= 69 \times 10)$ line-of-sight of measurements sequentially. Through spectral tomographic analysis and CR modeling, the x-y distributions of T_e and N_e were diagnosed. It was noted that the time difference between acquiring the spectra could be a source of increased uncertainty in the reconstruction.

In the field of semiconductor processing, various plasmas with different temperatures, pressures, and principles are in general use [82]. However, spatial *in situ* diagnoses applicable to these plasmas have not been realized [83]. With the above background, plasma diagnostics based on the combination of spectroscopic tomography measurements and CR modeling should be applied to semiconductor process plasmas.

Our study aims to diagnose the spatial distribution of T_e and N_e in plasmas by analyzing the

spatial distribution of the spectral emission coefficients of plasmas obtained using tomographic emission spectroscopy measurements, based on a CR model. An argon low-pressure discharge plasma generated by an inductively coupled plasma system is used as the experimental target. The basic characteristics of plasma are observed. The findings will serve as a basis for future plasma experiments on other gas species. The present study aims to realize diagnosis that has a more noninvasive experimental system and a more versatile atomic and molecular process analysis.

The feature of the experimental system is that a radiometric system was constructed to simultaneously acquire spectra of 18 lines-of-sight, including intersecting lines-of-sight. Uncertainties of reconstructed image due to time fluctuations will prevent by acquiring all line-of-sight lines at the same time. Spectral radiance is observed by lenses placed outside the chamber through the windows. This eliminates the need to place the optical system in a vacuum and reduces the observation window area of the device, making it more applicable to actual process equipment.

The first feature of the analysis is that the CR model was employed for the atomic and molecular process model to achieve an analysis. This enables the analysis with the possibility of hand extension to plasma diagnostics with different generation principles. The second feature of the analysis is that the constrained regularization algorithm, a type of (pixel-based) reconstruction, is extended as a wavelength function for spectral. Furthermore, we will propose a method of wavelength interpolation and extraction of emission lines for processing experimental data in spectral tomography measurements using a multichannel spectrometer.

4.2 Experiments

4.2.1 Optical emission spectroscopic measurement of plasma

Figure 4.1 shows the experimental inductively coupled plasma (ICP)–generating apparatus employed in this study. The inner wall of the chamber was anodized aluminum (pressurized steam sealing, VACAL-SAL2V3010A, ULVAC TECHNO, Ltd.). A spiral-shaped radio frequency (RF) antenna was placed at the top of the chamber over the top window (synthetic quartz, diameter: 205 mm, thickness: 21.5 mm). The side-view window (synthetic quartz, height 115 mm $\times$ width 10 mm, thickness 6 mm) was placed on the chamber sidewall. Argon (Ar) gas was supplied to the chamber via a mass flow controller. The chamber was evacuated using turbomolecular and rotary pumps. The base pressure of the vacuum chamber was

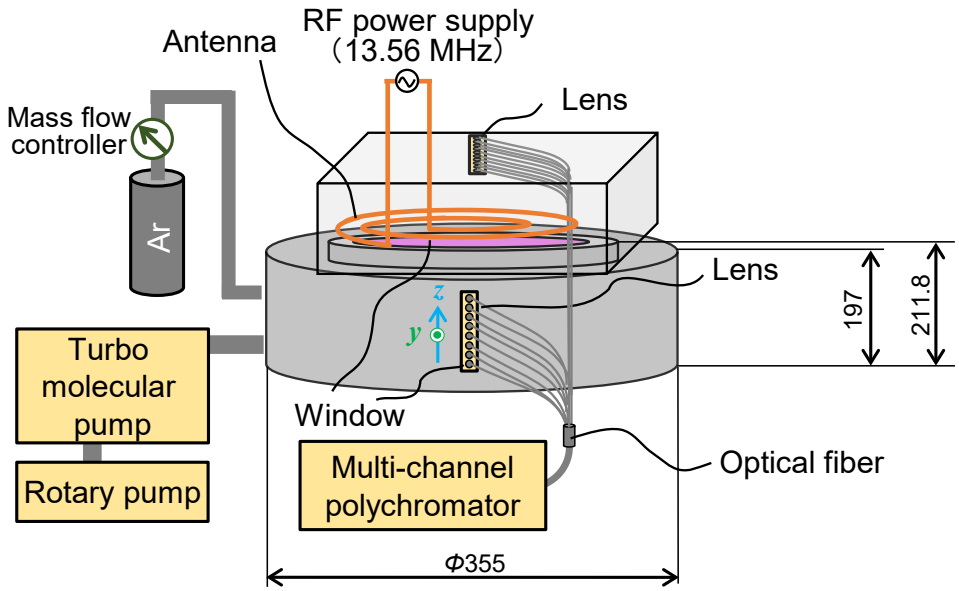

Fig. 4.1: Schematic of ICP-generating apparatus. The sizes are denoted at the chamber internal. Reproduced from Yuya Yamashita *et al.*, J. Vac. Sci. Technol. A, **42**, 023003, (2024) [5] with permission from the American Vacuum Society (AVS).

1.5×10^{-5} Pa. A 13.56 MHz RF power was applied to the RF antenna to generate the plasma.

Eight and ten collimator lenses (#88-173, Edmond Optics) were placed on the outside window of the side ($+y$ side) and top ($+z$ side) of the chamber, respectively, as shown in Fig. 4.2. The collimator lenses were connected to a multichannel spectrometer (M116, Horiba, focal length: 116 mm) with optical fibers (core diameter: 100 μm). The line-of-sight dependence of spiral radiance at the air-side surface on the window $L_{\text{plasma air}}(\lambda)$ was measured by the multichannel spectrometer as described in Sec.4.2.2.

4.2.2 Spectral radiance calibration and Fresnel reflection correction

The spectral radiometry system was calibrated using a setup as shown in Fig 4.3. A spectral radiance surface [25] was realized using a spectral irradiance standard lamp (JPD100V500WCS, Ushio Lighting) and a standard diffuse reflector (SG 3051, SphereOptics). The spectral irradiance standard lamp was driven at a constant voltage of DC 95.0V (the specified voltage as the standard lamp) by a DC power supply unit (PSW-720M160, TEXIO TECHNOLOGY CORPORATION). The voltage was measured using the four-terminal method to prevent measurement errors due to voltage drop in electric wires. The light shields with hole [25] were placed between the spectral irradiance standard lamp and the standard diffuse reflector. The hole size of the light shields is larger than the line connecting the outline of the bulb of the spectral irradiance standard lamp and the outline of the standard diffuse reflector. Therefore, direct light is

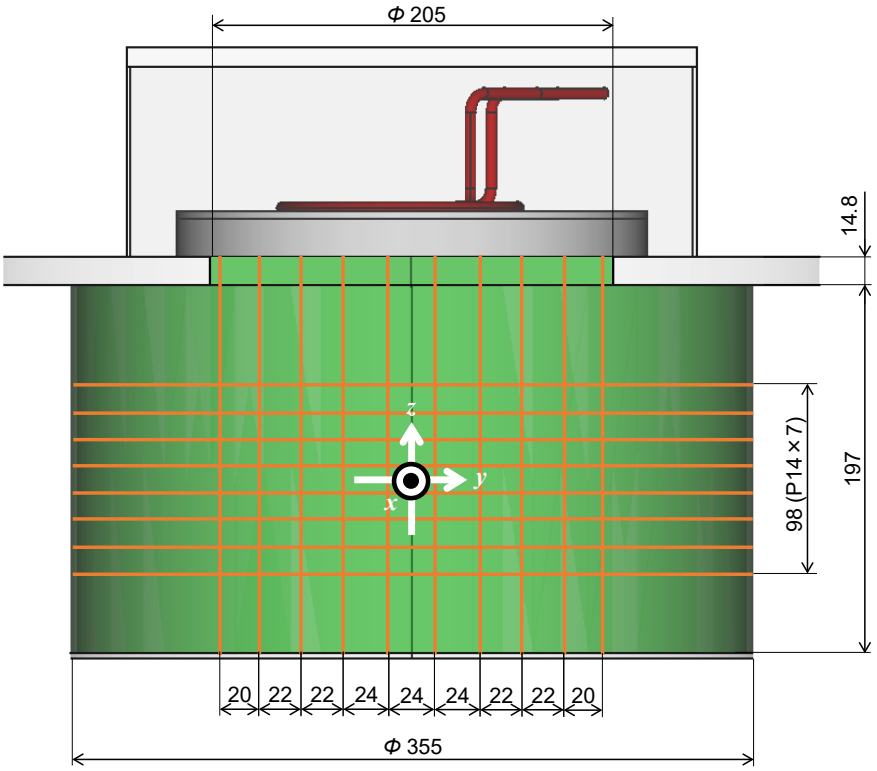

Fig. 4.2: Lines-of-sight of the spectral radiance measurements on the chamber windows. Reproduced from Yuya Yamashita *et al.*, J. Vac. Sci. Technol. A, **42**, 023003, (2024) [5] with permission from the American Vacuum Society (AVS).

not blocked, while stray light is blocked.

The spectral radiance on the standard diffuse reflector surface $L_{\mathrm{std}}(\lambda)$ was obtained as shown in Fig. 4.4 and as follows:

$$L_{\mathrm{std}}(\lambda) = \frac{R_{\mathrm{std}}(\lambda)}{\pi} E_{\mathrm{std}}(\lambda), \tag{4.1}$$

where $R_{\mathrm{std}}(\lambda)$ is the calibration value of the spectral total reflectance of the standard diffuse reflector and $E_{\mathrm{std}}(\lambda)$ is the calibration value of the spectral irradiance standard lamp at 500 mm in front. It must be noted that $R_{\mathrm{std}}(\lambda)$ and $E_{\mathrm{std}}(\lambda)$ were discretely calibrated at 1 and 5 nm intervals, respectively. The interpolated values $S_{\mathrm{lagr}}(\lambda)$ at any wavelength λ in the middle were calculated using the Lagrangian interpolation of the calibrated values of two front points: $S_1(\lambda_1)$ and $S_2(\lambda_2)$, and two back points $S_3(\lambda_3)$ and $S_4(\lambda_4)$, which is shown in Eq. (5) of JIS Z 8724:2015 [31] as follows:

$$\begin{aligned} S_{\mathrm{lagr}}(\lambda) = {} & \frac{(\lambda-\lambda_2)(\lambda-\lambda_3)(\lambda-\lambda_4)}{(\lambda_1-\lambda_2)(\lambda_1-\lambda_3)(\lambda_1-\lambda_4)} S_{\mathrm{s}}(\lambda_1) + \frac{(\lambda-\lambda_1)(\lambda-\lambda_3)(\lambda-\lambda_4)}{(\lambda_2-\lambda_1)(\lambda_2-\lambda_3)(\lambda_2-\lambda_4)} S_{\mathrm{s}}(\lambda_2) \\ & + \frac{(\lambda-\lambda_1)(\lambda-\lambda_2)(\lambda-\lambda_4)}{(\lambda_3-\lambda_1)(\lambda_3-\lambda_2)(\lambda_3-\lambda_4)} S_{\mathrm{s}}(\lambda_3) + \frac{(\lambda-\lambda_1)(\lambda-\lambda_2)(\lambda-\lambda_3)}{(\lambda_4-\lambda_1)(\lambda_4-\lambda_2)(\lambda_4-\lambda_3)} S_{\mathrm{s}}(\lambda_4), \end{aligned} \tag{4.2}$$

where $\lambda_1 < \lambda_2 < \lambda < \lambda_3 < \lambda_4$.

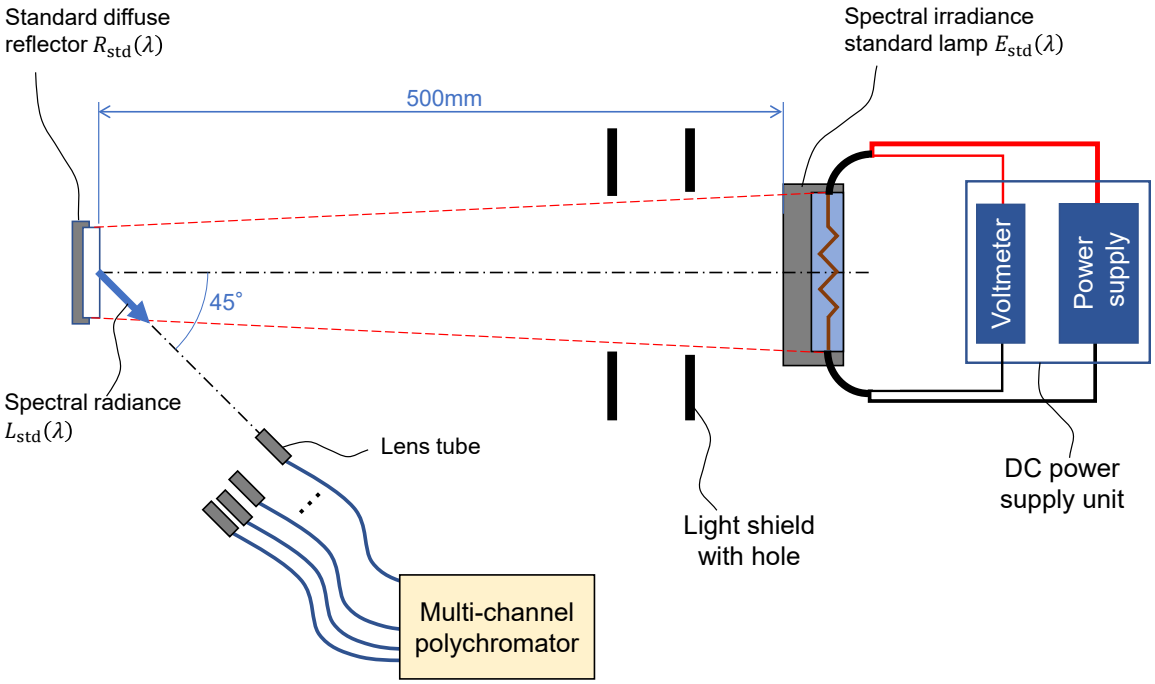

Fig. 4.3: Experiment setup of spectrometer spectral radiance calibration. Reproduced from Yuya Yamashita *et al.*, J. Vac. Sci. Technol. A, **42**, 023003, (2024) [5] with permission from the American Vacuum Society (AVS).

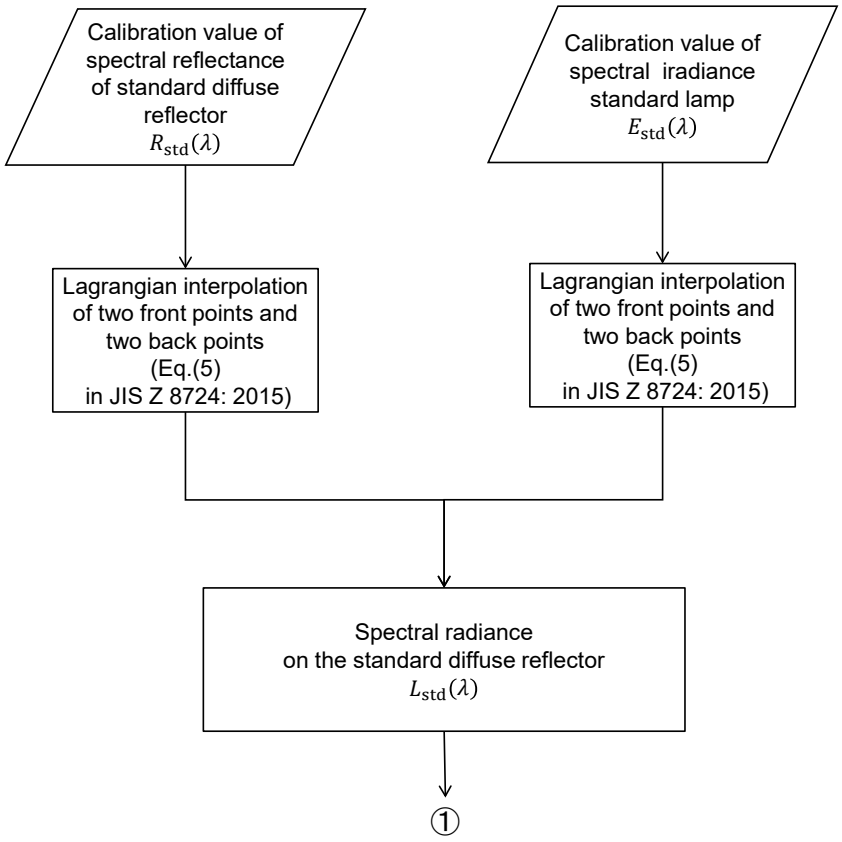

Fig. 4.4: Calculation flowchart of the spectral radiance on the standard diffuse reflector $L_{\mathrm{std}}(\lambda)$. Reproduced from Yuya Yamashita *et al.*, J. Vac. Sci. Technol. A, **42**, 023003, (2024) [5] with permission from the American Vacuum Society (AVS).

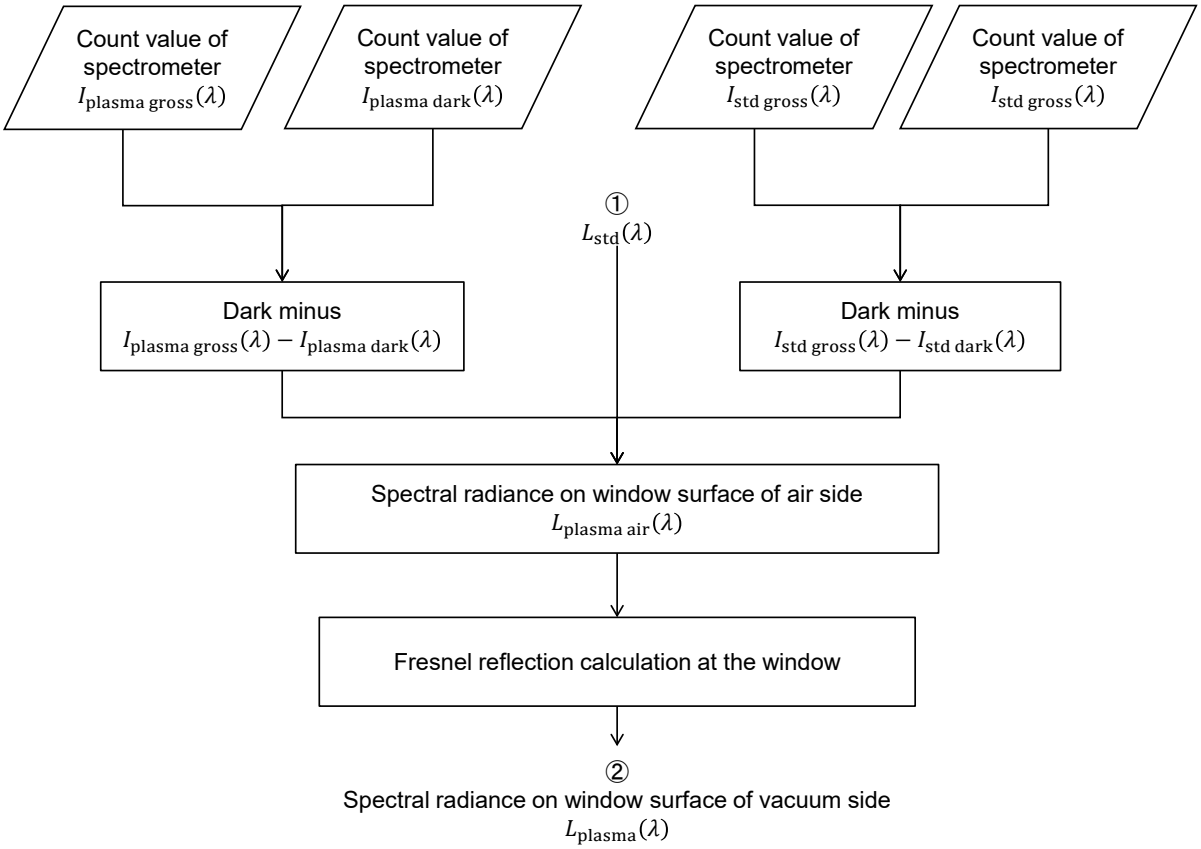

Fig. 4.5: Calculation flowchart of the spectral radiance of plasma. Reproduced from Yuya Yamashita *et al.*, J. Vac. Sci. Technol. A, **42**, 023003, (2024) [5] with permission from the American Vacuum Society (AVS).

The count value when observing the spectral radiance standard plane: $I_{\text{std gross}}(\lambda)$ was measured by the experimental setup as shown in Fig 4.3 for each channel (per fiber with lens). Furthermore, the dark count value: $I_{\text{std dark}}(\lambda)$ was measured by the same system in turning off the spectral irradiance standard lamp.

Therefore, the net value of the spectral radiance of the plasma at the air-side of the window surface: $L_{\text{plsma air}}(\lambda)$ was calculated for each channel as shown in Fig 4.5 and as expressed in the following equation:

$$L_{\text{plsma air}}(\lambda) = L_{\text{std}}(\lambda)\frac{I_{\text{plasma gross}}(\lambda) - I_{\text{plasma dark}}(\lambda)}{I_{\text{std gross}}(\lambda) - I_{\text{std dark}}(\lambda)}, \tag{4.3}$$

where $I_{\text{plasma gross}}(\lambda)$ and $I_{\text{plasma dark}}(\lambda)$ are the count values during the plasma discharge and when the plasma was switched off, respectively; the numerator and denominator denote the net count values of plasma and spectral radiance standard surface measurements, respectively.

Fresnel reflections occur at the window-air and window-vacuum interfaces. Therefore, the

spectral radiance at the vacuum-side surface of the window $L_{\text{plasma}}(\lambda)$[1] was calculated from $L_{\text{plasma air}}(\lambda)$ using the correction formula [4] of the function of the window thickness and the refractive index of the window as shown in Fig. 4.5.

4.3 Spectroscopic tomography calculation

This section outlines the principles of spectral tomography calculations using the constrained regularization algorithm and then describes the data processing scheme of the spectral tomography calculation implemented in this study.

4.3.1 Constrained regularization algorithm

The constrained regularization algorithm [73, 84] is a type of algorithm for algebraic (pixel-based) reconstruction in tomographic calculations. In this study, we developed a spectral tomography program by extending to wavelength function based on Ferreira *et al.*'s constrained regularization source code [85, 86].

$L_i(\lambda)$ is the measured projection [in this study, it corresponds to $L_{\text{plasma}}(\lambda)$] of the ith lens ($i = 1, 2, \cdots, n_{\text{v}} + n_{\text{h}}$, where $n_{\text{v}} = 8$ and $n_{\text{h}} = 10$ are the number of line-of-sight of vertical and horizontal directions, respectively.). n_{cols}(for column) $\times$ n_{rows}(for row) pixels reconstruction plane is considered, which were assumed 57×39 in this study. Note that the actual dimensions per pixel of the reconstructed image plane for y and z directions: Δy and Δz are derived from the above definition as follows, respectively:

$$\Delta y = \frac{y_{\text{max}} - y_{\text{min}}}{n_{\text{cols}}}, \tag{4.4}$$

$$\Delta z = \frac{z_{\text{max}} - z_{\text{min}}}{n_{\text{rows}}}, \tag{4.5}$$

where y_{max} and y_{min} are the y coordinates of the maximum and minimum values in the pixel plane, respectively; z_{max} and z_{min} are the z coordinates of the maximum and minimum values in the pixel plane, respectively. In this study, y_{max}, y_{min}, z_{max}, and z_{min} were assumed $+19.0$, -19.0, $+13.0$, and -13.0 cm, receptively. Therefore, Δy and Δz were also 0.6667 cm/pixel.

$\varepsilon_j(\lambda)$ is the reconstructed image (corresponding to the spectral emission coefficient) of the

[1] [This footnote has been supplemented in this thesis to deepen the reader's understanding and was not included in the original paper [5].] For specific examples of the data of $L_{\text{plasma}}(\lambda)$, see Fig. B.1 in Appendix B.

jth pixel ($j = 1, 2, \cdots, n_{\mathrm{rows}} \times n_{\mathrm{cols}}$)

$$\begin{bmatrix} L_1(\lambda) \\ L_2(\lambda) \\ \vdots \\ L_{n_{\mathrm{v}}+n_{\mathrm{h}}}(\lambda) \end{bmatrix} = \begin{bmatrix} P_{1,1} & P_{1,2} & \cdots & P_{1,(n_{\mathrm{col}} \times n_{\mathrm{row}})} \\ P_{2,1} & P_{2,2} & \cdots & P_{2,(n_{\mathrm{col}} \times n_{\mathrm{row}})} \\ \vdots & \vdots & \ddots & \vdots \\ P_{(n_{\mathrm{v}}+n_{\mathrm{h}}),1} & P_{(n_{\mathrm{v}}+n_{\mathrm{h}}),2} & \cdots & P_{(n_{\mathrm{v}}+n_{\mathrm{h}}),(n_{\mathrm{col}} \times n_{\mathrm{row}})} \end{bmatrix} \begin{bmatrix} \varepsilon_1(\lambda) \\ \varepsilon_2(\lambda) \\ \vdots \\ \varepsilon_{(n_{\mathrm{col}} \times n_{\mathrm{row}})}(\lambda) \end{bmatrix}, \quad (4.6)$$

where $P_{i,j}$ is the projection (in this study, $P_{i,j}$ corresponds to the length of the ith line-of-sight on the jth pixel). We designated the projection vector, projection matrix, and image vector as $\mathbf{L}$, $\mathbf{P}$, and $\boldsymbol{\varepsilon}$, respectively. Equation (4.6) can be written as follows:

$$\mathbf{L} = \mathbf{P}\boldsymbol{\varepsilon}. \quad (4.7)$$

In an ideal situation, where the image is completely reconstructed, the left and right sides of Eqs.(4.6) and (4.7) are equal. However, the left and right sides did not match perfectly owing to numerical calculation errors. To find $\boldsymbol{\varepsilon}$ from $\mathbf{L}$, we must find the inverse of $\mathbf{P}$; however, because $\mathbf{P}$ is irregular, we cannot define the inverse of $\mathbf{P}$. Therefore, $\boldsymbol{\varepsilon}$ cannot be obtained analytically. Thus, the main objective of this reconstruction algorithm is to numerically find $\boldsymbol{\varepsilon}$, which minimizes the residual difference ϕ between $\mathbf{L}$ and $\mathbf{P}\varepsilon$.

$$\phi = \|\mathbf{L} - \mathbf{P}\boldsymbol{\varepsilon}\|^2 + \alpha_1 \|\mathbf{D}_{\mathrm{h}}\boldsymbol{\varepsilon}\|^2 + \alpha_2 \|\mathbf{D}_{\mathrm{v}}\boldsymbol{\varepsilon}\|^2 + \alpha_3 \|\mathbf{I}_{\mathrm{o}}\boldsymbol{\varepsilon}\|^2, \quad (4.8)$$

where $\alpha_1 (> 0)$ is the regularization parameter that determines the calculation errors of $\mathbf{L}$ and $\mathbf{P}\boldsymbol{\varepsilon}$, α_1 was given as 1×10^{-5}; α_2 and α_3 are defined as follows:

$$\alpha_2 = \alpha_1, \quad (4.9)$$

$$\alpha_3 = 10\,\alpha_2. \quad (4.10)$$

$\mathbf{D}_{\mathrm{h}}$, $\mathbf{D}_{\mathrm{v}}$, and $\mathbf{I}_{\mathrm{o}}$ are regularization matrices,

$$\mathbf{D}_{\mathrm{h}} = \mathbf{E} - \mathbf{A}, \quad (4.11)$$

where $\mathbf{E}$ is an $n_{\mathrm{rows}}n_{\mathrm{cols}}$-dimensional identity matrix and $\mathbf{A} = [a_{i,j}]$ as follows:

$$a_{i,j} = \begin{cases} 1 & [j = i+1 \ (\text{for } i = 1, 2, \ldots, (n_{\mathrm{rows}}n_{\mathrm{cols}} - 1))] \\ 1 & (i = n_{\mathrm{rows}}n_{\mathrm{cols}},\ j = 1) \\ 0 & (\text{else}), \end{cases} \quad (4.12)$$

$$\mathbf{D}_{\mathrm{v}} = \mathbf{E} - \mathbf{B}, \quad (4.13)$$

where $\mathbf{B}=[b_{i,j}]$ as follows:

$$b_{i,j}=\begin{cases}1 & [j=i+n_{\mathrm{cols}}\ (\text{for } i=1,2,\ldots,(n_{\mathrm{rows}}n_{\mathrm{cols}}-n_{\mathrm{cols}}))]\\ 1 & [j=1,2,\ldots,n_{\mathrm{cols}},\ (\text{for } i=(n_{\mathrm{rows}}n_{\mathrm{cols}}-n_{\mathrm{cols}}+1),\ldots,n_{\mathrm{rows}}n_{\mathrm{cols}})]\\ 0 & (\text{else})\end{cases} \tag{4.14}$$

and $\mathbf{I}_{\mathrm{o}}$ is a mask matrix, and the elements inside the ellipse (half axes are $(n_{\mathrm{rows}},n_{\mathrm{cols}})$ and whose center is $(0,0)$) are 0, and the other elements are 1.

Here, the pseudoinverse matrix M of P is defined as

$$\boldsymbol{\varepsilon}=\mathbf{M}\cdot\mathbf{L}. \tag{4.15}$$

From the above discussion, M can be expressed as

$$\mathbf{M}=\left(\mathbf{P}^{\mathrm{T}}\mathbf{P}+\alpha_1\mathbf{D}_{\mathrm{h}}^{\mathrm{T}}\mathbf{D}_{\mathrm{h}}+\alpha_2\mathbf{D}_{\mathrm{v}}^{\mathrm{T}}\mathbf{D}_{\mathrm{v}}+\alpha_3\mathbf{I}_{\mathrm{o}}^{\mathrm{T}}\mathbf{I}_{\mathrm{o}}\right)^{-1}\mathbf{P}^{\mathrm{T}}. \tag{4.16}$$

Therefore, the reconstructed image $\boldsymbol{\varepsilon}$, which corresponds to the dependence of the spectral emission coefficient on the position $\varepsilon_j(\lambda)$, can be obtained.

4.3.2 Spectral tomography calculation

This section describes the data processing algorithm to spectral tomography on tomography calculation. The algorithm was developed in this study. Figure 4.6 shows the flow of data processing for spectral tomography calculation. Generally, in multichannel spectrometers, even if the pixels belong to the same row in the pixel plane of the image-receiving surface, the corresponding wavelengths are different for each row. However, to perform spectral tomography calculations, the dependence of spectral emissions between channels on the same wavelength has to be obtained. Therefore, in this study, linear interpolation of one front point and one back point was used to obtain the spectral radiance at any wavelength from the experimental spectral radiance data. The linear interpolated value $S_{\mathrm{linear}}(\lambda)$ at λ was obtained with the experimental data points of the front $S_1(\lambda_1)$ and the back $S_2(\lambda_2)$ as follows:

$$S_{\mathrm{linear}}(\lambda)=\frac{\lambda-\lambda_2}{\lambda_1-\lambda_2}S_1(\lambda_1)+\frac{\lambda-\lambda_1}{\lambda_2-\lambda_1}S_2(\lambda_2), \tag{4.17}$$

where $\lambda_1<\lambda<\lambda_2$. The reasons for adopting this interpolation method are as follows: The mean slit wavelength width (wavelength resolution, determined by pixel width) of the spectrometer employed in this study is 2.19 nm. The mean measurement wavelength interval (determined by pixel interval) of the spectrometer employed in this study is 0.38 nm. Since the natural width of the argon spectrum is sufficiently narrow, linear interpolation at one point,

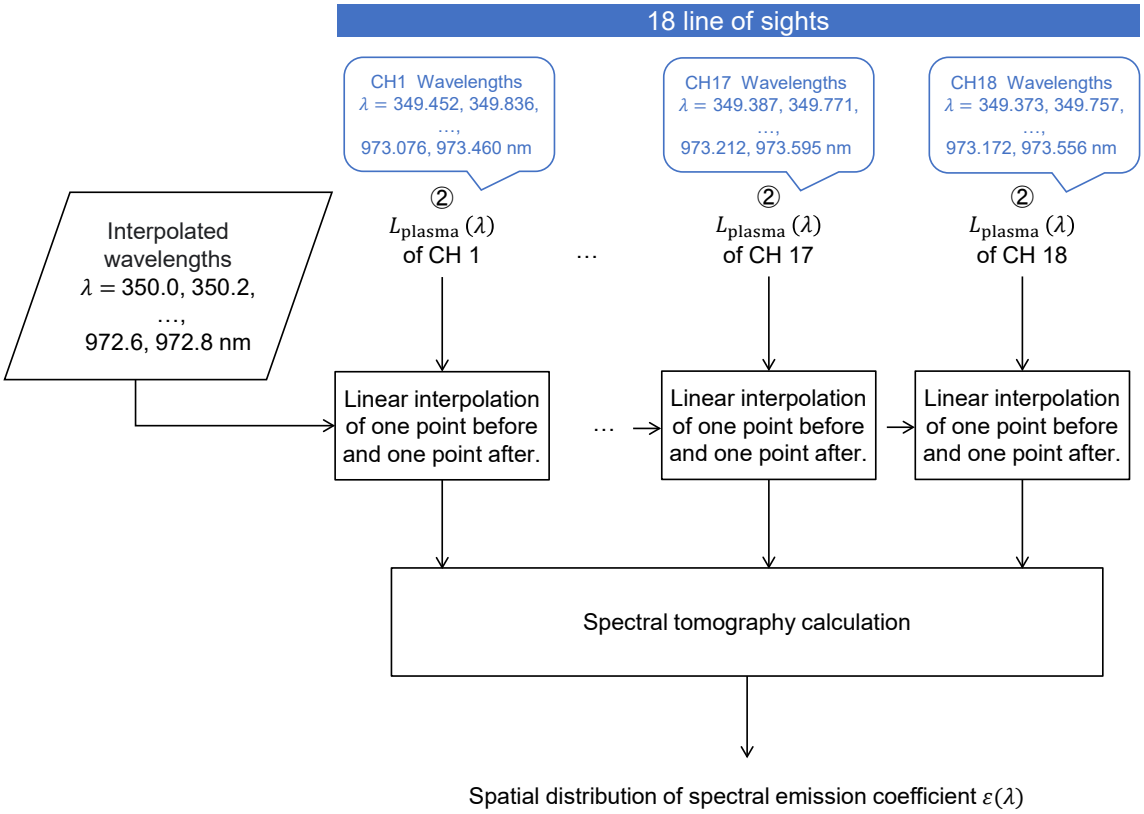

Fig. 4.6: Calculation flowchart of the spectral tomography. Reproduced from Yuya Yamashita *et al.*, J. Vac. Sci. Technol. A, **42**, 023003, (2024) [5] with permission from the American Vacuum Society (AVS).

before and after, was performed. In this study, the $L_{\mathrm{plasma}}(\lambda)$ of each channel (CH) was interpolated by 0.2 nm at wavelengths of 350.0–972.8 nm. These were substituted into Eq.(4.15), and the spatial distribution of spectral emission coefficients was obtained from $L_{\mathrm{plasma}}(\lambda)$ in the wavelength of 350.0–972.8 nm by spectral tomography calculation.

4.4 Diagnosis

4.4.1 Calculation of reduced population density distribution

This section describes the method for determining the spatial distribution of the number density of excited levels from the spatial distribution of the spectral radiance. Table 4.1 shows the optical emission lines employed in this study.

The relationship between the spectral emission coefficient and the number density of the excited levels is expressed as follows:

$$4\pi \int_{-\infty}^{\infty} \varepsilon_{j^*\to i^*}(\lambda)\,\mathrm{d}\lambda = h\,\frac{c}{\lambda(j^*,i^*)}\,A(j^*,i^*)\,n_{j^*}, \tag{4.18}$$

Table 4.1: Optical emission lines for OES measurement. Reproduced from Yuya Yamashita *et al.*, J. Vac. Sci. Technol. A, **42**, 023003, (2024) [5] with permission from the American Vacuum Society (AVS).

Ritz wavelength	Upper level				Lower level				A coefficient [66]
in Air [66]	Vlček [66]		Racah [66]		Vlček [66]		Racah [66]		$A(j^*,i^*)$
$\lambda(j^*,i^*)$ [nm]	level j	g_j	level j^*	g_{j^*}	level i	g_i	level i^*	g_{i^*}	[s^{-1}]
708.6705	21	24	$6s'[1/2]_1^\circ$	3	10	1	$4p[1/2]_0$	1	1.50×10^5
794.8176	8	8	$4p'[3/2]_1$	3	4	1	$4s'[1/2]_0^\circ$	1	1.86×10^7
826.4521	9	3	$4p'[1/2]_1$	3	5	3	$4s'[1/2]_1^\circ$	3	1.53×10^7
840.8209	8	8	$4p'[3/2]_2$	5	5	3	$4s'[1/2]_1^\circ$	3	2.23×10^7
842.4647	7	20	$4p[5/2]_2$	5	3	3	$4s[3/2]_1^\circ$	3	2.15×10^7
852.1441	8	8	$4p'[3/2]_1$	3	5	3	$4s'[1/2]_1^\circ$	3	1.39×10^7
866.7943	7	20	$4p[3/2]_1$	3	4	1	$4s'[1/2]_0^\circ$	1	2.43×10^6
912.2967	6	3	$4p[1/2]_1$	3	2	5	$4s[3/2]_2^\circ$	5	1.89×10^7
922.4498	7	20	$4p[3/2]_2$	5	5	3	$4s'[1/2]_1^\circ$	3	5.00×10^6
935.4218	7	20	$4p[3/2]_1$	3	5	3	$4s'[1/2]_1^\circ$	3	1.06×10^6
965.7786	6	3	$4p[1/2]_1$	3	3	3	$4s[3/2]_1^\circ$	3	5.40×10^6

where $\varepsilon_{j^*\to i^*}$ is the spectral emission coefficient of the transition from level j^* to level i^*, that is, the line spectral profile of the transition from level j^* to level i^*; h is the Planck constant, c is the speed of light, $\lambda(j^*,i^*)$ is the wavelength of the transition from level j^* to level i^*, $A(j^*,i^*)$ is Einstein's A coefficient of the transition from level j^* to level i^*, and n_{j^*} is the number density of level j^*.

When observing the line spectra nearby using a spectrometer with a large wavelength resolution, the hems of the line spectra overlap. Therefore, if the experimental data for spectral emission coefficients are integrated over the wavelength range, the emission coefficients for a given emission line cannot be determined correctly. To solve this problem, we separated adjacent line spectra by fitting the calculated value obtained using the Voigt function to the experimental data of the spectral emission coefficients. Then, the emission coefficients were obtained by integrating the line spectrum profiles (spectral emission coefficients) obtained using the Voigt function in the wavelength direction for each transition alone.

Prior studies with Abel transformations used the same transitions for all positions to diagnose. On the other hand in this study, in each pixel, emission lines were mechanically extracted from the experimentally obtained spectral emission coefficient data, and the extracted emission lines were used to obtain the excited-level number density distribution. Because the wavelength distribution and strength of the spectral emission coefficients differ greatly depending on the spatial location, there were no transitions that appeared in common for all pixels.

4.4.2 Argon CR model and diagnostics with the model

The Ar CR model [50] is an excitation kinetic model that provides a reduced population density distribution n_i/g_i with T_e, electron energy distribution function (EEDF), N_e, atomic temperature T_a, ion density N_I, and plasma radius r as input parameters. The rate equation is as follows:

$$\begin{aligned}\frac{dn_i}{dt} = &\sum_{j=i+1}^{65}\left[-\{C(i,j)N_e n_i + K(i,j)n_1 n_i\} + \left\{F(j,i)N_e n_j + L(j,i)n_1 n_j + A(j,i)\Lambda_{j,i}n_j\right\}\right] \\ &+ \sum_{j=1}^{i-1}\left[\left\{C(j,i)N_e n_j + K(j,i)n_1 n_j\right\} - \left\{F(i,j)N_e n_j + L(i,j)n_1 n_i + A(i,j)\Lambda_{i,j}n_i\right\}\right] \\ &- \{S(i)N_e n_i + V(i)n_1 n_i\} + [\{O(i)N_e + W(i)n_1 + R(i)\Lambda_i\}]N_e N_I - [D(i) + B(i)] \\ &(i = 2,3,\cdots),\end{aligned} \tag{4.19}$$

where C and F are the electron-collisional excitation and de-excitation rate coefficients, respectively; K and L are the atomic-collisional excitation and de-excitation rate coefficients, respectively; A is the radiative transition probability; S and O are the atomic-collisional ionization and electron three-body recombination rate coefficients, respectively; V and W are the atomic-collisional ionization and atomic three-body recombination rate coefficients, respectively; R is the radiative recombination rate coefficient; B is the rate of generation of metastable Ar_2 molecules, D is the diffusion loss of the metastable Ar atom; $\Lambda_{i,j}$ and Λ_i are the optical escape factors of the transition from level i to level j and the transition from ion level to level i, respectively. The rate coefficients were calculated based on reaction cross sections, which were function of T_e, N_e, p, r, T_a, or N_I, as shown in the study by Vlcek [50]. The quasi-stationary approximation ($d/dt = 0$) in Eq.(4.19) yields a set of simultaneous equations with T_e and N_e as input variables and n_i as the output variable. $\Lambda_{i,j}$ and Λ_i were calculated as shown in the study by Vlcek [50]. Optical thickness for transitions to the ground level $\Lambda_{i,1}$ was considered and to non-ground levels were assumed to be optically thin [$\Lambda_{i,j} = 1$ (for $j \neq 1$)].

In this study, T_e and N_e were determined by fitting the n_i/g_i distributions of the experimental values by OES measurements and the values calculated from the Ar CR model. The objective function f_I for the fitting [4, 51, 52] was assumed as follows:

$$f_I(T_e, N_e) = \sum_{i \in I}\left(\frac{n_{i\mathrm{model}}(T_e, N_e)/g_i}{n_{i\mathrm{OES}}/g_i} - 1\right)^2, \tag{4.20}$$

where $n_{i\mathrm{model}}(T_e, N_e)/g_i$ is the value of n_i/g_i from the Ar CR model and $n_{i\mathrm{OES}}/g_i$ is the experimental value obtained from OES measurements; I is a set of optical emission lines which are

employed for the fitting. In this study, nine, ten, or 11 optical emission lines shown in Table 4.1 for diagnosis were employed. T_e and N_e were obtained by fitting the minimization f_1.

4.5 Results and discussion

4.5.1 Spectral tomography

Figures 4.7 – 4.14 show the dependence of the spectral emission coefficient on the spatial position, pressure, and power. The spectral emission coefficient increased with increasing pressure and power. The spectral emission coefficient was generally higher in the center and lower in the periphery in the y-direction. For the z-direction, it was higher on the upper side, just below the antenna and window, and decreased downstream. The spatial distribution of spectral emission coefficient was different for each wavelength even at the same pressure and power. It denotes that each excited level had a different dependence on the spatial distribution.

In the central region where the lines-of-sight intersect, the spatial distribution could be observed at a high resolution; however, the resolution of the reconstructed images was inferior in the peripheral areas where the lines-of-sight did not intersect. In the peripheral area, there were areas that the spectral emission coefficients as a reconstructed value were negative values. In this experiment, the line-of-sight placement was concentrated in the center of the chamber, and thus, the spatial distribution of spectral emission coefficients at the periphery could not be adequately obtained. Therefore, uncertainty in image reconstruction may have been greater at the same area. In this study, subsequent analyses for diagnostics of T_e and N_e are discussed focusing only on the central region ($-10 \leq y\,[\mathrm{cm}] \leq 10, -4 \leq z\,[\mathrm{cm}] \leq 4$).

4.5.2 Diagnosis of electron temperature and density

Figures 4.15 shows the T_e diagnostic result as a dependence on pressure and spatial position. T_e decreased with increasing pressure. A possible mechanism behind this observation is that the increase in pressure increased the electron-atom collision frequency and reduced the high-energy component of the electrons.

Figure 4.16 shows the T_e diagnostic result as a dependence on power and spatial position. T_e increased monotonically with power from 200 W to 400 W. It decreased once, from 400 W to 600 W, and increased again from 600 W to 800 W. The mechanism for the roughly monotonic increase in power and T_e is thought to be the increase in electromagnetic field strength that accompanied by the increase in power, which contributed to the acceleration of electrons. The

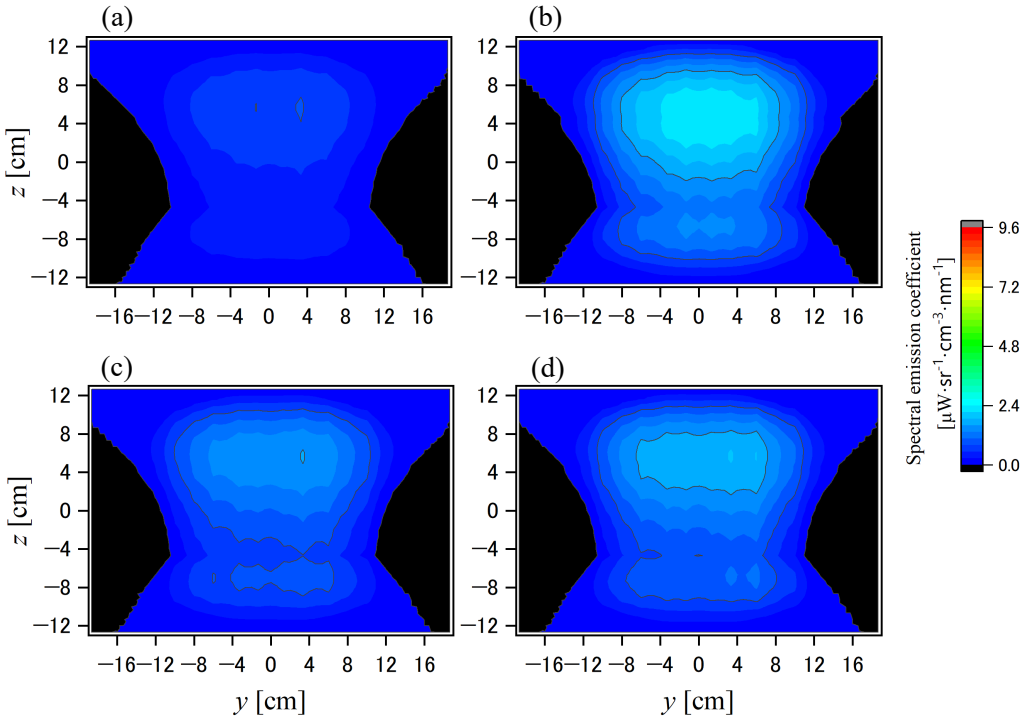

Fig. 4.7: Dependence of 708.6 nm of the spectral emission coefficient on the position and power at p = 1 Pa. (a), (b), (c), and (d) are the results at P = 200, 400, 600, and 800 W, respectively. Reproduced from Yuya Yamashita *et al.*, J. Vac. Sci. Technol. A, **42**, 023003, (2024) [5] with permission from the American Vacuum Society (AVS).

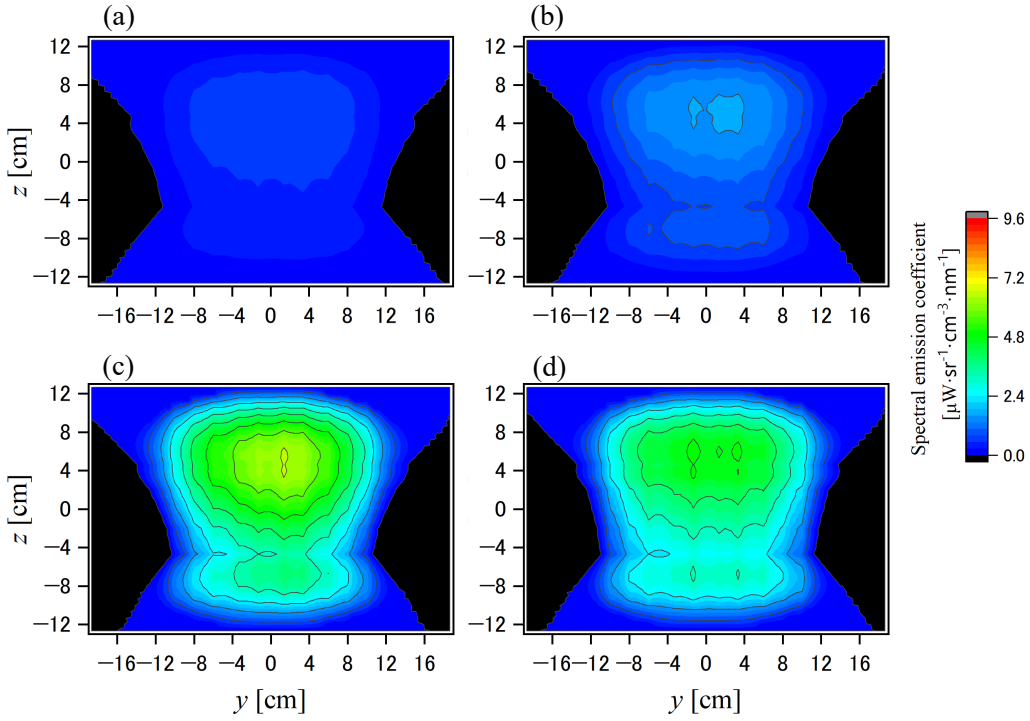

Fig. 4.8: Dependence of 708.6 nm of the spectral emission coefficient on the position and pressure at P = 300 W. (a), (b), (c), and (d) are the results at p = 0.5, 1, 5, and 10 Pa, respectively. Reproduced from Yuya Yamashita *et al.*, J. Vac. Sci. Technol. A, **42**, 023003, (2024) [5] with permission from the American Vacuum Society (AVS).

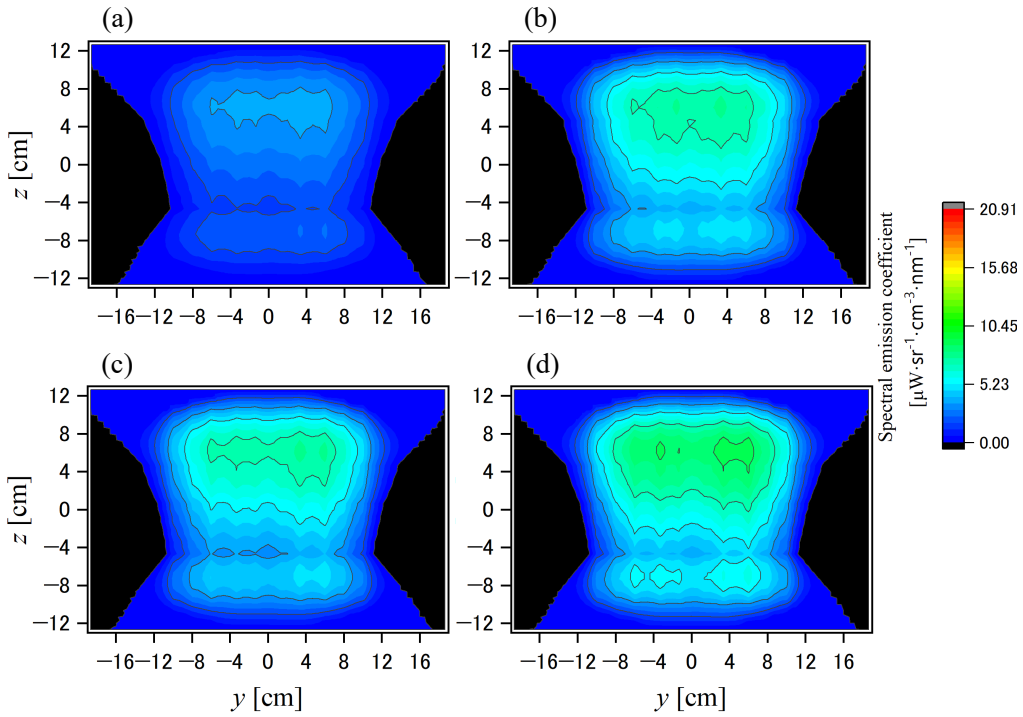

Fig. 4.9: Dependence of 750.4 nm of the spectral emission coefficient on the position and power at p = 1 Pa. (a), (b), (c), and (d) are the results at P = 200, 400, 600, and 800 W, respectively. Reproduced from Yuya Yamashita *et al.*, J. Vac. Sci. Technol. A, **42**, 023003, (2024) [5] with permission from the American Vacuum Society (AVS).

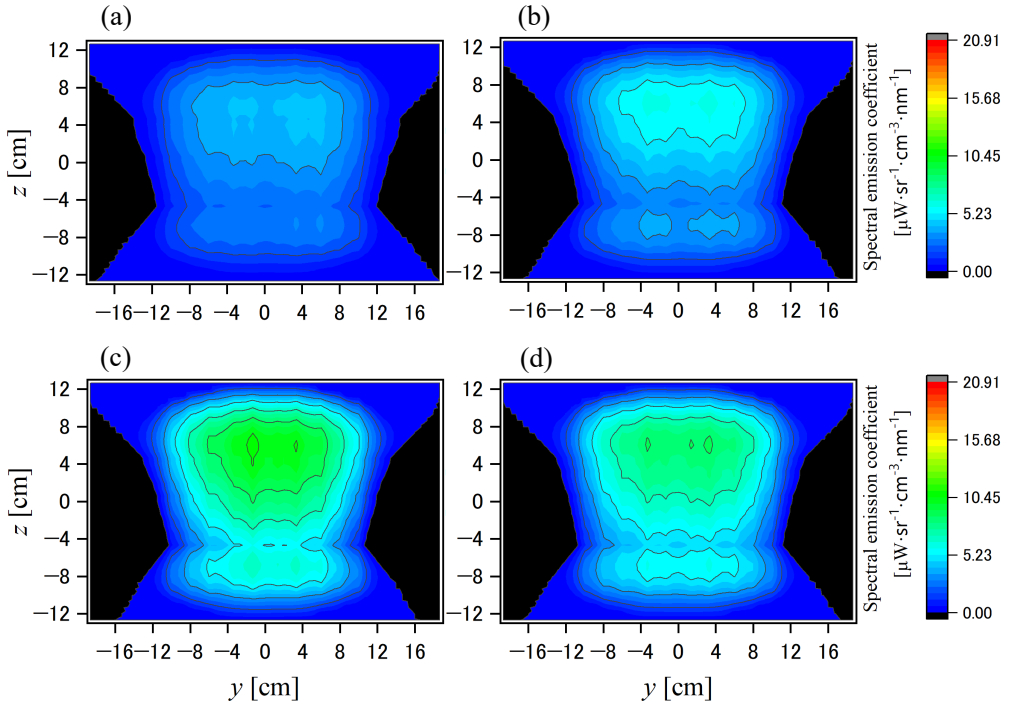

Fig. 4.10: Dependence of 750.4 nm of the spectral emission coefficient on the position and pressure at P = 300 W. (a), (b), (c), and (d) are the results at p = 0.5, 1, 5, and 10 Pa, respectively. Reproduced from Yuya Yamashita *et al.*, J. Vac. Sci. Technol. A, **42**, 023003, (2024) [5] with permission from the American Vacuum Society (AVS).

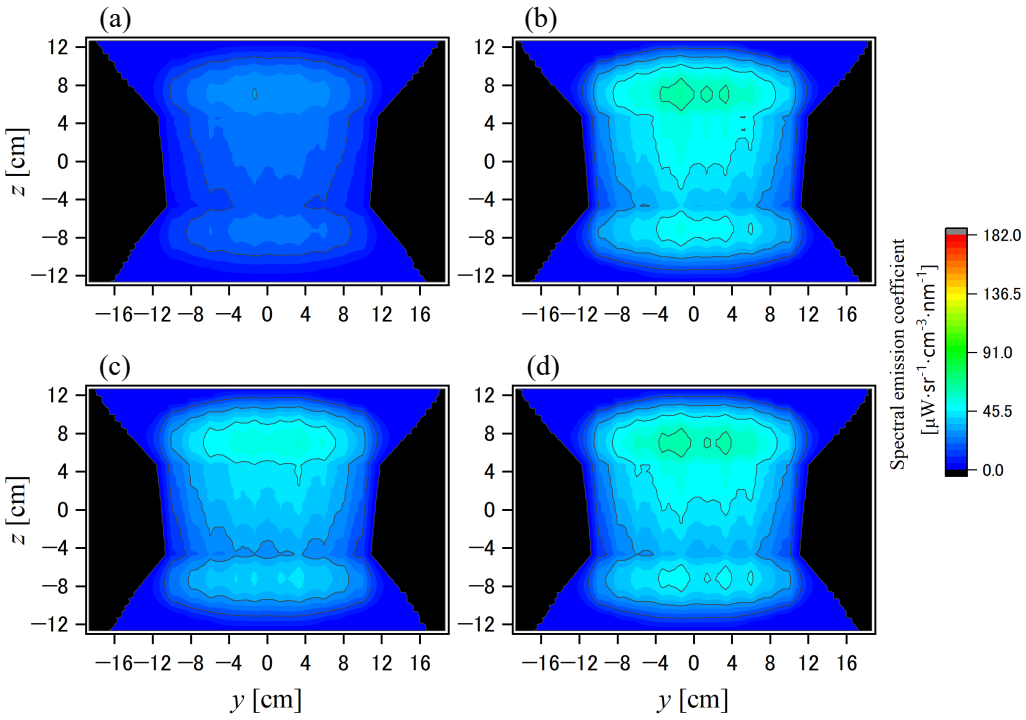

Fig. 4.11: Dependence of 811.8 nm of the spectral emission coefficient on the position and power at p = 1 Pa. (a), (b), (c), and (d) are the results at P = 200, 400, 600, and 800 W, respectively. Reproduced from Yuya Yamashita *et al.*, J. Vac. Sci. Technol. A, **42**, 023003, (2024) [5] with permission from the American Vacuum Society (AVS).

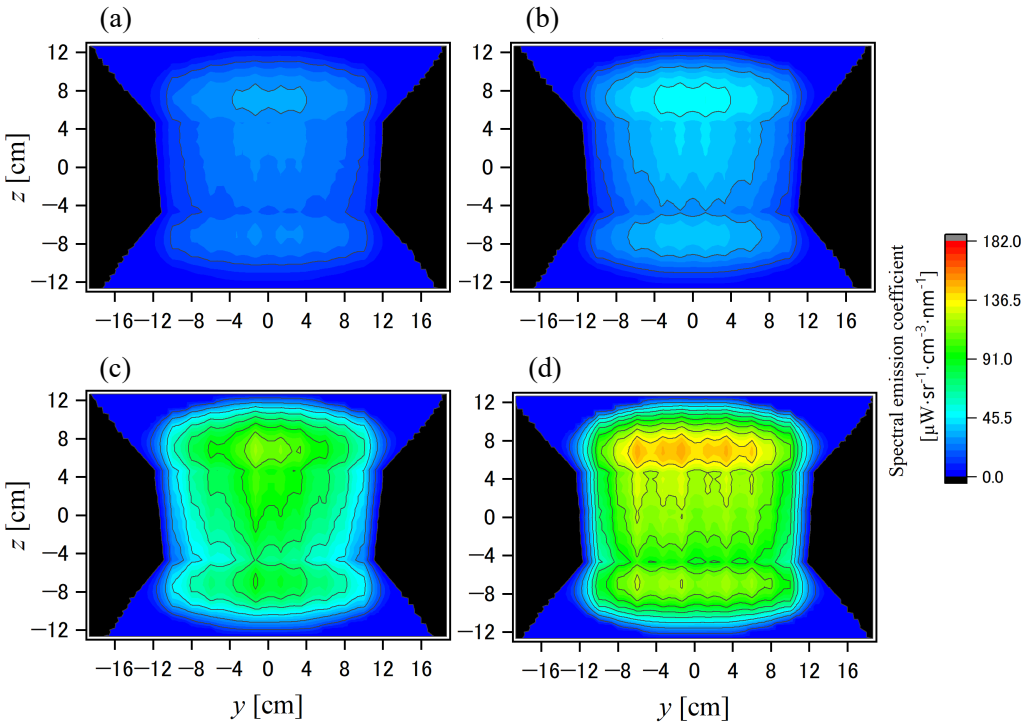

Fig. 4.12: Dependence of 811.8 nm of the spectral emission coefficient on the position and pressure at P = 300 W. (a), (b), (c), and (d) are the results at p = 0.5, 1, 5, and 10 Pa, respectively. Reproduced from Yuya Yamashita *et al.*, J. Vac. Sci. Technol. A, **42**, 023003, (2024) [5] with permission from the American Vacuum Society (AVS).

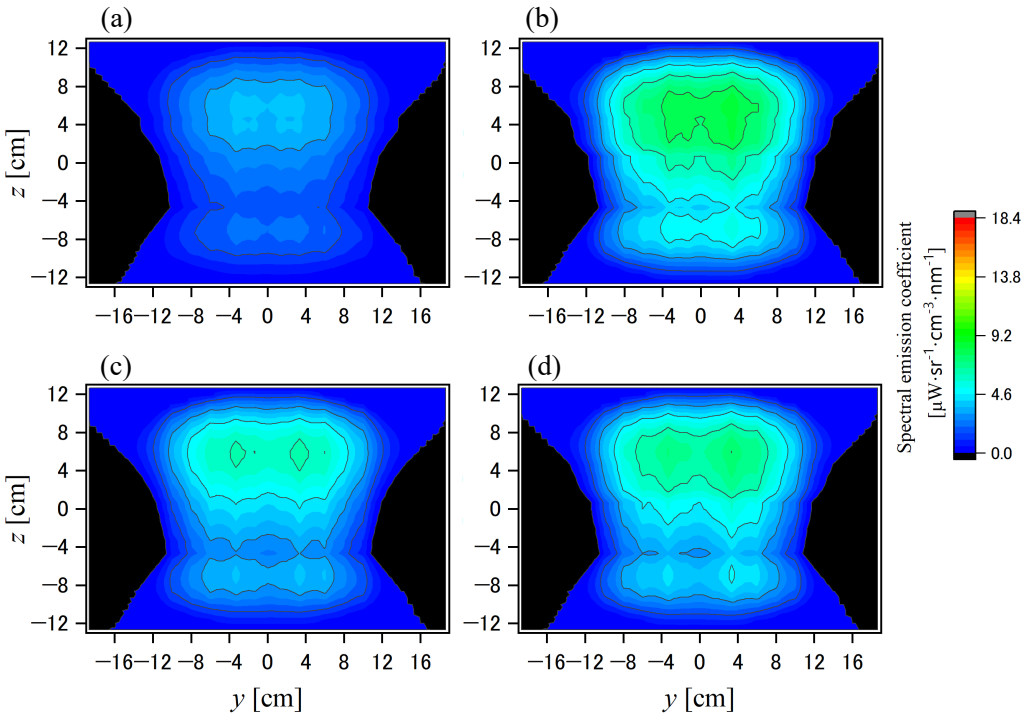

Fig. 4.13: Dependence of 965.8 nm of the spectral emission coefficient on the position and power at p = 1 Pa. (a), (b), (c), and (d) are the results at P = 200, 400, 600, and 800 W, respectively. Reproduced from Yuya Yamashita *et al.*, J. Vac. Sci. Technol. A, **42**, 023003, (2024) [5] with permission from the American Vacuum Society (AVS).

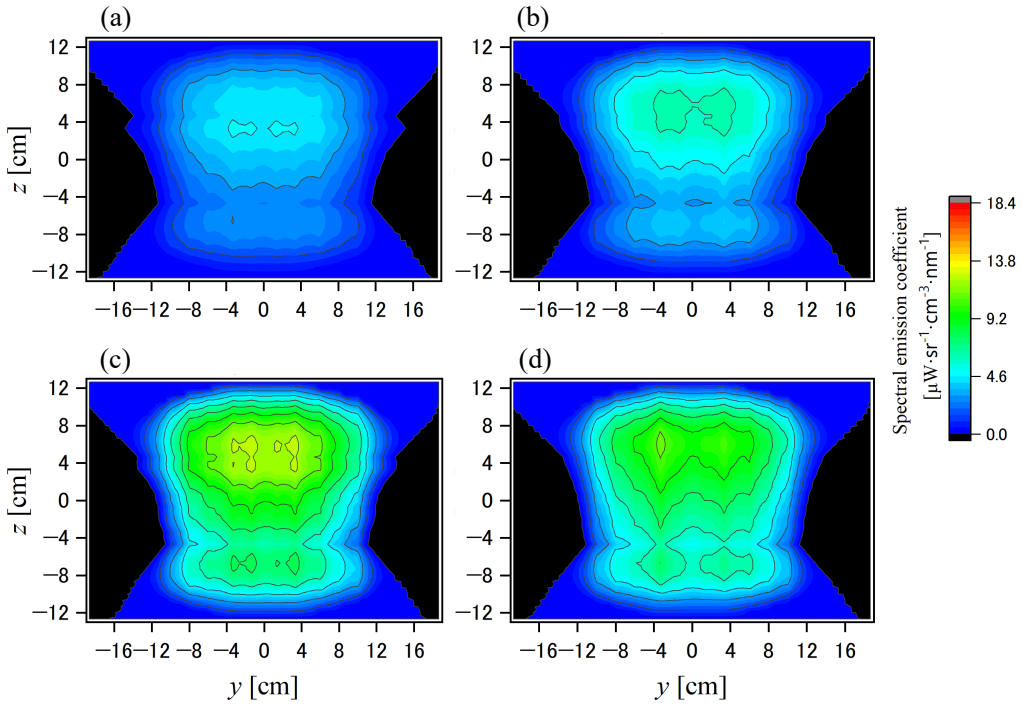

Fig. 4.14: Dependence of 965.8 nm of the spectral emission coefficient on the position and pressure at P = 300 W. (a), (b), (c), and (d) are the results at p = 0.5, 1, 5, and 10 Pa, respectively. Reproduced from Yuya Yamashita *et al.*, J. Vac. Sci. Technol. A, **42**, 023003, (2024) [5] with permission from the American Vacuum Society (AVS).

cause of the decrease in T_e once at 400 W to 600 W may have been a transition from the E-mode (capacitive discharge mode) to the H-mode (inductive discharge mode). The phenomenon that the T_e drops once at the transition from the E-mode to the H-mode even with increasing power is reported in a simulation of an argon ICP plasma at 6.7 Pa by Zhao *et al.* [87].

The y-direction dependence on T_e shows asymmetry higher in the center and lower in the periphery. The z-direction dependence on T_e shows higher in the upper side and lower in the lower side. This is because of the grounded window flange and the nonuniform-induced electromagnetic field distribution on the y-x plane and the asymmetry of the geometrical structure of the device, particularly the spiral antenna ends [4].

Figure 4.17 shows the N_e diagnostic result as the dependence on pressure and spatial position. N_e decreased with increasing pressure. This may be due to the increase in ionization/desorption reactions caused by the increase in electron-atom collision frequency due to increased pressure. Figure 4.18 shows the N_e diagnostic result as a dependence on power and spatial position. N_e were generally constant regardless of the electric power. N_e exhibited a gradual change in the spatial distribution, regardless of the geometric structure of the device. This is attributed to the significant influence of the diffusion effect on the wall and other factors. In addition, the spatial distribution was asymmetrical.

There is a previous literature [4] reporting electromagnetic field simulations for the experimental apparatus used in this study. In that simulation, the electromagnetic field distribution was asymmetric. The asymmetry of the electromagnetic field distribution was considered to be caused by the axially asymmetric shape of the spiral antenna. Note that in this study spontaneous emission transitions between excited levels were assumed to be optically thin. This assumption may be a cause of increased uncertainty of the diagnosis result of T_e and N_e in high-density plasmas.

4.5.3 Discussion of uncertainty of spectral tomography and diagnosis

At the beginning, middle, and end in a series of experimental sequences with varying pressure and power, the spectral radiance was also measured at $p = 10\,\mathrm{Pa}, P = 800\,\mathrm{W}$ three times in total. Figure 4.19 shows the average and range of the emission coefficient as the result of spectral tomography calculation at 708.6 nm on the three times measurements. T_e and N_e were diagnosed from the three times measurements independently, and their average and range were also obtained as shown in Figs. 4.20 and 4.21, respectively.

The range of the emission coefficient was largest in the area around $y = 0\,\mathrm{cm}$, $z = 8\,\mathrm{cm}$. It

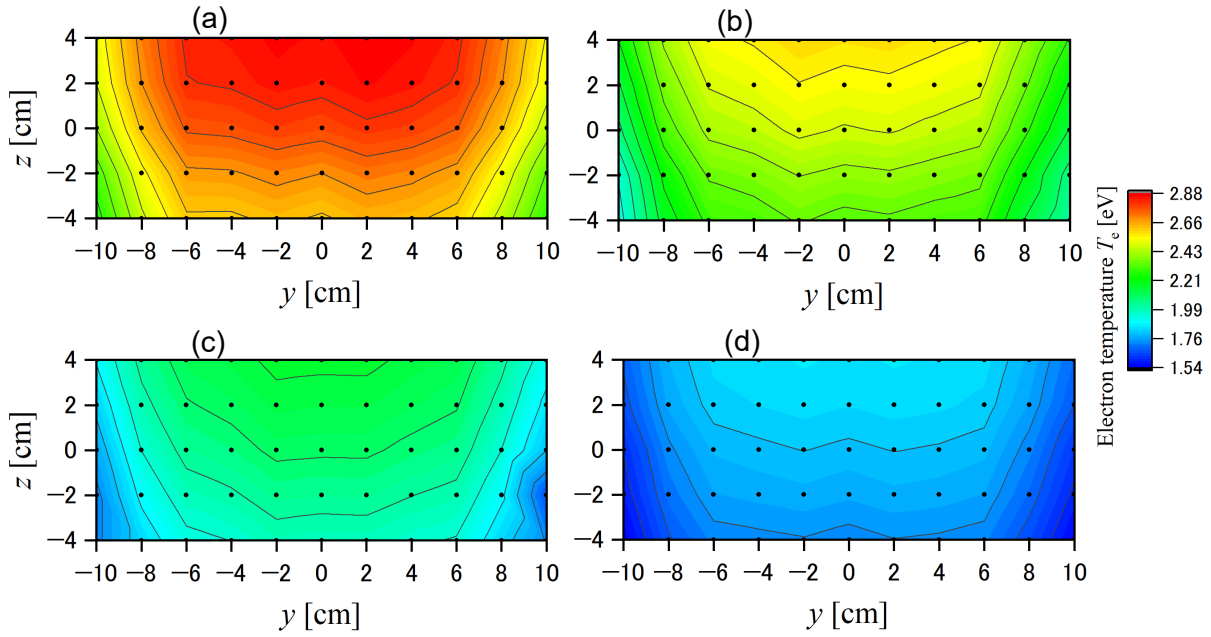

Fig. 4.15: Dependence of electron temperature on spatial position and pressure at P = 300 W. (a), (b), (c), and (d) are the results at $p = 0.5$, 1, 5, and 10 Pa, respectively. Reproduced from Yuya Yamashita *et al.*, J. Vac. Sci. Technol. A, **42**, 023003, (2024) [5] with permission from the American Vacuum Society (AVS).

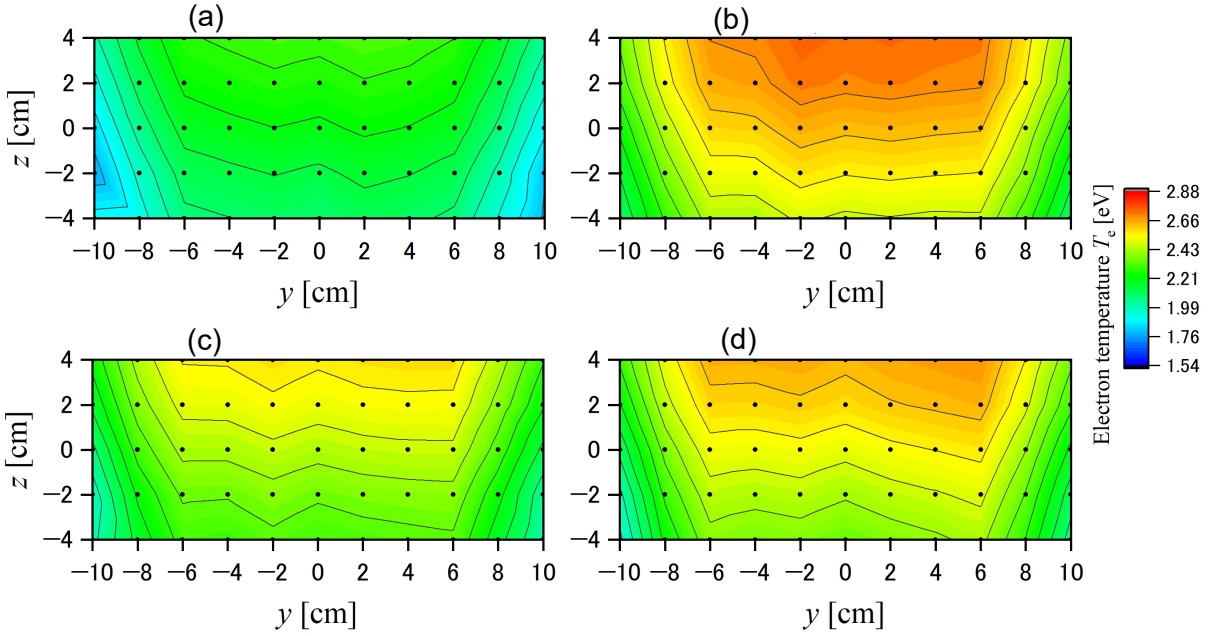

Fig. 4.16: Dependence of electron temperature on spatial position and RF power at p = 1 Pa. (a), (b), (c), and (d) are the results at $P = 200$, 400, 600, and 800 W, respectively. Reproduced from Yuya Yamashita *et al.*, J. Vac. Sci. Technol. A, **42**, 023003, (2024) [5] with permission from the American Vacuum Society (AVS).

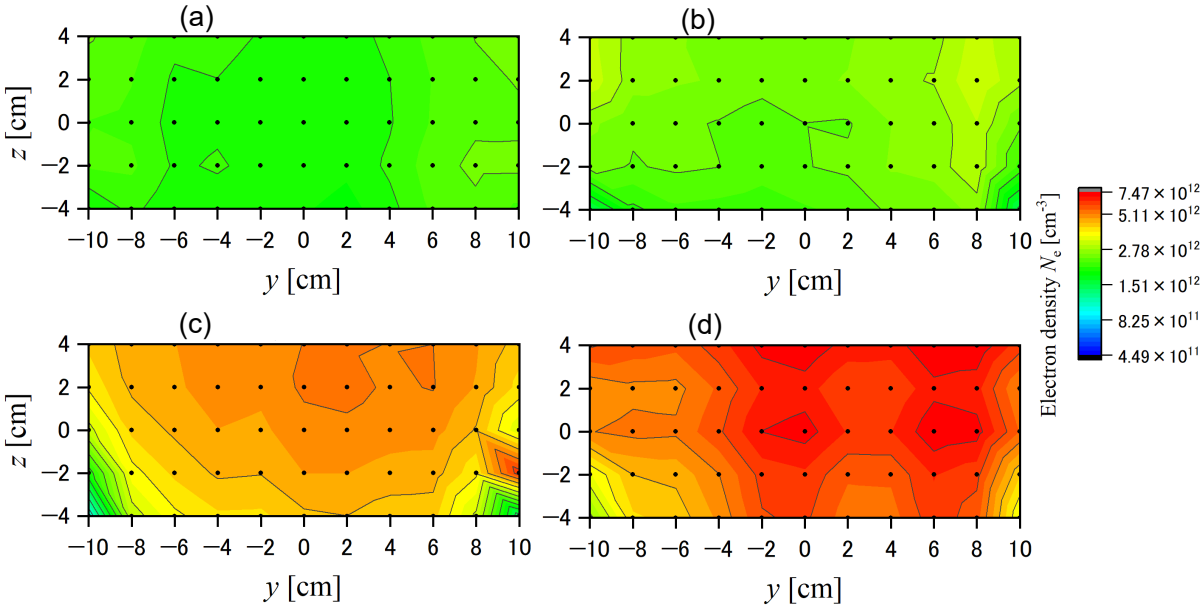

Fig. 4.17: Dependence of electron density on spatial position and pressure at P = 300 W. (a), (b), (c), and (d) are the results at $p = 0.5$, 1, 5, and 10 Pa, respectively. Reproduced from Yuya Yamashita *et al.*, J. Vac. Sci. Technol. A, **42**, 023003, (2024) [5] with permission from the American Vacuum Society (AVS).

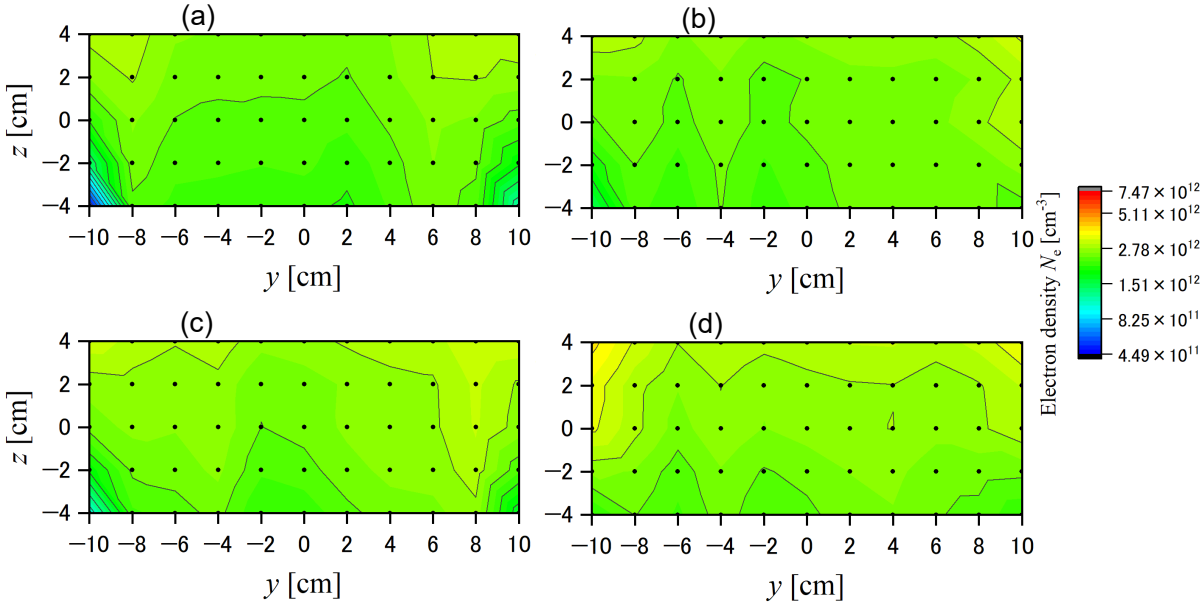

Fig. 4.18: Dependence of electron density on spatial position and power at p = 1 Pa. (a), (b), (c), and (d) are the results at $P = 200$, 400, 600, and 800 W, respectively. Reproduced from Yuya Yamashita *et al.*, J. Vac. Sci. Technol. A, **42**, 023003, (2024) [5] with permission from the American Vacuum Society (AVS).

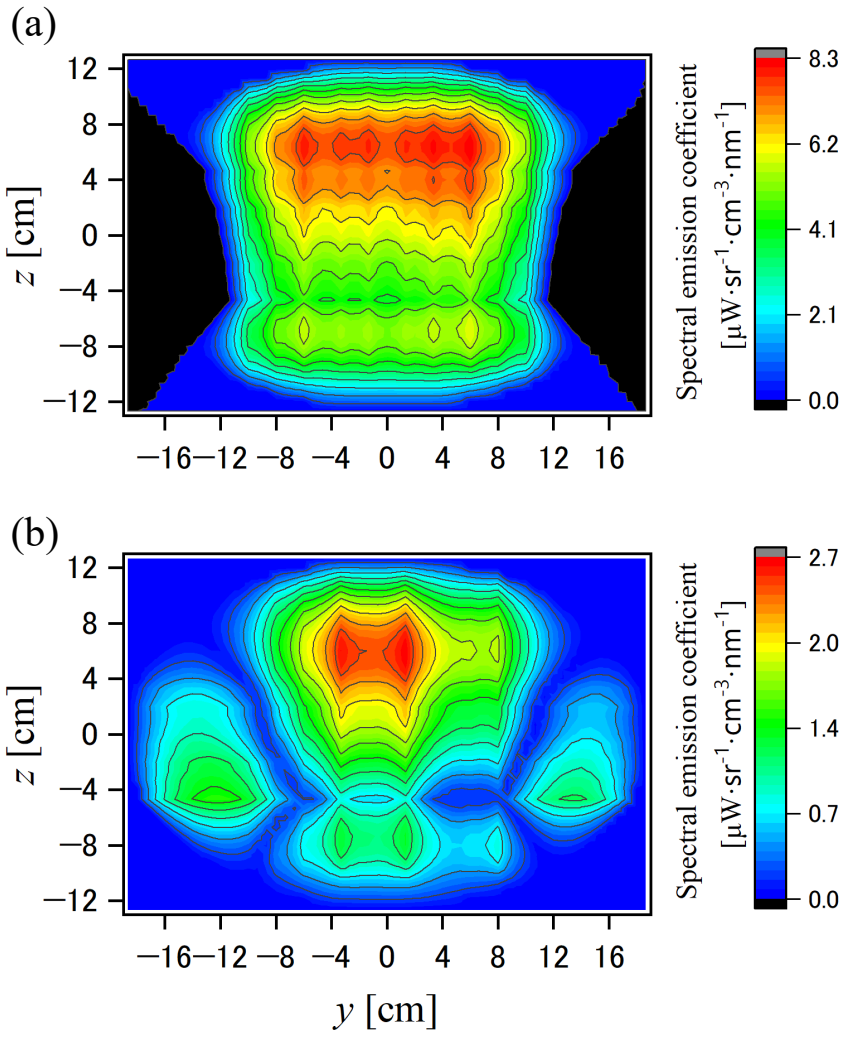

Fig. 4.19: Spacial dependence of spectral emission coefficient at 708.6 nm on $p = 10\,\mathrm{Pa}, P =$ 800W. (a) and (b) show the average and range of three times measurement, respectively. Reproduced from Yuya Yamashita *et al.*, J. Vac. Sci. Technol. A, **42**, 023003, (2024) [5] with permission from the American Vacuum Society (AVS).

corresponds to the area near the quartz window just below the antenna, and it is possible that the repeated uncertainty in the impedance matching may have affected the changed electromagnetic field generated by the antenna. In each of the three measurements, the variable capacitor constant of the auto-matcher changed in each trial. This suggests that the impedance of the plasma as the object of observation as well as the spectral emission coefficient distribution of the plasma itself changed from trial to trial. Hence, the range of spectral emission in the area located just below the antenna would have been larger. This result suggests that the uncertainty in plasma diagnostics performed by combining tomographic optical emission spectroscopy measurements and CR modeling will increase if all lines-of-sight are not acquired simultaneously. In particular, the simultaneous acquisition of all lines-of-sight is important for plasma diagnostics that combine tomographic optical emission spectroscopy and CR modeling.

This result suggests that in order to reduce the uncertainty of the spectral emission coefficient as a reconstructed image in tomographic optical emission spectroscopy, it is necessary to simultaneously acquire the spectral radiance of the entire line-of-sight of the cross section under observation. The position of the T_e maximum is just below the antenna, near $y = 0\,\mathrm{cm}$ and $z = 4\,\mathrm{cm}$, the same position where the spectral emission coefficient reached its maximum value.

In other words, time evolution of the T_e of the plasma could be observed. The results further support the importance of the simultaneous acquisition of all lines-of-sight in plasma diagnostics based upon tomographic optical emission spectroscopy combined with the CR modeling, as mentioned above.

The areas around $y = 12$ to $16\,\mathrm{cm}$, $z = -6$ to $4\,\mathrm{cm}$ and $y = -16$ to $-12\,\mathrm{cm}$, $z = -6$ to $4\,\mathrm{cm}$ also showed characteristic distributions. They correspond to the positions where the spectral emission coefficient as a reconstructed image exhibits a negative value and where there is no line-of-sight intersection. Furthermore, spectral emission coefficients in those areas are smaller than in other areas. Therefore, in those areas, it was considered that the signal-to-noise ratio on OES measurements was smaller. Therefore, the iterative uncertainty is considered to have increased.

The method was employed by this study, which simultaneously measures all the lines-of-sight of the measured cross section. As mentioned above, the method has the advantage that there is no uncertainty in the reconstructed image due to the time evolution of the plasma. However, in the same method, the number of lines-of-sight is generally lower than that of the

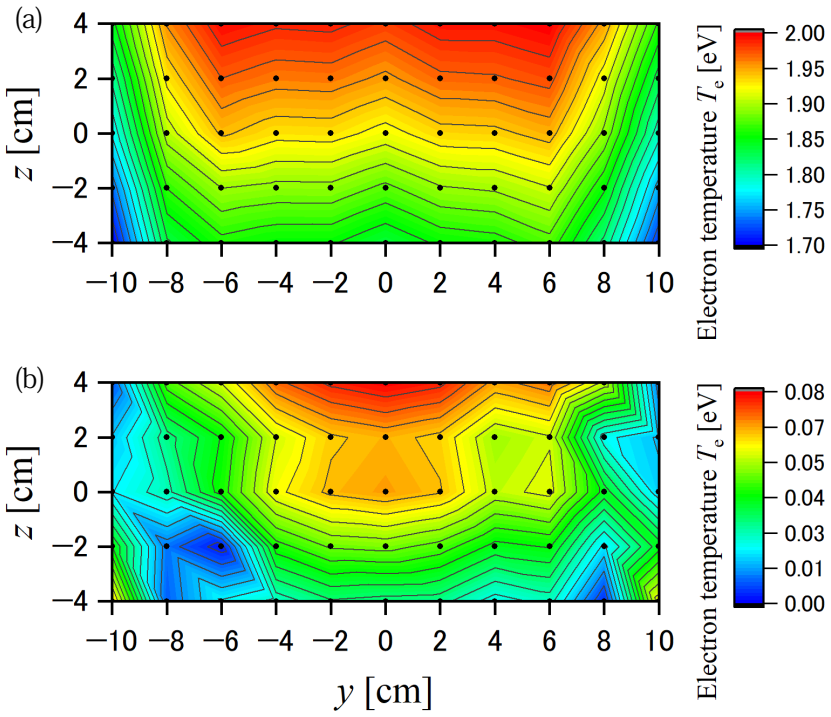

Fig. 4.20: Spacial dependence of electron temperature on $p = 10\,\mathrm{Pa}, P = 800\mathrm{W}$. (a) and (b) show the average and range of three times measurement, respectively. Reproduced from Yuya Yamashita *et al.*, J. Vac. Sci. Technol. A, **42**, 023003, (2024) [5] with permission from the American Vacuum Society (AVS).

line-of-sight scanning method due to objective overlap of lenses and equipment cost. In particular, the system in which plasma is observed from outside the observation window, as in this study, has the advantage of not disturbing the plasma in the depressurization process. However, the method has the disadvantage of the limitation of the number or placement of lines-of-sight. Future work is to improve the spectral tomography algorithm.

On the other hand, the range of N_e was spatially nearly uniform. This is thought to be because the absolute value of N_e was nearly uniform spatially, and the effect on repeatability was small.

To discuss the fitting uncertainty of Eq.(4.20), the reduced population density: $n_{i\mathrm{model}}/g_i$ was recursively calculated by Ar CR model to substitute T_e and N_e which were diagnosed by the fitting of the Ar CR model as shown in Figs. 4.20 and 4.21. Figure 4.22 shows the result. The difference between $n_{i\mathrm{OES}}/g_i$ and $n_{i\mathrm{model}}/g_i$ was larger in Vlcek level number $i = 21$ compared to $i = 6$, 7, 8, and 9. It is due to the absolute value of the spectral radiance of the transition that was small, so the uncertainty of $n_{i\mathrm{OES}}$ becomes large.

Figure 4.23 shows the dependence of the optical escape factor from ion level on excitation state levels. The levels except for the Vlcek level numbers 3, 5, 12, 15, 16, 17, 20, 21, 26,

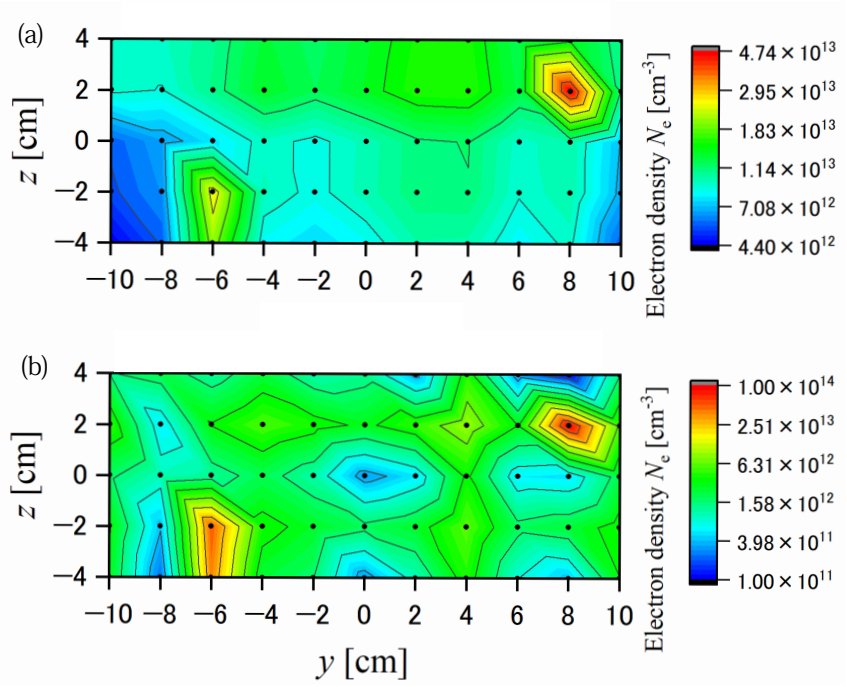

Fig. 4.21: Spacial dependence of electron density on $p = 10\,\mathrm{Pa}, P = 800\mathrm{W}$. (a) and (b) show the average and range of three times measurement, respectively. Reproduced from Yuya Yamashita *et al.*, J. Vac. Sci. Technol. A, **42**, 023003, (2024) [5] with permission from the American Vacuum Society (AVS).

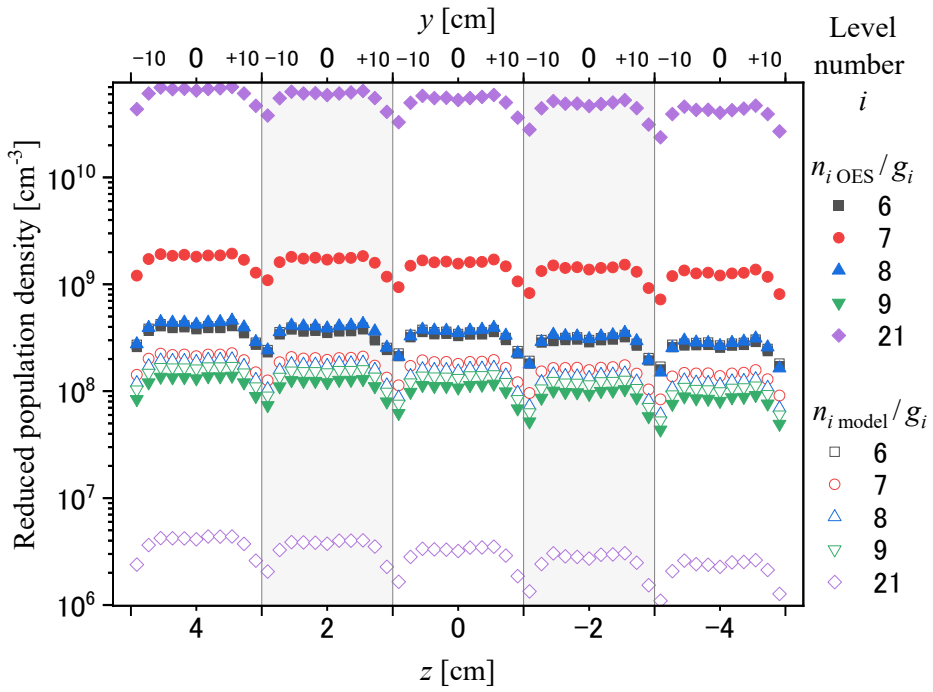

Fig. 4.22: The dependence of reduced population density of electron density on the position at $p = 10\,\mathrm{Pa}, P = 800\mathrm{W}$. This figure shows the result of the average of three times measurements. Reproduced from Yuya Yamashita *et al.*, J. Vac. Sci. Technol. A, **42**, 023003, (2024) [5] with permission from the American Vacuum Society (AVS).

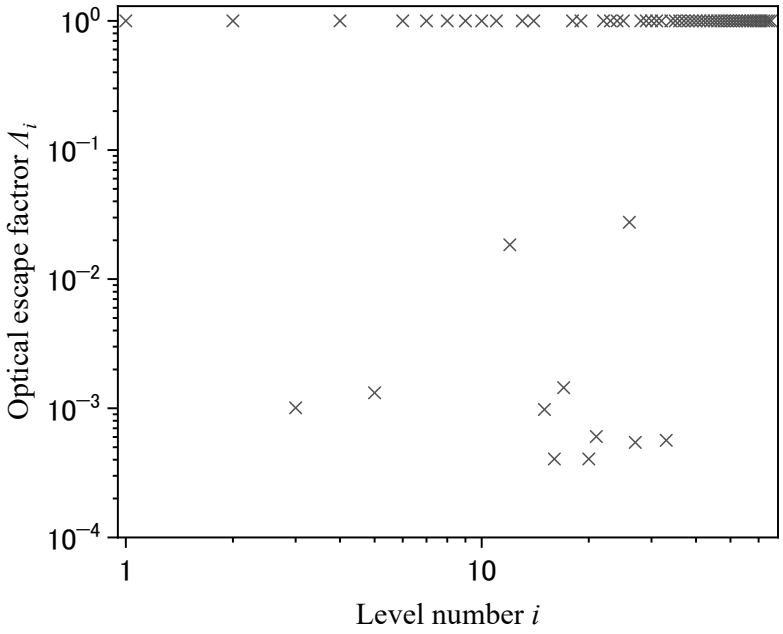

Fig. 4.23: Optical escape factor $p = 10\,\mathrm{Pa}$, $P = 800\mathrm{W}$. This figure shows the results of the average of three measurements, with data points in the range $-10\,\mathrm{cm} \leq y \leq 10\,\mathrm{cm}$ and $-4\,\mathrm{cm} \leq z \leq 4\,\mathrm{cm}$ on Figs. 4.20 and 4.21. Reproduced from Yuya Yamashita *et al.*, J. Vac. Sci. Technol. A, **42**, 023003, (2024) [5] with permission from the American Vacuum Society (AVS).

27, and 33 were optically thin, i.e., their optical escape factors were equal to one. Vlcek level 21 was the only nonone in the levels that were employed for fitting in this study as shown in Tab.4.1. This may have affected the convergence of same-level fitting. In this study, the results are presented using the CR model that considers optical thickness for some transitions, as shown in Eq. (4.19).

To discuss optical escape factor, we attempted to fit T_e and N_e under assuming optically thin for all transitions, but the results did not converge within the search range. This result suggests the validity of the model employed in this study. However, the model does not take into account the optical thickness between the excited levels, which is an issue for future work.

4.6 Conclusion

An optical system was constructed to simultaneously acquire the spectral radiance of 18 lines-of-sight for tomographic OES measurement of low-pressure inductively coupled plasma. The optical system is located outside of the plasma system, which means that it is an undis-

turbing plasma diagnostic technique and highly applicable to process equipment. The position dependence of the spectral emission coefficients was obtained from the spectral radiance by spectral tomography calculations. The spatial distribution of the number density of excited levels was obtained based on the emission line spectra. The spatial distribution of the excited level number density was analyzed based on a CR model to diagnose the spatial distribution of T_e and N_e.

The effects of antenna power and total pressure on T_e and N_e are revealed. The effect of the placement of line-of-sight and plasma time evolution on T_e and N_e from spectral tomography measurements and CR modeling is discussed.

Chapter 5

Conclusion

5.1 Conclusion of this study

This study aimed to realize positional distribution diagnostics of plasmas by OES measurement. To achieve this goal, a diagnostic method based on tomographic OES measurement and CR model was proposed and established in this thesis. The core content of this thesis consists of the two original papers [4, 5]. The first part of the core content—Chapter 3—established a method for compensating multiple reflections from the chamber inner wall and for radial distribution diagnosis with the multiple reflection compensation. This chapter was positioned as preliminary research to achieve the objective. The second part of the core content—Chapter 4—has achieved the objective of this thesis. The overall conclusions of this study are summarized below. Note that the differences in the experiments and analysis between Chapters 3 and 4 are shown in Table 5.1.

In Chapter 3, a simple method for measuring the spectral reflectance of the chamber inner wall was developed, since multiple reflections on the chamber inner wall cause uncertainty in the measurement of the spectral emission coefficient. Under the assumption of axial symmetry in the spatial distribution of the low-pressure ICP plasma, an analysis method for calculating the net spectral emission coefficient with the multiple reflection compensation was developed. Furthermore, by analyzing based on an argon CR model, the measurement of the radial dependence of T_e and N_e was realized. This quantitatively clarified the effect of multiple reflections on the diagnostic results. In addition, by using Langmuir probe measurements and electromagnetic simulations, the effect of the antenna shape and window arrangement on the plasma characteristics was discussed. Furthermore, the need for analysis that does not assume axial symmetry, that is, tomographic OES measurement, was also experimentally highlighted.

In Chapter 4, the development of positional distribution diagnosis based on tomographic

Table 5.1: Overview of main differences on experiments and analysis in Chapters 3 and 4

Chapter	Chapter 3	Chapter 4
Spectrometer	MS3504i	M116
Detector	DU420A-OE	(integrated)
Wavelength resolution [nm]	0.22 (FWHM)	2.19 (FWHM)
Number of line-of-sights	10 (per side)	18
Line-of-sight scanning	sequentially	simultaneously
Measured plane	$x-y$ plane at $z=0$ cm (horizontal plane)	$y-z$ plane at $x=0$ cm (vertical plane)
Compensation of multiple reflected light	with	without
Assumptions on reconstruction	z-axis symmetry	none
Resolution of reconstructed plane	17.7 mm/segmented radius	6.667 mm/pixel
Number of optical emission lines employed in diagnosis	11	9, 10, or 11

OES measurement and CR model was established. In the experimental verification, an optical system capable of simultaneously acquiring the spectral radiance of 18 lines-of-sight for low-pressure ICP was constructed. The positional distribution of excited level number density was obtained by spectral tomography calculation. The positional distribution of T_e and N_e was diagnosed by the CR model. From these results, the effects of antenna power and total pressure on the plasma positional distribution were clarified.

These results provide a new methodology for understanding the positional characteristics of plasma. This method also represents an important step toward understanding plasma kinetics and developing plasma control technology. The knowledge gained through this research will contribute greatly to the advancement of spectroscopic measurement technology and is expected to become a fundamental technology for achieving advanced control of plasma processes in the future. However, this research also revealed several directions for future research approaches, which will be discussed in the next section.

5.2 Future prospects and challenges of plasma diagnostics based on optical emission spectroscopic measurements

In this section, the prospects and challenges of plasma diagnostics based on OES measurements are discussed. The potential for advancements in plasma diagnostics is proposed by examining different diagnostic purposes, measurement accuracy, and a systematic approach. Ad-

ditionally, the significance of interdisciplinary collaboration for future advancements in plasma science and engineering is reiterated.

5.2.1 Dependence of plasma diagnostics requirements on their purpose

The purposes of plasma diagnosis are diverse [88, 89], and the requirements of plasma diagnostics differ accordingly. This thesis classifies the purposes of plasma diagnostics into the following two categories. The first type is diagnosis to understand phenomena. The second type is diagnostics for sensing methods. The challenges for each purpose will be discussed as follows.

First, the discussion focuses on **plasma diagnostics to clarify phenomena**. In other words, the purpose is to clarify and understand phenomena in plasma science and engineering, either in plasma alone or in the interaction of plasma with other solids or liquids. Specific examples of diagnostic applications for this purpose include clarifying the mechanisms of the generation and annihilation of various atomic species in plasma and clarifying the effects of electromagnetic field distribution on plasma and workpieces by coupled analysis with electromagnetic field simulation. For this purpose, **trueness**[1] should be prioritized in requirements for diagnostics.

Next, the discussion focuses on **plasma diagnostics for sensing methods**. Sensing here can refer to feedback in control systems or sensing to obtain data for monitoring or sampling in industrial engineering. Specific applications of diagnostics for this purpose include feedback control of the plasma, *in situ* sensing of a workpiece to ensure that the desired post-processing properties are achieved, and anomaly detection and rejection in production control. For this purpose, **precision**[2] should be prioritized in requirements for diagnostics.

5.2.2 Accuracy on plasma diagnosis by optical emission spectroscopic measurement

In this section, the accuracy[3] of plasma diagnostics based on OES measurements and CR models will be discussed. In this context, the proposed method of this thesis —namely, positional diagnosis based on tomographic OES measurement and CR model—is employed as a case in point for discussion. The experimental and analytical stages can be roughly divided

[1] **Trueness** is defined as "closeness of agreement between the average of an infinite number of replicate measured quantity values and a reference quantity value [90]".

[2] **Precision** is defined as "closeness of agreement between indications or measured quantity values obtained by replicate measurements on the same or similar objects under specified conditions [90]".

[3] **Accuracy** is defined as "closeness of agreement between a measured quantity value and a true quantity value of a measurand [90]". Accuracy is a concept that encompasses both trueness and precision.

into four stages: Step1) **OES measurement experiment**, Step2) **Analysis based on spectral tomography**, Step3) **Analysis of excited-level density**, and Step4) **Analysis based on CR model**.

The sources involved in each step are as follows. The underlined sources in the following list denote the sources which were revealed in this study.

Step 1) **OES measurement experiment**—Aberration of each equipment constituting the spectroradiometric system, Measurement position, Quantization of wavelength and spectral radiance, Wavelength calibration and spectral radiance calibration, Light reflection on view windows and chamber inner wall surface [4][4], Optical resolution, In-plane inhomogeneity in the field-of-view cross-section, and Changes in the system over time (repeatable reproducibility)

Step 2) **Analysis based on spectral tomography**[5]—Reconstruction algorithms, Device dimensions, Reconstruction resolution

Step 3) **Analysis of excited-level density**—Separation of continuum spectrum and line spectrum, Function fitting to obtain emission coefficient, Identification of line, A coefficient [91]

Step 4) **Analysis based on CR model**—Input parameters of the CR model (including due to assumed or measured parameters); Inherent in the CR model (including Omission of elementary processes in modeling [92], Reaction cross sections, Grouping of excited levels, and Optical escape factors [91]); and Diagnostic analysis based on CR models (including Mathematical uncertainties due to the solution search algorithm or objective function, Choosing of excision levels, and Excitation levels density not measured by OES measurement)

The sources of uncertainty described above are just a few examples, and there are many more [93–95]. From acquiring spectral radiation to diagnosis, various analytical theories and experimental techniques are involved in a complex manner [96]. As such, it is clear that plasma diagnostics is a complex system.

[4]This includes resulting from the geometric shape of the structures within the chamber. In addition, for plasma processes such as film formation and etching, changes in the reflectance of chamber inner wall surfaces [60] and the transmittance of observation windows as the processes progress can be sources of uncertainty.

[5]On the other hand, when position-resolved measurements are not carried out, or when measurements assume a positional distribution of the plasma (such as in Abel inversion), there is inherent uncertainty in the positional distribution.

5.2.3 Necessity of systematic approach on plasma diagnosis

Plasma diagnostics by OES measurements can be considered a kind of system, with plasma light emission as input and plasma parameters as output. The author emphasizes that the elements of the system proposed in this thesis include not only experimental data analyzers, but also hardware such as radiometric systems.

However, there have been no reports of the systematic approach (or operations research approach) in the research and practice of plasma diagnostics. One of the reasons why the systematic approach has not been put into practice is considered to be that plasma diagnostics is extremely complex to understand as a system. One reason for this is that analyzing systems has been difficult due to computational resource limitations, especially before today's high-speed computing became available at low cost.

However, this thesis proposes that the systematic approach is also necessary in the research and practice of plasma diagnostics. Because, as mentioned above, there are a huge number of parameters or methodologies for realizing or designing plasma diagnostics systems. Optimization of parameters or methodologies of plasma diagnostic systems is essential to realistically achieve accurate diagnostics. However, the optimal solution varies depending on the individual diagnostic purpose, measurement target, and even constraints[6]. The systematic approach is essential to find the optimal solution. Furthermore, bottlenecks exist in systems. The systematic approach is essential in plasma diagnostics systems to investigate and resolve bottlenecks. There is one more reason why a systematic approach is necessary. A systematic approach has a high affinity with information engineering. This compatibility enables the integration of systematic methodologies with advanced information science and engineering, such as machine learning and data mining. As a result, a hybrid approach of systematic and information technology can facilitate advanced and diverse plasma diagnostics. As machine learning approaches are increasingly being reported in plasma diagnostic analysis [97–100], plasma chemical reaction analysis [101, 102] and post-processing propertiy prediction [103, 104], the need for such a hybrid approach is growing rapidly.

The systematic approach is important not only for the application of plasma diagnostics in engineering, but also for research into plasma diagnostics itself, and in plasma physics and chemistry as fundamental science. For example, diagnostics with explicitly stated uncertainties, which would be possible with a systematic approach, would increase the reliability of popula-

[6]The constraints here can encompass not only scientific and technological limitations but also socio-economic or engineering factors, such as resource and cost limitations.

tion kinetic considerations based on diagnostic results.

However, the systematic approach is just one of many research philosophies or strategies, and other approach are equally important and should be respected. This will be discussed in the next section.

5.2.4 Towards advancements in plasma science and engineering: the importance of interdisciplinary collaboration

In recent years, plasma engineering and industrial applications have advanced, with surprising expansions into multiple fields. For example, through advancements in semiconductor devices, society is benefiting from these developments in everyday life. In some perspectives, research that is directly connected to products and solutions is often regarded as the sole valuable pursuit.

However, the author strongly emphasizes that basic research holds immense value and serves as a platform, being a cornerstone of plasma science and engineering. As mentioned in Chapter 1, research and development that rely solely on engineering approaches—such as the trial-and-error approach—have limitations. The importance of promoting basic plasma science research, including plasma diagnostics, lies not only in its value as pure science but also in its contribution to breakthroughs in engineering fields and applications. For example, atomic and molecular physics provide the understanding and modeling of atomic and molecular processes, which are the fundamental principles of plasma diagnostics through OES measurement —something that goes without saying. Furthermore, atomic and molecular physics can be regarded as the fundamental source of innovative advancements in plasma processes and semiconductor devices.Furthermore, atomic and molecular physics serves as the foundation for many innovative advancements in plasma processes and semiconductor devices.

Both the fundamental and applied approaches should be regarded as indispensable and complementary, each with its own multifaceted and diverse contributions, based on mutual respect, rather than opposing. It is well known that the field of plasma science and engineering is an interdisciplinary field. Plasma diagnostics is also an interdisciplinary field.

The author believes that further mutual exchange and solidarity, respecting the individuality, interests, and diversity of researchers within the research communities of plasma basic science, plasma diagnostics, plasma applications, as well as information engineering, applied mathematics, and other related fields, and so on, are essential for the academic development of this field and beyond. Furthermore, such efforts will contribute to solving societal problems.

Just as the theory of relativity, which was purely fundamental physics a century ago, is now applied to satellite positioning, navigation, and timing systems as engineering, supporting our lives... Or, just as the progress of computer engineering is the source of development in basic science today...

The author would like to conclude this thesis with a hope for continued progress in plasma science and engineering, along with a strong determination to continue contributing to this field, however modestly.

Appendix A

Supplementary data for Chapter 3

[This appendix has been supplemented in this thesis to deepen the reader's understanding and was not included in the original paper [4].] Figures A.1 and A.2 show the spectral radiance on the air-side of the window surface: $L'_{\mathrm{I}}(\lambda)$ which is defined in Eq (3.20) in Section 3.3.2.

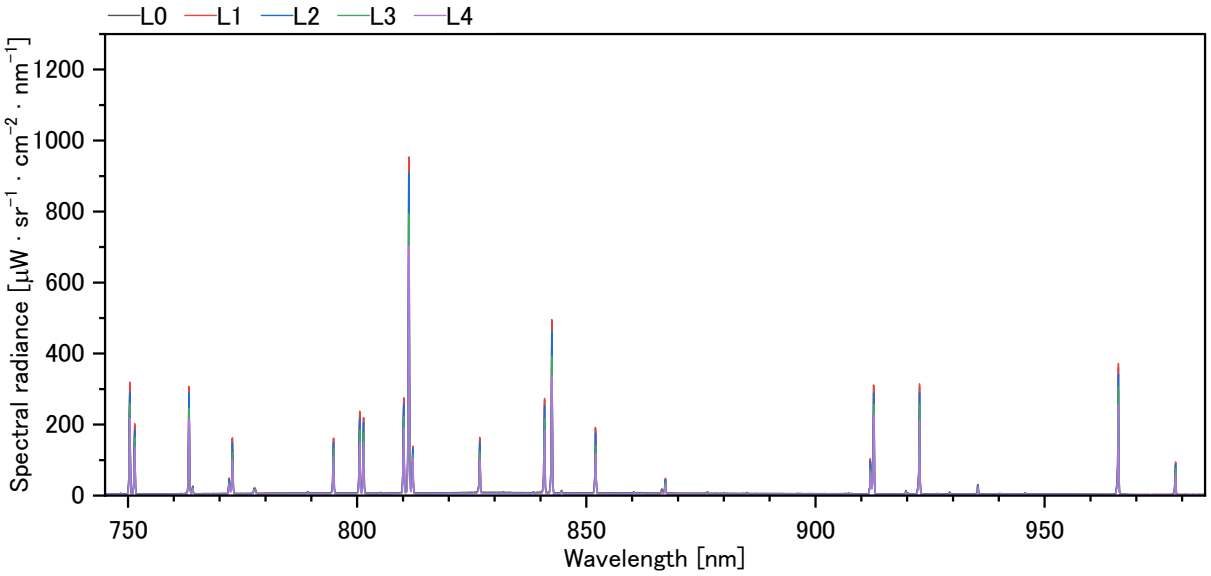

(a) Lines-of-sight L0 to L4.

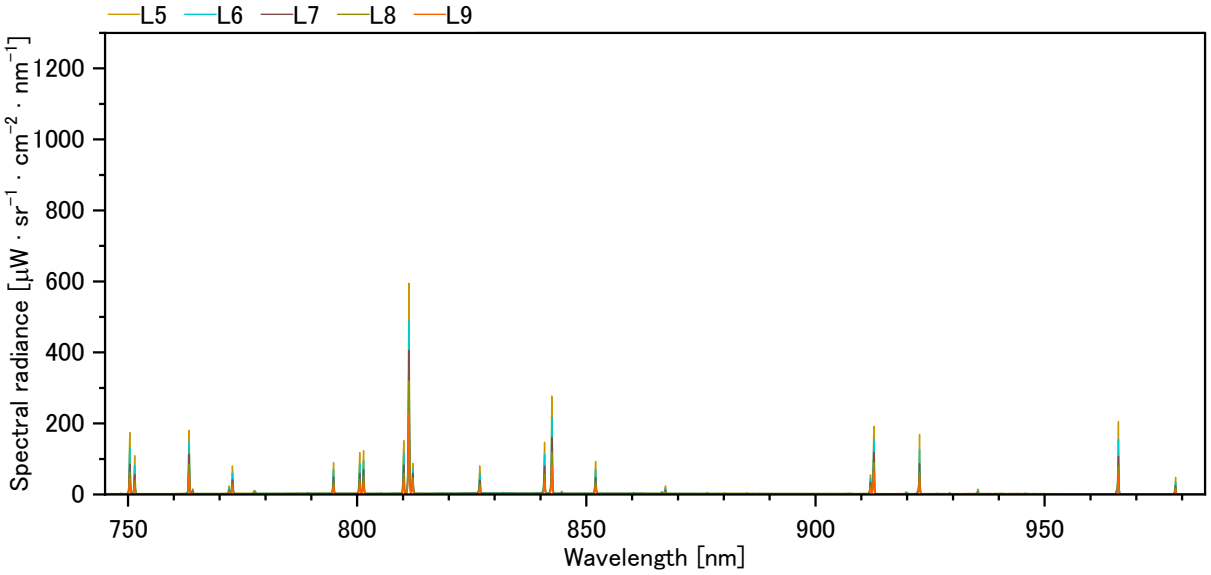

(b) Lines-of-sight L5 to L9.

Fig. A.1: Lines-of-sight (L0 - L9) dependence of the spectral radiance on the air-side of the window surface: $L_1'(\lambda)$ at pressure p = 1 Pa and power P = 300 W. The arrangement and numbering of the lines-of-sight are as shown in Fig. 3.9. [This figure has been supplemented in this thesis to deepen the reader's understanding and was not included in the original paper [4].]

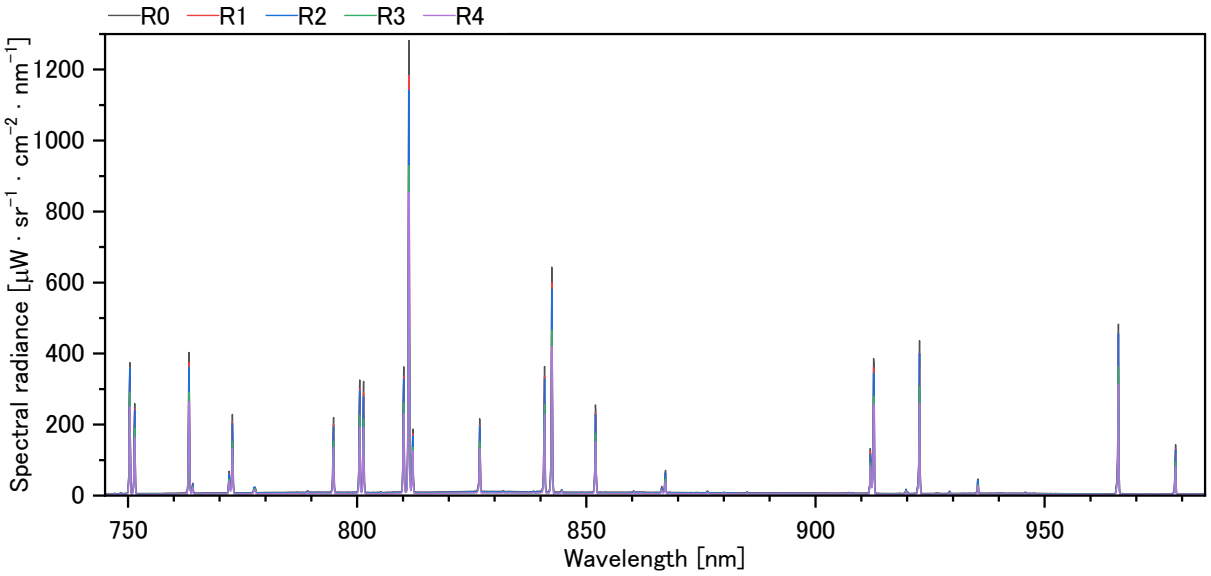

(a) Lines-of-sight R0 to R4.

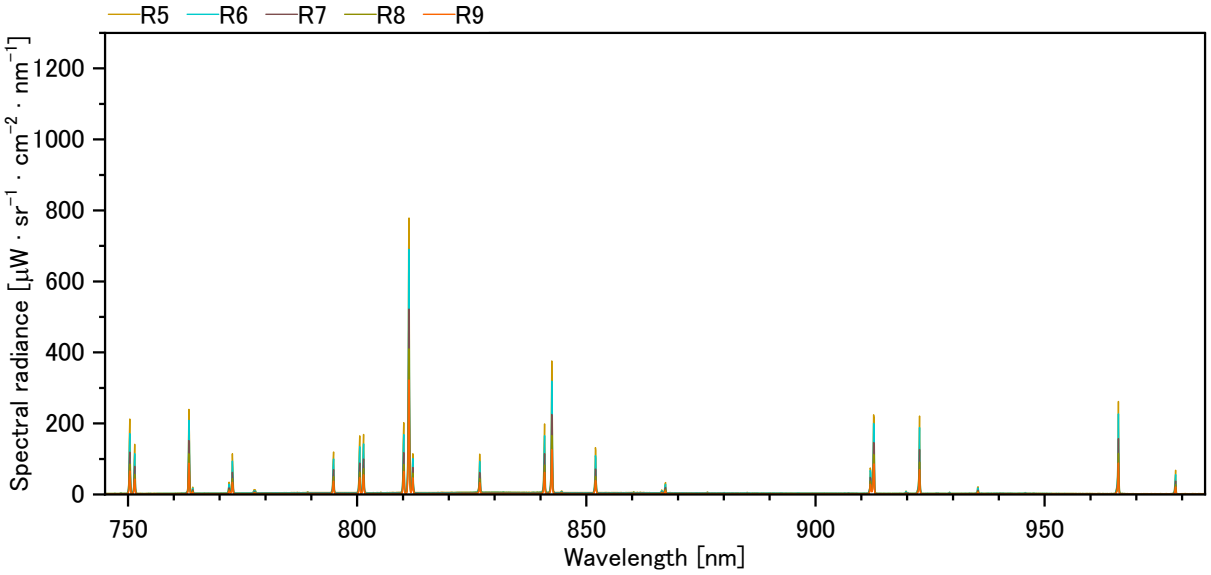

(b) Lines-of-sight R5 to R9.

Fig. A.2: Lines-of-sight (R0 - R9) dependence of the spectral radiance on the air-side of the window surface at pressure $p = 1$ Pa and power $P = 300$ W. The arrangement and numbering of the lines-of-sight are as shown in Fig. 3.9. [This figure has been supplemented in this thesis to deepen the reader's understanding and was not included in the original paper [4].]

Appendix B

Supplementary data for Chapter 4

[This appendix has been supplemented in this thesis to deepen the reader's understanding and was not included in the original paper [5].] Figure B.1 shows an example of the spectral radiance on the vacuum-side of the window surface: $L_{\mathrm{plasma}}(\lambda)$, obtained as an output of Fig. 4.5 in Section 4.2.2.

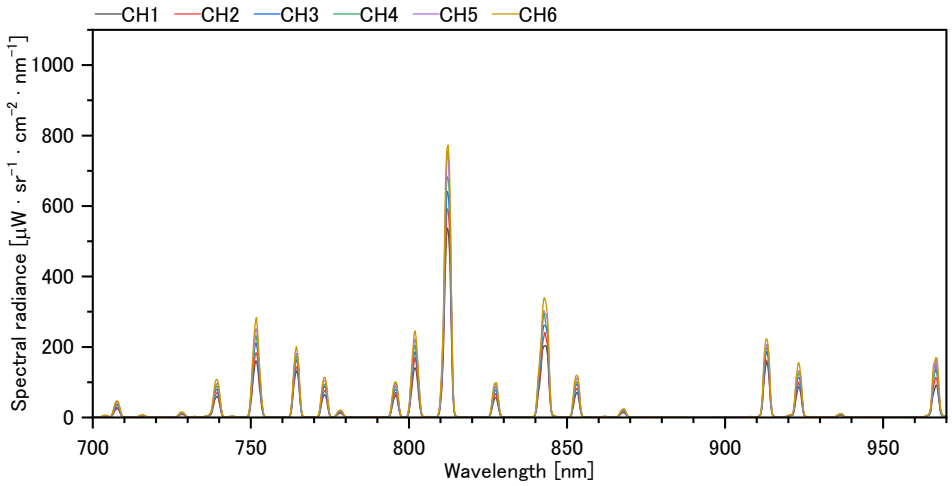

(a) Channels (CH) 1 to 6 are horizontal lines-of-sight, positioned at z = -4.9, -3.5, -2.1, -0.7, 0.7, and 2.1 cm, respectively.

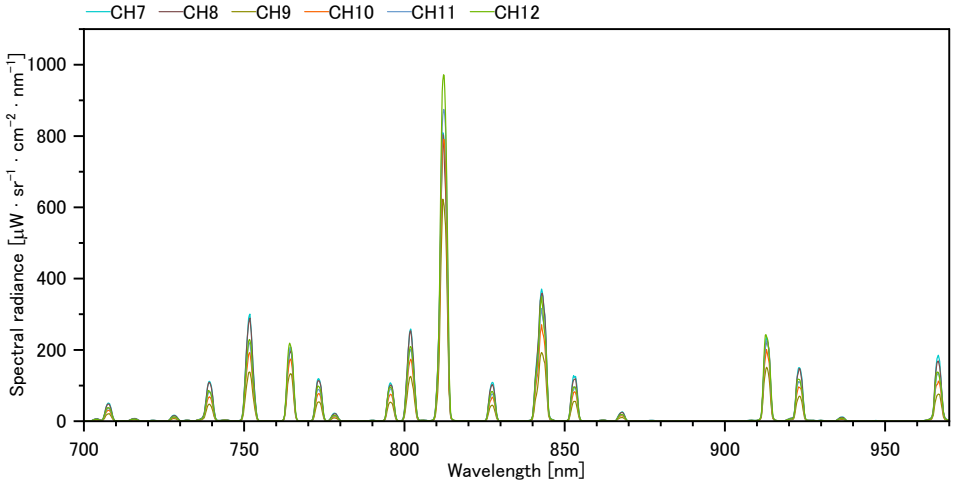

(b) Channels (CH) 7 and 8 are horizontal lines-of-sight, positioned at z = 3.5 and 4.9 cm, respectively. CH 9 to 12 are vertical lines-of-sight, positioned at y = -10.0, -8.0, -5.8, and -3.6 cm, respectively.

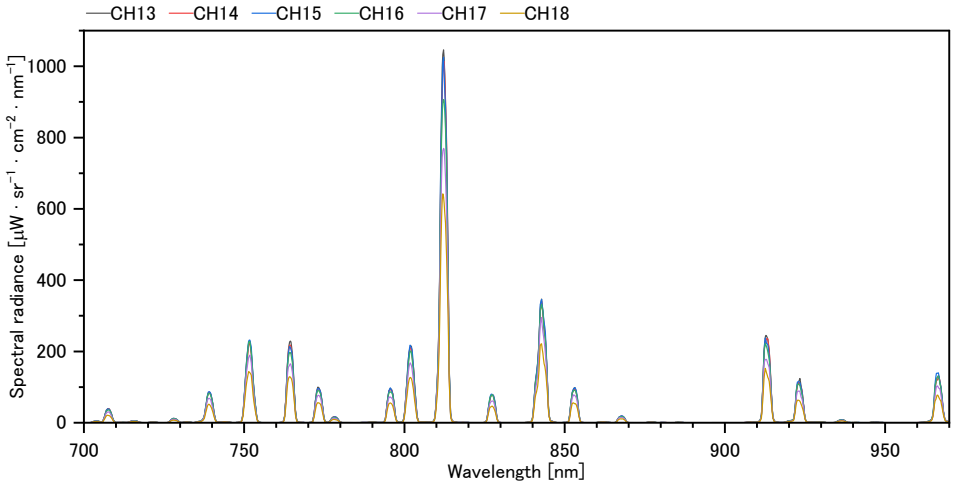

(c) Channels (CH) 13 to 18 are vertical lines-of-sight, positioned at y = -1.2, 1.2, 3.6, 5.8, 8.0, and 10.0 cm, respectively.

Fig. B.1: Lines-of-sight dependence of spectral radiance on the vacuum-side of the window surface at pressure p = 10 Pa and power P = 800 W. [This figure has been supplemented in this thesis to deepen the reader's understanding and was not included in the original paper [5].]

Bibliography

[1] Y. Yamashita, K. Doi, T. Kiyota, A. Kobayashi, S. Hosoya, K. Yoneda, A. Nezu, and H. Akatsuka, "Position dependence diagnosis of electron temperature and density of inductively coupled argon plasma based on Abel inverted optical emission spectroscopic measurement and collisional-radiative model," in *11th International Conference on Reactive Plasmas (ICRP-11) / 75th Annual Gaseous Electronics Conference (GEC2022)*, Sendai, Japan, 2022, conference proceedings, pp. 141–142, https://meetings.aps.org/Meeting/GEC22/Session/HT4.22 https://www.ecei.tohoku.ac.jp/plasma/ICRP-11/

[2] Y. Yamashita, K. Doi, T. Kiyota, K. Asakawa, S. Hosoya, W. Kikuchi, A. Nezu, and H. Akatsuka, "Diagnosis of spatial distribution of electron temperature and electron density of argon inductively coupled plasma by tomographic optical emission spectroscopic measurement," in *XXXVth International Conference on Phenomena in Ionized Gases (ICPIG 2023)*, Egmond aan Zee, Netherlands, 2023, conference proceedings, p. 240, https://www.icpig2023.com/ [Available online]: https://cdn.aanmelderusercontent.nl/i/doc/d2663742727c669e2bb8bd98c4f93fac

[3] Y. Yamashita, K. Doi, T. Kiyota, S. Watanabe, K. Shimatani, W. Kikuchi, Y. Ye, A. Nezu, and H. Akatsuka, "Electron temperature diagnosis of CF_4/O_2 plasma based on fluorine atomic corona model by tomographic optical emission spectroscopic measurement," in *26th Europhysics Conference on Atomic and Molecular Physics of Ionized Gases (ESCAMPIG 2024)*, Brno, Czech Republic, 2024, conference proceedings, p. P2-T5-29, https://escampig2024.physics.muni.cz/

[4] Y. Yamashita, K. Doi, T. Kiyota, K. Asakawa, S. Hosoya, W. Kikuchi, A. Nezu, and H. Akatsuka, "Radial dependence diagnosis of inductively coupled Ar plasma based upon optical emission spectroscopic measurement with spectral reflectance

compensation," *Review of Scientific Instruments*, vol. 94, no. 8, p. 083503, 2023, https://doi.org/10.1063/5.0138912

[5] Y. Yamashita, K. Doi, T. Kiyota, K. Ishi, S. Watanabe, W. Kikuchi, A. Nezu, and H. Akatsuka, "Spatial distribution diagnosis of electron temperature and density of argon inductively coupled plasma by tomographic optical emission spectroscopic measurement and collisional-radiative model," *Journal of Vacuum Science & Technology A*, vol. 42, no. 2, p. 023003, 2024, https://doi.org/10.1116/6.0003209

[6] H. Sugai and K. Ohe, *Plasma Electronics*（プラズマエレクトロニクス）. Tokyo, Japan: Ohmsha, 2000, [in Japanese], ISBN: 978-4-274-13210-0, http://id.ndl.go.jp/bib/000002916530

[7] H. Kunieda, "4.High-Resolution Spectroscopy of Astrophysical Plasmas," *Journal of Plasma and Fusion Research*, vol. 79, no. 4, pp. 377–385, 2003, [in Japanese], https://doi.org/10.1585/jspf.79.377

[8] M. Laroussi, "Low Temperature Plasma-Based Sterilization: Overview and State-of-the-Art," *Plasma Processes and Polymers*, vol. 2, no. 5, pp. 391–400, 2005, https://doi.org/10.1002/ppap.200400078

[9] M. A. Lieberman and A. J. Lichtenberg, *Principles of Plasma Discharges and Materials Processing*, 2nd ed. Hoboken, New Jersey, USA: John Wiley & Sons, Inc., 2005, ISBN: 978-0-471-72001-0, https://www.doi.org/10.1002/0471724254

[10] M. A. Lieberman and A. J. Lichtenberg, *Principles of Plasma Discharges and Materials Processing*（プラズマ/プロセスの原理）, 2nd ed., translated by M. Hori and H. Sato from [9]. Tokyo, Japan: Maruzen, 2010, [in Japanese], ISBN: 978-4-621-08223-2, http://id.ndl.go.jp/bib/000010688965

[11] F. J. Arellano, M. Kusaba, S. Wu, R. Yoshida, Z. Donko, P. Hartmann, T. V. Tsankov, and S. Hamaguchi, "First-principles simulation of optical emission spectra for low-pressure argon plasmas and its experimental validation," *Plasma Sources Science and Technology*, vol. 32, no. 12, p. 125007, 2023, https://doi.org/10.1088/1361-6595/ad0ede

[12] F. J. Arellano, M. Kusaba, S. Wu, R. Yoshida, Z. Donko, P. Hartmann, T. V. Tsankov, and S. Hamaguchi, "Machine learning-based prediction of the electron energy

distribution function and electron density of argon plasma from the optical emission spectra," *Journal of Vacuum Science & Technology A*, vol. 42, no. 5, p. 053001, 2024, https://doi.org/10.1116/6.0003731

[13] S. Datta, J. G. Han, R. Kumar, and B. B. Sahu, "Experimental studies and COMSOL 1-D simulation in Ar capacitively coupled plasmas," *AIP Advances*, vol. 14, no. 1, p. 015046, 2024, https://doi.org/10.1063/5.0174990

[14] S. Hamaguchi, I. Murakami, D. Kato, and The Japan Society of Plasma Science and Nuclear Fusion Research, Eds., *Handbook of Atomic and Molecular Processes in Plasmas*（プラズマ原子分子過程ハンドブック）. Suita, Japan: Osaka University Press, 2011, [in Japanese], ISBN: 978-4-87259-362-4, http://id.ndl.go.jp/bib/000011184832

[15] T. A. Badgwell, T. Breedijk, S. G. Bushman, S. W. Butler, S. Chatterjee, T. F. Edgar, A. J. Toprac, and I. Trachtenberg, "Modeling and control of microelectronics materials processing," *Computers & Chemical Engineering*, vol. 19, no. 1, pp. 1–41, 1995, https://doi.org/10.1016/0098-1354(94)E0038-O

[16] T. F. Edgar, S. W. Butler, W. J. Campbell, C. Pfeiffer, C. Bode, S. B. Hwang, K. S. Balakrishnan, and J. Hahn, "Automatic control in microelectronics manufacturing: Practices, challenges, and possibilities," *Automatica*, vol. 36, no. 11, pp. 1567–1603, 2000, https://doi.org/10.1016/S0005-1098(00)00084-4

[17] C. S. Moon, K. Takeda, M. Sekine, Y. Setsuhara, M. Shiratani, and M. Hori, "Combinatorial Plasma Etching Process," *Applied Physics Express*, vol. 2, no. 9, p. 096001, 2009, https://doi.org/10.1143/APEX.2.096001

[18] T. Sibillano, A. Ancona, V. Berardi, and P. M. Lugarà, "A Real-Time Spectroscopic Sensor for Monitoring Laser Welding Processes," vol. 9, no. 5, pp. 3376–3385, 2009, https://doi.org/10.3390/s90503376

[19] P. Rajasekaran, C. Ruhrmann, N. Bibinov, and P. Awakowicz, "Space-resolved characterization of high frequency atmospheric-pressure plasma in nitrogen, applying optical emission spectroscopy and numerical simulation," *Journal of Physics D: Applied Physics*, vol. 44, no. 48, p. 485205, 2011, https://doi.org/10.1088/0022-3727/44/48/485205

[20] A. Megía-Macías and O. D. Cortázar, “Review of Spatial Distribution Modes in a 2.45-GHz Hydrogen Plasma,” *IEEE Transactions on Plasma Science*, vol. 47, no. 1, pp. 483–487, 2019, https://doi.org/10.1109/TPS.2018.2877604

[21] K. Ishikawa, K. Karahashi, T. Ishijima, S. I. Cho, S. Elliott, D. Hausmann, D. Mocuta, A. Wilson, and K. Kinoshita, “Progress in nanoscale dry processes for fabrication of high-aspect-ratio features: How can we control critical dimension uniformity at the bottom?” *Japanese Journal of Applied Physics*, vol. 57, no. 6, p. 06JA01, 2018, https://doi.org/10.7567/JJAP.57.06JA01

[22] D. White, D. Boning, S. Butler, and G. Barna, “Spatial characterization of wafer state using principal component analysis of optical emission spectra in plasma etch,” *IEEE Transactions on Semiconductor Manufacturing*, vol. 10, no. 1, pp. 52–61, 1997, https://doi.org/10.1109/66.554484

[23] “International Electrotechnical Vocabulary (IEV) - Part 845: Lighting,” IEC 60050-845:2020, 2020, http://id.ndl.go.jp/bib/031482044 [Available online]: https://electropedia.org/

[24] “Lighting vocabulary,” JIS Z 8113:1998, 1998, [in Japanese], http://id.ndl.go.jp/bib/000003346412

[25] Shoumei-gakkai ed., *Shinpan Hikari no keisoku manual*（新版 光の計測マニュアル）. Tokyo, Japan: JAPAN INDUSTRIAL PUBLISHING, 2022, [in Japanese], ISBN: 978-4-8190-3406-7, http://id.ndl.go.jp/bib/032232860

[26] H.-J. Kunze, *Introduction to plasma spectroscopy*. Berlin, Germany: Springer, 2009, ISBN: 978-3-642-02233-3, https://doi.org/10.1007/978-3-642-02233-3

[27] The Illuminating Engineering Institute of Japan, “Kidokei no seinou hyouka houhou oyobi shiyou houhou（輝度計の性能評価方法及び使用方法）,” Shomei gakkai gijutsu shishin (照明学会技術指針) JIEG-006, 1986, [in Japanese], http://id.ndl.go.jp/bib/026716731

[28] M. Suzuki, T. Nagasaka, M. Habu, K. Yamamura, and M. Nishibori, “A Quartz-bromine Lamp as a Secondary Standard of Spectral Irradiance,” *Journal of the Illuminating*

Engineering Institute of Japan, vol. 57, no. 8, pp. 528–535, 1973, [in Japanese], https://doi.org/10.2150/jieij1917.57.8_528

[29] Y. Iwasa, "A Survey on Realization of Spectral Irradiation Standard by Using High Temperature Blackbody Radiation," *Journal of The Society of Instrument and Control Engineers*, vol. 61, no. 10, pp. 754–761, 2022, [in Japanese], https://doi.org/10.11499/sicejl.61.754

[30] National Institute of Technology and Evaluation, "JCSS Specific Application Documents – Photometry: Luminous Intensity Standard Lamp," JCT21400-12, 2021, [in Japanese], https://www.nite.go.jp/data/000001491.pdf [Online archive]: https://warp.da.ndl.go.jp/info:ndljp/pid/13763105/www.nite.go.jp/data/000001491.pdf

[31] "Methods of colour measurement—Light-source colour," JIS Z 8724:2015, 2015, [in Japanese], http://id.ndl.go.jp/bib/026631133

[32] C. J. Sansonetti, M. L. Salit, and J. Reader, "Wavelengths of spectral lines in mercury pencil lamps," *Applied Optics*, vol. 35, no. 1, pp. 74–77, 1996, https://doi.org/10.1364/AO.35.000074

[33] J. Reader, C. J. Sansonetti, and J. M. Bridges, "Irradiances of spectral lines in mercury pencil lamps," *Applied Optics*, vol. 35, no. 1, pp. 78–83, 1996, https://doi.org/10.1364/AO.35.000078

[34] M. Yamamoto and S. Murayama, *Plasma no bunkou keisoku*（プラズマの分光計測）. Tokyo, Japan: Gakkai shuppan center（学会出版センター）, 1995, [in Japanese], ISBN: 978-4-7622-8784-8, https://doi.org/10.11501/13628809

[35] National Institute of Standards and Technology, *NIST Atomic Spectra Database*, https://www.nist.gov/pml/atomic-spectra-database

[36] R. W. B. Pearse and A. G. Gaydon, *The Identification of Molecular Spectra*, 4th ed. London, UK; New York, USA; (reprinted: Dordrecht, Netherlands): Chapman and Hall ; Wiley; (reprinted: Springer Dordrecht), 1976 (reprinted 2011), ISBN: 0-412-14350-X (reprinted: 978-94-009-5760-2), https://www.springer.com/gp/book/9789400957602

[37] J. S. Chang, R. M. Hobson, Y. Ichikawa, and T. Kaneda, *Denri kitai no genshi-bunshi katei*（電離気体の原子・分子過程）. Tokyo, Japan: Tokyo Denki University Press, 1982, [in Japanese], ISBN: 978-4-501-00570-2, https://doi.org/10.11501/12704099

[38] *LXCat*, http://www.lxcat.net

[39] S. Pancheshnyi, S. Biagi, M. C. Bordage, G. J. M. Hagelaar, W. L. Morgan, A. V. Phelps, and L. C. Pitchford, "The LXCat project: Electron scattering cross sections and swarm parameters for low temperature plasma modeling," *Chemical Physics*, vol. 398, pp. 148–153, 2012, https://doi.org/10.1016/j.chemphys.2011.04.020

[40] L. C. Pitchford, L. L. Alves, K. Bartschat, S. F. Biagi, M.-C. Bordage, I. Bray, C. E. Brion, M. J. Brunger, L. Campbell, A. Chachereau, B. Chaudhury, L. G. Christophorou, E. Carbone, N. A. Dyatko, C. M. Franck, D. V. Fursa, R. K. Gangwar, V. Guerra, P. Haefliger, G. J. M. Hagelaar, A. Hoesl, Y. Itikawa, I. V. Kochetov, R. P. McEachran, W. L. Morgan, A. P. Napartovich, V. Puech, M. Rabie, L. Sharma, R. Srivastava, A. D. Stauffer, J. Tennyson, J. de Urquijo, J. van Dijk, L. A. Viehland, M. C. Zammit, O. Zatsarinny, and S. Pancheshnyi, "LXCat: an Open-Access, Web-Based Platform for Data Needed for Modeling Low Temperature Plasmas," *Plasma Processes and Polymers*, vol. 14, no. 1-2, p. 1600098, 2017, https://doi.org/10.1002/ppap.201600098

[41] E. Carbone, W. Graef, G. Hagelaar, D. Boer, M. M. Hopkins, J. C. Stephens, B. T. Yee, S. Pancheshnyi, J. van Dijk, and L. Pitchford, "Data Needs for Modeling Low-Temperature Non-Equilibrium Plasmas: The LXCat Project, History, Perspectives and a Tutorial," *Atoms*, vol. 9, no. 1, p. 16, 2021, https://doi.org/10.3390/atoms9010016

[42] T. Fujimoto, *Plasma Spectroscopy*. Oxford, United Kingdom: New York, 2004, ISBN: 978-0-19-853028-2, https://doi.org/10.1093/acprof:oso/9780198530282.001.0001

[43] H. Akatsuka, "Optical Emission Spectroscopic Analysis Based on Collisional-Radiative Model for Diagnostics of Low-Temperature Processing Plasmas," *Journal of Plasma and Fusion Research*, vol. 99, no. 8, pp. 377–384, 2023, [in Japanese], https://

www.jspf.or.jp/Journal/PDF_JSPF/jspf2023_08/jspf2023_08-377.pdf [Online archive]: https://warp.da.ndl.go.jp/info:ndljp/pid/13581736/www.jspf.or.jp/Journal/PDF_JSPF/jspf2023_08/jspf2023_08-377.pdf

[44] T. Fujimoto, "Plasma Spectroscopy — Ionizing-, Recombining- and Equilibrium-Plasmas," *Journal of the Spectroscopical Society of Japan*, vol. 34, no. 6, pp. 347–358, 1985, [in Japanese], https://www.doi.org/10.5111/bunkou.34.347

[45] T. Fujimoto, "Kinetics of Ionization-Recombination of a Plasma and Population Density of Excited Ions. I. Equilibrium Plasma," *Journal of the Physical Society of Japan*, vol. 47, no. 1, pp. 265–272, 1979, https://doi.org/10.1143/JPSJ.47.265

[46] T. Fujimoto, "Kinetics of Ionization-Recombination of a Plasma and Population Density of Excited Ions. II. Ionizing Plasma," *Journal of the Physical Society of Japan*, vol. 47, no. 1, pp. 273–281, 1979, https://doi.org/10.1143/JPSJ.47.273

[47] T. Fujimoto, "Kinetics of Ionization-Recombination of a Plasma and Population Density of Excited Ions. III. Recombining Plasma–High-Temperature Case," *Journal of the Physical Society of Japan*, vol. 49, no. 4, pp. 1561–1568, 1980, https://doi.org/10.1143/JPSJ.49.1561

[48] T. Fujimoto, "Kinetics of Ionization-Recombination of a Plasma and Population Density of Excited Ions. IV. Recombining Plasma–Low-Temperature Case," *Journal of the Physical Society of Japan*, vol. 49, no. 4, pp. 1569–1576, 1980, https://doi.org/10.1143/JPSJ.49.1569

[49] T. Fujimoto, "Kinetics of Ionization-Recombination of a Plasma and Population Density of Excited Ions. V. Ionization-Recombination and Equilibrium Plasma," *Journal of the Physical Society of Japan*, vol. 54, no. 8, pp. 2905–2914, 1985, https://doi.org/10.1143/JPSJ.54.2905

[50] J. Vlček, "A collisional-radiative model applicable to argon discharges over a wide range of conditions. I. Formulation and basic data," *Journal of Physics D: Applied Physics*, vol. 22, no. 5, pp. 623–631, 1989, https://doi.org/10.1088/0022-3727/22/5/009

[51] Y. Yamashita, T. Akiba, T. Iwanaga, H. Yamaoka, S. Date, and H. Akatsuka, "Developing an optimization algorithm for diagnostic modeling of optical emission spectroscopic measurement of non-equilibrium plasmas based on the argon collisional-radiative model," *Japanese Journal of Applied Physics*, vol. 60, no. 4, p. 046003, 2021, https://doi.org/10.35848/1347-4065/abe642

[52] Y. Yamashita, T. Akiba, T. Iwanaga, H. Yamaoka, S. Date, and H. Akatsuka, "Optical Emission Spectroscopic Measurement of Argon Low-Pressure Inductively Coupled Plasma Based on the Optimization Algorithm of Plasma Diagnostic Model," *IEEE Transactions on Plasma Science*, vol. 50, no. 6, pp. 1875–1889, 2022, https://doi.org/10.1109/TPS.2022.3172944

[53] M. Abdel-Rahman, T. Gans, V. Schulz-von der Gathen, and H. F. Döbele, "Space and time resolved rotational state populations and gas temperatures in an inductively coupled hydrogen RF discharge," *Plasma Sources Science and Technology*, vol. 14, no. 1, pp. 51–60, 2005, https://doi.org/10.1088/0963-0252/14/1/007

[54] P. Buchner, H. Schubert, J. Uhlenbusch, M. Weiβ, and K. Willée, "Diagnostics and modelling of a thermal RF plasma process used for the flash evaporation of zirconia powders," *Heat and Mass Transfer under Plasma Conditions*, vol. 891, pp. 296–303, 1999, https://doi.org/10.1111/j.1749-6632.1999.tb08776.x

[55] R. Caetano, Y. D. Hoyer, I. M. Barbosa, K. G. Grigorov, and B. N. Sismanoglu, "RADIAL MEASUREMENTS OF GAS DISCHARGE PARAMETERS OF ATMOSPHERIC PRESSURE MICROPLASMA," *International Journal of Modern Physics B*, vol. 27, no. 18, p. 1350089, 2013, https://doi.org/10.1142/s0217979213500896

[56] S. Ries, N. Bibinov, M. Rudolph, J. Schulze, S. Mráz, J. M. Schneider, and P. Awakowicz, "Spatially resolved characterization of a dc magnetron plasma using optical emission spectroscopy," *Plasma Sources Science and Technology*, vol. 27, no. 9, p. 094001, 2018, https://doi.org/10.1088/1361-6595/aad6d9

[57] S. Shi, K. Finch, and G. Gamez, "Radially resolved optical emission spectral imaging study of an atmospheric pressure μDBD jet for elucidating the effect of sample surface material on the underlying mechanisms," *Journal of Analytical Atomic Spectrometry*, vol. 36, no. 5, pp. 1055–1073, 2021, https://doi.org/10.1039/D0JA00522C

[58] S. Shi, K. Finch, Y. She, and G. Gamez, "Development of Abel's inversion method to extract radially resolved optical emission maps from spectral data cubes collected via push-broom hyperspectral imaging with sub-pixel shifting sampling," *Journal of Analytical Atomic Spectrometry*, vol. 35, no. 1, pp. 117–125, 2020, https://doi.org/10.1039/C9JA00239A

[59] Q. Xiong, L. Xu, L. Xiong, Q. Huang, Q. Chen, Y. Chen, X. Wang, and X. Jiang, "Heat deposition in the thermal field of a micro-glow discharge: effect of humidity," *Plasma Sources Science and Technology*, vol. 27, no. 9, p. 095010, 2018, https://doi.org/10.1088/1361-6595/aacf30

[60] Y.-K. Pu, Z.-D. Yu, and Z.-G. Guo, "Effect of wall reflection on the determination of electron temperature by the line-ratio method in inductively coupled plasmas," *Physics of Plasmas*, vol. 12, no. 11, p. 113301, 2005, https://doi.org/10.1063/1.2124527

[61] M. Odstrčil, J. Mlynář, V. Weinzettl, P. Háček, T. Odstrčil, G. Verdoolaege, M. Berta, T. Szabolics, and A. Bencze, "Plasma tomographic reconstruction from tangentially viewing camera with background subtraction," *Review of Scientific Instruments*, vol. 85, p. 013509, 2014, https://doi.org/10.1063/1.4862652

[62] K. Munechika, H. Tsutsui, and S. Tsuji-Iio, "Visible Light Tomography Considering Reflection Light in a Small Tokamak Device PHiX," *Plasma and Fusion Research*, vol. 16, p. 2402033, 2021, https://doi.org/10.1585/pfr.16.2402033

[63] G. Ghosh, "Dispersion-equation coefficients for the refractive index and birefringence of calcite and quartz crystals," *Optics Communications*, vol. 163, no. 1, pp. 95–102, 1999, https://doi.org/10.1016/S0030-4018(99)00091-7

[64] KLA Corporation, *Hakumaku atsu sokutei no tame no Quartz kussetsu ritu* （薄膜厚測定のための *Quartz* 屈折率）, based on [63], [in Japanese]. https://www.filmetricsinc.jp/refractive-index-database/Quartz

[65] H. Yatagai, *Optics*（光学）. Tokyo, Japan: Asakura Shoten, 2017, [in Japanese], ISBN: 978-4-254-13121-5, http://id.ndl.go.jp/bib/025696846

[66] A. Kramida, Y. Ralchenko, J. Reader, and NIST ASD Team, *NIST Atomic Spectra Database*, 2022, https://physics.nist.gov/asd

[67] Y. Yamashita, K. Doi, T. Kiyota, S. Hosoya, A. Nezu, and H. Akatsuka, "Diagnosis of argon inductively coupled plasma by optical emission spectroscopic measurement with compensation of spectral reflectance on chamber inner wall," in *43rd International Symposium on Dry Process (DPS 2022)*, Osaka, Japan; Online, 2022, conference proceedings, pp. 47–48, ISBN: 978-4-900986-23-7, https://www.dry-process.org/2022/

[68] T. Iwanaga, H. Nakamura, M. Ebisawa, and T. Yamamoto, "Development of calibration system for spectral radiance measurement," *Bulletin of Tokyo Metropolitan Industrial Technology Research Institute*, no. 5, pp. 34–37, 2010, https://www.iri-tokyo.jp/uploaded/attachment/879.pdf [Online archive]: https://dl.ndl.go.jp/pid/9212384

[69] J. B. Boffard, R. O. Jung, C. C. Lin, L. E. Aneskavich, and A. E. Wendt, "Optical diagnostics for characterization of electron energy distributions: argon inductively coupled plasmas," *Plasma Sources Science and Technology*, vol. 20, no. 5, p. 055006, 2011, https://doi.org/10.1088/0963-0252/20/5/055006

[70] J. Hopwood, C. R. Guarnieri, S. J. Whitehair, and J. J. Cuomo, "Electromagnetic fields in a radio ‐ frequency induction plasma," *Journal of Vacuum Science & Technology A*, vol. 11, no. 1, pp. 147–151, 1993, https://doi.org/10.1116/1.578281

[71] A. V. Vasenkov and M. J. Kushner, "Angular anisotropy of electron energy distributions in inductively coupled plasmas," *Journal of Applied Physics*, vol. 94, no. 9, pp. 5522–5529, 2003, https://doi.org/10.1063/1.1614428

[72] R. Decoste, "X ‐ ray tomography on plasmas with arbitrary cross sections and limited access," *Review of Scientific Instruments*, vol. 56, no. 5, pp. 806–808, 1985, https://doi.org/10.1063/1.1138179

[73] R. S. Granetz and P. Smeulders, "X-ray tomography on JET," *Nuclear Fusion*, vol. 28, no. 3, pp. 457–476, 1988, https://doi.org/10.1088/0029-5515/28/3/011

[74] T. Hermann, S. Löhle, S. Fasoulas, and A. Andrianatos, "Tomographic optical emission spectroscopy of a high enthalpy air plasma flow," *Applied Optics*, vol. 55, no. 36, pp. 10 290–10 298, 2016, https://doi.org/10.1364/AO.55.010290

[75] R. Barni, P. Alex, E. Ghorbanpour, and C. Riccardi, "A spectroscopical study of H_2 emission in a simply magnetized toroidal plasma," *The European Physical Journal D*, vol. 75, no. 3, p. 101, 2021, https://doi.org/10.1140/epjd/s10053-021-00109-4

[76] Y. Miyoshi, Z. L. Petrovic, and T. Makabe, "Optical computerized tomography of the E-H transition in inductively coupled plasmas in Ar and Ar-CF4 mixtures," *Journal of Physics D: Applied Physics*, vol. 35, p. 454, 2002, https://doi.org/10.1088/0022-3727/35/5/307

[77] Y. Miyoshi, Z. L. Petrovic, and T. Makabe, "Transition between capacitive and inductive mode in inductively coupled plasma observed by emission computerized tomography," *IEEE Transactions on Plasma Science*, vol. 30, no. 1, pp. 130–131, 2002, https://doi.org/10.1109/TPS.2002.1003958

[78] X. Wan, S. L. Yu, G. Y. Cai, Y. Q. Gao, and J. L. Yi, "Three-dimensional plasma field reconstruction with multiobjective optimization emission spectral tomography," *Journal of the Optical Society of America a-Optics Image Science and Vision*, vol. 21, no. 7, pp. 1161–1171, 2004, https://doi.org/10.1364/josaa.21.001161

[79] K. Rathore, S. Bhattacharjee, D. N. Patel, and P. Munshi, "Optical Emission Spectroscopy-Based Tomography for Compact Low-Pressure Microwave Plasma in a Multicusp," *IEEE Transactions on Plasma Science*, vol. 45, no. 9, pp. 2492–2503, 2017, https://doi.org/10.1109/tps.2017.2734963

[80] V. Gonzalez-Fernandez, P. David, R. Baude, A. Escarguel, and Y. Camenen, "Spatially resolved determination of the electronic density and temperature by a visible spectro-tomography diagnostic in a linear magnetized plasma," *Scientific Reports*, vol. 10, no. 1, p. 5389, 2020, https://doi.org/10.1038/s41598-020-62426-9

[81] D. Lee, J. Kim, G. Doh, C. Shin, and W. Choe, "Two-dimensional electron temperature and density profiles of Hall thruster plume plasmas using tomographically reconstructed optical emission spectroscopy," *Plasma Sources Science and Technology*, vol. 31, no. 12, p. 125004, 2022, https://doi.org/10.1088/1361-6595/aca714

[82] S. Park, W. Choe, S. Y. Moon, and S. J. Yoo, "Electron characterization in weakly ionized collisional plasmas: from principles to techniques," *Advances in Physics: X*, vol. 4, no. 1, p. 1526114, 2019, https://doi.org/10.1080/23746149.2018.1526114

[83] J. Jang, S. Park, J. Y. Park, and W. Choe, "Tomography-based spatial uniformity diagnostics for meter-sized plasmas," *Plasma Sources Science and Technology*, vol. 27, no. 10, p. 10LT01, 2018, https://doi.org/10.1088/1361-6595/aac671

[84] M. Anton, H. Weisen, M. J. Dutch, W. v. d. Linden, F. Buhlmann, R. Chavan, B. Marletaz, P. Marmillod, and P. Paris, "X-ray tomography on the TCV tokamak," *Plasma Physics and Controlled Fusion*, vol. 38, no. 11, p. 1849, 1996, https://doi.org/10.1088/0741-3335/38/11/001

[85] D. R. Ferreira, *isttok-tomography*, 2019, https://github.com/diogoff/isttok-tomography

[86] P. J. Carvalho, "Tomography Algorithms for Real-Time Control in ISTTOK," Ph.D. thesis, Instituto Superior Técnico, Technical University of Lisbon, 2010.

[87] S.-X. Zhao, X. Xu, X.-C. Li, and Y.-N. Wang, "Fluid simulation of the E-H mode transition in inductively coupled plasma," *Journal of Applied Physics*, vol. 105, no. 8, p. 083306, 2009, https://doi.org/10.1063/1.3112009

[88] A. J. H. Donné, "Introduction to Plasma Diagnostics," *Fusion Science and Technology*, vol. 53, no. 2T, pp. 379–386, 2008, https://doi.org/10.13182/FST08-A1723

[89] B. Gonçalves, "Plasma Diagnostics," *Sensors*, vol. 24, no. 10, 2024, https://doi.org/10.3390/s24103257

[90] "International vocabulary of metrology — Basic and general concepts and associated terms (VIM)," ISO/IEC Guide 99:2007, 2007, http://id.ndl.go.jp/bib/000011024781 [Available online]: https://www.iso.org/iso_iec_Guides

[91] E. Gudimenko, V. Milosavljević, and S. Daniels, "Influence of self-absorption on plasma diagnostics by emission spectral lines," *Optics Express*, vol. 20, no. 12, pp. 12 699–12 709, 2012, https://doi.org/10.1364/OE.20.012699

[92] K. Lin, A. Nezu, and H. Akatsuka, "Development of diagnostics of electron density and temperature for atmospheric-pressure helium plasma based on optical emission spectroscopy analysis and a collisional-radiative model," *Japanese Journal of Applied Physics*, vol. 62, no. SL, p. SL1005, 2023, https://doi.org/10.35848/1347-4065/accc93

[93] E. Rozet, S. Rudaz, R. D. Marini, E. Ziémons, B. Boulanger, and P. Hubert, "Models to estimate overall analytical measurements uncertainty: Assumptions, comparisons and applications," *Analytica Chimica Acta*, vol. 702, no. 2, pp. 160–171, 2011, https://doi.org/10.1016/j.aca.2011.06.055

[94] X. Yu, G. D. Zanna, D. C. Stenning, J. Cisewski-Kehe, V. L. Kashyap, N. Stein, D. A. van Dyk, H. P. Warren, and M. A. Weber, "Incorporating Uncertainties in Atomic Data into the Analysis of Solar and Stellar Observations: A Case Study in Fe xiii," *The Astrophysical Journal*, vol. 866, no. 2, p. 146, 2018, https://doi.org/10.3847/1538-4357/aadfdd

[95] Z. L. Petrović, S. Dujko, D. Marić, G. Malović, c. Nikitović, O. Šašić, J. Jovanović, V. Stojanović, and M. Radmilović-Rađenović, "Measurement and interpretation of swarm parameters and their application in plasma modelling," *Journal of Physics D: Applied Physics*, vol. 42, no. 19, p. 194002, 2009, https://doi.org/10.1088/0022-3727/42/19/194002

[96] P. F. Knapp, W. E. Lewis, V. R. Joseph, C. A. Jennings, and M. E. Glinsky, "Optimizing the configuration of plasma radiation detectors in the presence of uncertain instrument response and inadequate physics," *Journal of Plasma Physics*, vol. 89, no. 1, p. 895890101, 2023, https://doi.org/10.1017/S002237782200126X

[97] M. He, R. Bai, S. Tan, D. Liu, and Y. Zhang, "Data-driven plasma science: A new perspective on modeling, diagnostics, and applications through machine learning," *Plasma Processes and Polymers*, vol. 21, no. 9, p. 2400020, 2024, https://doi.org/10.1002/ppap.202400020

[98] S. Park, J. Seong, Y. Jang, H.-J. Roh, J.-W. Kwon, J. Lee, S. Ryu, J. Song, K.-B. Roh, Y. Noh, Y. Park, Y. Jang, T. Cho, J.-H. Yang, and G.-H. Kim, "Plasma information-based virtual metrology (PI-VM) and mass production process

control," *Journal of the Korean Physical Society*, vol. 80, no. 8, pp. 647–669, 2022, https://doi.org/10.1007/s40042-022-00452-8

[99] T. van der Gaag, A. Nezu, and H. Akatsuka, "Practical considerations of the visible bremsstrahlung inversion (VBI) method for arbitrary EEDF determination in cold atmospheric-pressure plasma," *Japanese Journal of Applied Physics*, vol. 61, no. 7, p. 076004, 2022, https://doi.org/10.35848/1347-4065/ac7835

[100] S. J. Hong, G. S. May, and D.-C. Park, "Neural network modeling of reactive ion etching using optical emission spectroscopy data," *IEEE Transactions on Semiconductor Manufacturing*, vol. 16, no. 4, pp. 598–608, 2003, https://doi.org/10.1109/TSM.2003.818976

[101] Y. Mizui, T. Kojima, S. Miyagi, and O. Sakai, "Graphical Classification in Multi-Centrality-Index Diagrams for Complex Chemical Networks," *Symmetry*, vol. 9, no. 12, p. 309, 2017, https://doi.org/10.3390/sym9120309

[102] T. Murakami and O. Sakai, "Rescaling the complex network of low-temperature plasma chemistry through graph-theoretical analysis," *Plasma Sources Science and Technology*, vol. 29, no. 11, p. 115018, 2020, https://doi.org/10.1088/1361-6595/abbdca

[103] F. Krüger, T. Gergs, and J. Trieschmann, "Machine learning plasma-surface interface for coupling sputtering and gas-phase transport simulations," *Plasma Sources Science and Technology*, vol. 28, no. 3, p. 035002, 2019, https://doi.org/10.1088/1361-6595/ab0246

[104] B. Kim and G. S. May, "An optimal neural network process model for plasma etching," *IEEE Transactions on Semiconductor Manufacturing*, vol. 7, no. 1, pp. 12–21, 1994, https://doi.org/10.1109/66.286829

Index